OMIP

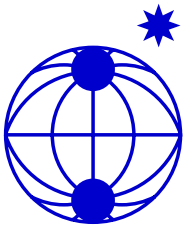

Vergleich der thermohalinen Zirkulation in zwei globalen ozeanischen Zirkulationsmodellen

The Ocean Model Intercomparison Project

by the German OMIP Group:

Bernadette Fritzsch (AWI)
Ruediger Gerdes (AWI)
Wolfgang Hiller (AWI)
Mojib Latif (MPI)
Stephanie Legutke (MPI)
Ernst Maier-Reimer (MPI)
Dirk Olbers (AWI)
Frank Roeske (MPI)

Alfred Wegener Institute for Polar and Marine Research, Bremerhaven
Max-Planck-Institute for Meteorology, Hamburg

Abschlußbericht BMBF Projekt 01 LA 9862/8
Oktober 2000

Contents

Chapter 1

Das deutsche OMIP Projekt

In diesem Projekt werden die zwei für die deutsche Klimaforschung wichtigsten numerischen ozeanischen Zirkulationsmodelle MOM und HOPE in ihren Fähigkeiten verglichen, den mittleren Zustand der globalen Zirkulation darzustellen. Dazu wurden Langzeitintegrationen in globaler Konfiguration unter möglichst identischen Randbedingungen konzipiert. Die Auswertung soll zu einer Bewertung der Modelle bezüglich der Darstellung der globalen Zirkulation und des Einsatzes für Klimauntersuchungen führen.

Der Zustand der mittleren großräumigen Zirkulation ist quantitativ nicht bekannt. Messungen liegen zwar vor, weisen aber starke zeitliche Variationen auf und sind mit Ausnahme der hydrographischen Felder und einige natürlicher Tracer nicht repräsentativ für die mittlere Zirkulation. Modelle können deshalb nur indirekt über den Effekt der großräumigen Zirkulation auf die Tracerverteilungen verifiziert werden.

Neben der Verifikation anhand von Hydrographie und Tracerfeldern kommt daher dem Vergleich von verschiedenen Modellen besondere Bedeutung zu. Mit der Bandbreite der allein durch Numerik und unvermeidliche Unterschiede in der Konfiguration bedingten Abweichungen erhält man eine untere Grenze für den Fehler der verwendeten Zirkulationsmodelle. Ein systematischer Vergleich der Modellergebnisse untereinander und mit beobachteten Tracerverteilungen ist eine Grundlage für eine Verbesserung der Ozeanmodelle. Das Merkmal des vorliegenden Vergleichs liegt in dem Anspruch, die Modelle in möglichst identischer Konfiguration bezüglich der Parametrisierungen, der Topographie und der Antriebe zu gestalten.

Das Projekt ist Teil der internationalen Studie OMIP (Ocean Model Intercomparison Project). Anfängliche Pläne, weitere deutsche Modelle (LSG, OPYC) und auch die dekadische Variabilität in diesen Modelle im Vergleich mit zu berücksichtigen, konnten nicht eingehalten werden, da Zusagen für eine zusätzliche personelle Unterstützung der Betreuer dieser Modelle zurückgezogen wurden. Weitere deutsche Beiträge zu OMIP sind in dem von der EU geförderten Projekt 'DYNAMO' durchgeführt worden (Dynamo Group 1997, Willebrand et al. 2000).

1.1 Ziele des Projekts

Die spezifischen wissenschaftlichen und technischen Ziele dieses Projektes sind:

- eine parallele Version des MOM2 Code zu erzeugen und verfügbar zu machen, die ein Meereismodul enthält.
- globale atmosphärische Antriebsfelder für globale Ozeanmodelle zu erzeugen und verfügbar zu machen, die von verschiedenen Modellen verwendet werden können. Hierzu soll ein typisches Jahr von täglichen Antriebsparametern aus der am Euroäischen Zentrum für Mittelfristvorhersagen (EZMWF) durchgeführten Reanalyse ERA erstellt werden.
- einen detaillierten Vergleich des mittleren Jahresgangs in den Modellen MOM2 und HOPE zu erarbeiten.

- Grundlagen für generelle Empfehlungen zum Betreiben von globalen Ozeanmodellen zu legen.

1.2 Physikalische Aspekte von Ozeanmodellen

Der Ozean ist für die Klimavariabilität im Zeitskalenbereich von Monaten bis zu einigen Jahrtausenden die bedeutsamste Komponente des Klimasystems. Die schnelleren Zeitskalen sind im Verhalten der äquatorialen Zirkulation, in der globalen Deckschicht (einschließlich des Konvektionsvorgangs) und den Rossbywellen und mesoskaligen Wirbeln verankert, die langsamen Zeitskalen sind durch die advektiven und diffusiven Umwälzungs- und Vermischungsprozesse bedingt. Eine Implementierung aller wesentlichen klimarelevanten Prozesse, die in diesem breiten Spektrum angesiedelt sind - in einem universellen Zirkulationsmodell des Weltozeans - übersteigt die gegenwärtigen Computerresourcen um viele Größenordnungen an Rechenzeit und Speichergröße. Abgesehen von neueren Versuchen, mesoskalige Wirbelprozesse global darzustellen (Semtner und Chervin, 1992) - wegen der enormen Rechenzeiten muss man sich hierbei auf kleine Störungen eines vorgegebenen thermohalinen Zustands über nur wenige Dekaden beschränken - laufen gegenwärtig alle globalen Modelle mit horizontalen Auflösungen im Bereich $2° - 4°$ und mit 10 bis 20 vertikalen Schichten.

In diesen ozeanischen Modellen (Ocean General Circulation Models, OGCM), die in dieser groben Auflösung auch für gekoppelte Klimamodelle eingesetzt werden, sind alle turbulenten Prozesse, alle für eine korrekte Darstellung der Oberflächentemperatur (und damit Kopplung an die Atmosphäre) bedeutsamen thermohalinen Vorgänge in der Deckschicht und die bei instabiler Schichtung einsetzenden Prozesse der Tiefenkonvektion nur in sehr grob parametrisierter Form enthalten. In vielen Fällen wird außerdem auf die Simulation des Jahresgangs verzichtet, um Beschleunigungstechniken (Bryan, 1984) für das Erreichen eines stationären Zustands der Zirkulation auszunutzen. In diesem Fall ist der saisonale Zyklus nicht adäquat eingeschwungen. Darüberhinaus haben die simulierten Zirkulationssysteme und thermohalinen Zustandsgrößen einen stark diffusiven Charakter, der durch die Stabilitätsanforderungen der groben räumlichen Auflösung hervorgerufen wird. Trotz der zu erwartenden Rechnerentwicklung (massiv parallele Systeme etc.) und Verbesserungen von Modellcodes (Parallelisierung etc) ist abzusehen, daß Studien mit ozeanischen Zirkulationsmodellen, die die volle Einstellung des thermohalinen Zustands beinhalten, auch in den nächsten Jahren unter diesen Schwachpunkten leiden werden. Dies ist auch bedeutsam in der weitergehenden Klimamodellierung, da die Güte von Simulationen zu erwartender Klimaentwicklungen unter den Mängeln der ozeanischen Modellkomponente leidet. Eingehende Untersuchungen zum Vergleich der wenigen heute existierenden Modelltypen sind daher dringend geboten.

Die Parametrisierungen in ozeanischen Modellen sind mit Unsicherheiten behaftet, die auf unzureichender Kenntnis der Prozesse und ihres Zusammenhangs mit den aufgelösten Variablen beruhen. Numerische Aspekte spielen ebenfalls eine große Rolle, da Strukturen und Vorgänge am Rande der Gitterauflösung die Lösung mit prägen. Aus dieser Situation erklärt sich das zum Teil sehr unterschiedliche Verhalten von oberflächlich ähnlichen Modellen, denen dieselben physikalischen Gleichungen zugrunde liegen. Dies betrifft insbesondere den mittleren Zustand des Ozeans aber auch die Variabilität und Sensitivität der thermohalinen Zirkulation. An der grundsätzlichen Situation wird sich in den nächsten Jahren nichts ändern, da die absehbare Rechnerentwicklung nicht dem Ressourcenbedarf von Modellen mit ausreichend hoher Auflösung genügt. Dies gilt insbesondere für den Ozean, weil extrem hohe Auflösung (wenige Kilometer) in hohen Breiten für die explizite Beschreibung der für die thermohaline Zirkulation entscheidenden Vorgänge (u.a. Wassermassenbildung, Abfluß von Schelfmeeren, Überströmung von topographischen Hindernissen, Vermischung in Randströmen) notwendig wäre.

Alle gegenwärtig vorliegenden Ozeanmodelle haben erhebliche Probleme in der Darstellung der ozeanischen Zirkulation. Insbesondere ist der thermohaline Zustand (Temperatur und Salzgehalt) fehlerhaft, während Zeitskalen für Ventilation (aus der Simulation von H3, 14C etc.) gut mit Kenntnissen aus geochemischen Untersuchungen übereinstimmen. Es ist vielfach nicht klar, ob Fehler

der Modelle (z.B. Produktion von Wassermassen an der richtigen Stelle mit der richtigen Rate) relevant für Klimastudien sind. Für die jeweilig abgedeckten Zeitskalen sind die Ozeanmodelle in ihrer Güte aber vergleichbar mit entsprechend grob aufgelösten atmosphärischen Zirkulationsmodellen, so daß ihr Einsatz in gekoppelten Experimenten sinnvoll ist.

Die globale Verteilung der Antriebe (Wärme-, Frischwasser und Impulsflüsse an der Oberfläche) sind nur sehr ungenau bekannt. Es ist offensichtlich (aus Sensitivitätsstudien), daß viele Probleme der groben Modelle von Fehlern in den Oberflächenflüssen herrühren. Wenn Modelle auf falsche Flüsse eingestellt sind, reagieren sie in gekoppelten Experimenten auch falsch. Schon Fehler von der Größe $1 W/m^2$ führen bei Langzeitintegration zu erheblichen Unterschieden. Hieraus resultieren prinzipielle Schwierigkeiten bei der Kopplung von Ozean- und Atmosphärenmodellen, da die gegenseitig übertragenen Flüsse von Wärme und Frischwasser in der Regel nicht zu korrekten Gleichgewichtszuständen führen. Flusskorrekturmethoden sind notwendig, aber nach physikalischen Gesichtpunkten nicht zu akzeptieren. Ozeanmodelle werden im Alleinbetrieb allerdings in der Regel nicht durch Vorgabe der Flüsse, sondern in mehr oder weniger komplexer Weise durch Relaxation an atmosphärische (oder ozeanische) Oberflächentemperaturen und den ozeanischen Oberflächensalzgehalt angetrieben. Gegenwärtig sind auch einfache atmosphärische Modelle in der Entwicklung, die die Oberflächentemperatur oder Wärmefluss und den Frischwasserfluss liefern sollen.

Die Entwicklung von Parametrisierungen für grob auflösende Ozeanmodelle, wie sie in gekoppelten Klimamodellen verwendet werden, hat in den letzten Jahren erhebliche Fortschritte gemacht. Die Parametrisierungen sind aber bisher nur unvollständig auf ihren tatsächlichen Nutzen für die Klimavorhersage geprüft worden Auch verschiedene numerische Realisierungen der physikalischen Grundgleichungen sind bisher nicht systematisch für diesen Zweck verglichen worden. Für die langfristige Vorhersage von Klimaveränderungen ergibt sich daraus der dringende Bedarf einer Bestandsaufnahme verfügbarer Parametrisierungen und vorhandener, in gekoppelten globalen Modellen eingesetzter Ozeanmodelle.

Wirbelbedingte Transporte von Wärme, Salz und Impuls werden in groben Ozeanmodellen im Gegensatz zu atmosphärischen Modellen heute noch außerordentlich primitiv parametrisiert. Dies gilt in noch größerem Maße für nichthydrostatische Vorgänge wie beispielsweise Konvektion, Doppeldiffusion und durch interne Wellen bedingte Vermischung. Wegen der hydrostatischen Approximation sind diese Prozesse nicht in den primitiven Gleichungen enthalten und müssen in jedem Fall, unabhängig von der Auflösung, parametrisiert werden. Falsche Parametrisierung der Eddytransporte ergibt nicht nur Fehler in den mittleren Zuständen, sondern auch in der Variabilität, was besonders auf kurzen Zeitskalen (ENSO) Bedeutung hat. Alle oben genannten Modelle haben in grober Auflösung große implizite (d.h. durch Numerik bedingte) Diffusion von Wärme, Salz und Impuls. Unterschiedliche Advektionschemata ergeben daher in sonst identischen Modellen gravierende Unterschiede (Gerdes et al., 1991).

Der Einsatz des flux-corrected-transport (FCT-) Verfahrens konnte im MOM-Modell eine merkliche Reduktion der aus numerischen Gründen vorhandenen Diffusion erreichen. Dies ist eine Voraussetzung für den sinnvollen Einsatz von physikalisch motivierten Diffusionsparametrisierungen. Bei der sonst üblichen hohen Diffusion in den Koordinatenrichtungen des Modells ist eine physikalisch sinnvolle Orientierung des Vermischungstensors in isopykner und diapykner Richtung wenig erfolgversprechend. Die physikalische diapykne Diffusion tritt weit hinter die numerisch bedingte diapykne Komponente der horizontalen Diffusion an stark geneigten Isopyknen zurück. Der Effekt der Wirbel auf die großkaligen Verteilungen beschränkt sich nicht auf eine reine Vermischung von Tracern. Die Freisetzung von verfügbarer potentieller Energie bei barokliner Instabilität hat potentiell einen erheblichen Einfluß auf die mittlere Zirkulation. Hierfür ist vor kurzem eine Parametrisierung vorgeschlagen worden (Gent und McWilliams, 1992), die in ersten Versuchen verbesserte Ergebnisse geliefert hat. Weiterhin ist der rektifizierte Effekt von wirbelbedingten 'eddy form drag' an topographischen Strukturen zu berücksichtigen, der eine Tendenz zu einer zyklonalen Zirkulation an den Beckenrändern hervorruft (Holloway, 1992, Eby und Holloway, 1994).

Grobauflösende Modelle haben grundlegende Schwierigkeiten, die Überströmung von topographischen Hindernissen korrekt wiederzugeben. Sie liegen in dem durch die horizon-

tale Auflösung bedingten Unvermögen, ausreichend relative Vorticity zu erzeugen, um bei der Stauchung einer rotierenden Flüssigkeitssäule die potentielle Vorticity zu erhalten (Gerdes, 1993a,b). Bei Überströmung von untermeerischen Schwellen kommt es daher zu erhöhter diapykner Vermischung. Bei bodennaher Ausbreitung von dichten Wassermassen über einem Hang trägt die Abfolge von horizontaler Advektion und konvektiver Vermischung zu der erhöhten Vermischung in z-Koordinatenmodellen bei (Gerdes, 1993; Roberts et al., 1996). Da viele Tiefenwasserbildungsgebiete vom globalen Ozean durch Schwellen getrennt sind oder auf flachen Schelfen liegen, ist diese Problematik von großer Bedeutung für die Simulation der thermohalinen Zirkulation. Hochauflösende Modelle haben aber gezeigt, daß auch rein geometrische Effekte (Öffnung und Tiefe von Kanälen durch die topographische Schwelle) einen erheblichen Einfluß auf die Überströmung und das großräumige Zirkulationsmuster haben können. Verbesserungen in grob auflösenden Modellen sind von neuen Parametrisierungen der Vorgänge in bodennahen Grenzschichten zu erwarten (Beckmann und Döscher, 1997).

Das Klimasystem kann bei gleicher solarer Einstrahlung anscheinend verschiedene Gleichgewichtszustände annehmen (Manabe und Stouffer, 1994), abhängig von Anfangsbedingungen. Auch in Ozeanmodellen allein findet man mehrere Gleichgewichte (Marotzke und Willebrand, 1991). Unter gemischten Randbedingungen (fest vorgegebene Lufttemperatur und Frischwasserflüsse) erscheint der heutige Zustand mit seiner ausgeprägten Atlantischen thermohalinen Zirkulation sehr sensitiv gegen relativ kleine Störungen im Salzgehalt oder im Frischwasserfluss an der Oberfläche (Bryan, 1986). Gemischte Randbedingungen, obwohl physikalisch besser motiviert als die sonst übliche Dämpfung an klimatologische Oberflächenverteilungen, repräsentieren die Wechselwirkung mit einer höchst artifiziellen Atmosphäre. Durch die Vernachlässigung wichtiger Rückkopplungsmechanismen, mit Ausnahme des positiven Salztransportfeedbacks, wird die Sensitivität des System extrem gesteigert. Neuere Arbeiten haben gezeigt, daß die Sensitivität der thermohalinen Zirkulation und damit die zu erwartende Variabilität sehr stark von den Wärmetransporten in der Atmosphäre (Rahmstorf und Willebrand, 1994) abhängen. Auch die Annahme konstanter Frischwasserflüsse an der Ozeanoberfläche, die bei gemischten Randbedingungen gemacht wird, ist bei massiven Änderungen der thermohalinen Zirkulation nicht gerechtfertigt. Die atmosphärischen Feuchtetransporte können einen starken destabilisierenden Einfluss auf die thermohaline Zirkulation haben (Lohmann et al., 1996, Nakamura et al. 1994). Der Effekt variabler Meereisbedeckung und -transporte ist bisher nicht systematisch untersucht worden.

1.3 Numerische Aspekte

Es liegen nur wenige verschiedene Codes vor, die für globale Ozeanmodelle nutzbar sind. In Deutschland werden außer dem klassischen Modell (MOM) von Bryan (1969) und Cox (1984) in verschiedenen Weiterentwicklungsstufen (MOM, MOM2, FSCC) die neueren Entwicklungen (LSG, HOPE, OPYC) aus dem MPI verwendet. Ein kurze Charakterisierung der Numerik von MOM2 und HOPE folgt.

- MOM

  Das MOM-Modell basiert auf den primitiven Gleichungen, d.h. dem vollständigen Satz der physikalischen Erhaltungsgleichungen für Masse, Impuls, Wärme und Salz sowie eine diagnostische Zustandsgleichung, die die lokale Dichte in Abhängigkeit von Druck, Temperatur und Salzgehalt beschreibt. Die in den MOM-Versionen durchgeführte rigid-lid-Approximation führt auf eine elliptische Gleichung für die Stromfunktion des Massentransportes, welche die numerische Komplexität des Modells stark dominiert. Zusätzlich sind jedoch Gleichungen vom parabolisch-hyperbolischen Typ für das interne Geschwindigkeitsfeld, die Temperatur und den Salzgehalt zu behandeln. Zeitschritte sind durch relativ schnelle interne Wellen diktiert, was auch zu einem erheblichen Aufwand führt.

- HOPE

  Das HOPE-Modell basiert wie das MOM- Modell auf den kompletten primitiven Gleichungen. Es besitzt eine freie Oberfläche. Um aber dennoch einen akzeptablen Zeitschritt zu

ermöglichen, ist der barotrope Teil implizit formuliert. Dadurch werden die schnellen externen Schwerewellenmoden stark gedämpft, dieses Verfahren ist allerdings gegenüber den langsamen planetaren Wellen neutral. Der barokline Anteil ist hingegen semi-implizit formuliert. Die Advektion basiert auf zentralen Differenzen, wodurch die numerische Diffusion verglichen mit dem LSG Modell, das ein upstream- Verfahren verwendet, deutlich reduziert werden konnte.

Die Güte der Simulation eines stationären Zustands sagt nicht notwendigerweise etwas über die Fähigkeit eines Modells aus, zeitlich veränderliche Vorgänge darzustellen. Numerische Techniken wie die Beschleunigung der langsam veränderlichen Modellgrößen in MOM (Bryan 1984) oder implizite Algorithmen in HOPE beeinflussen das zeitliche Antwortverhalten. Dies ist von besonderer Relevanz, da Ozeanmodelle unter Umständen mehrere stabile Gleichgewichtszustände haben und der schließlich erreichte Zustand nicht nur von den Anfangsbedingungen, sondern auch von der Integrationstechnik abhängen kann.

Für das Erreichen des stationären Zustands sind in den einzelnen Modellen sehr lange Integrationszeiten notwendig. Um die Läufe in angemessener Zeit durchführen zu können, müssen daher leistungsstarke Parallelrechner eingesetzt werden. Der Übergang auf Parallelrechner ist aber verbunden mit einer Umstrukturierung der vorhandenen Programme, die fast immer für Vektorrechner optimiert worden sind. Für MOM2 wurde im Rahmen des vorangegangenen BMBF–Projekts (Förderkennzeichen 07VKV01/1-39) zunächst für eine spezielle Optionskonfiguration eine parallelisierte Arbeitsversion erstellt. Diese soll nun verallgemeinert und in die Module des Programmpakets eingearbeitet werden. Dazu muss noch das Problem der effizienten Datenein- und -ausgabe gelöst werden. Weiterhin sind noch Untersuchungen zur physikalischen Validierung der parallelen Programmversion notwendig.

1.4 Zusammenfassung der Ergebnisse

OMIP ist ein internationales Unterfangen, verschiedene Modelle der großräumigen ozeanischen Zirkulation zu vergleichen und zu verbessern. Das vorliegende Projekt trägt dazu mit einem Vergleich zweier globaler Modelle bei – dem MOM2 aus der GFDL Modellfamilie und dem HOPE Modell des MPI Hamburg. Wir beschränken uns in dieser Arbeit auf den Vergleich des mittleren saisonalen Zyklus beider Modelle, der in beiden Modellen in gleicher Weise durch atmosphärische Antriebe erzeugt wurde, die aus der Reanalyse ERA des EZMWF gewonnen wurden. Dies, wie auch der Einbau eines Meereismoduls und die Parallelisierung eines der Ozean-Meereis Modelle, ist Bestandteil des Projektes. Der Report stellt die Ergebnisse folgender Arbeitspunkte vor:

- die Erstellung der atmosphärischen Antriebsfunktionen,
- die technischen Errungenschaften der Parallelisierung vom MOM2, einschließlich eines Meereismoduls,
- einige Kontrollexperimente mit MOM2 zur Advektion/Diffusion von Tracern,
- den mittleren Jahresgang beider Modelle.

Die Ergebnisse sind im Einzelnen in den Kapiteln 6.1 und 7.10 interpretiert und in Kapitel 7 in Vergleichsbildern dokumentiert. Eine kurze Zusammenfassung folgt:

- Technische Errungenschaften:

  Die Parallelisierung und Skalierbarkeit des MOM2 Ozeanmodells mit angekoppeltem Meereismodell wurde im Rahmen des Modellvergleichs wesentlich verbessert. Dies ist wichtig, da der im OMIP Projekt gewählte Parallelisierungsansatz einer zweidimensionalen Gebietsaufteilung in der zukünftig vom GFDL erscheinenden MOM3 Version nicht berücksichtigt wurde, sondern nach wie vor eine eindimensionale Gebietszerlegung enthält. Ein weiterer Vorteil des gewählten Parallelisierungsansatzes im OMIP Projekt besteht darin,

daß das grundlegende Konzept des Speicherfensters in MOM auch in der parallelen Variante erhalten bleibt. Dieses erlaubt dem MOM Nutzer die Parallelisierung im Kontext des Speicherfensters, was Möglichkeiten zur Berechnung von Modellen mit höherer Gitterpunktanzahl eröffnet und eine generelle Reduktion der Speicheranforderungen des Gesamtmodells zur Folge hat. Hierbei kommen auch die guten Skalierbarkeitseigenschaften des in OMIP parallelisierten MOM2/Meereismodells zum Tragen. Weiter wurden erste Untersuchungen angestellt, wie das parallele Modell mit einer atmosphärischen Komponente unter Einsatz externer Flußkoppler anzubinden wäre.

- Antriebe aus der ERA Analyse:

  Wir haben aus der 15-jährigen Reanalyse ERA des ECMWF einen mittleren Jahresgang von atmosphärischen Antrieben erzeugt, der typische tägliche Fluktuationen enthält. Süßwassereinträge über den Kontinenten wurden in einfacher Weise über ein Abflußmodell in Quellen entlang den Küsten transformiert. Wärme- und Süßwasserbudgets sind über den Jahresgang geschlossen und die Antriebe sind unabhängig von Ozeanmodellen erstellt.

- Ergebnisse der Sensitivitätsexperimente aus Kapitel 6.1:

  - Die großräumige Verteilung der Wassermassen wird von beiden Modelle befriedigend wiedergegeben. Die 2° Auflösung reicht offensichtlich aus, um die Advektion von Wassermasseneigenschaften korrekt zu repräsentieren. Eine Ausnahme sind die hohen Breiten.
  - Verschiedene Mängel und Modellunterschiede sind in den Tropen und auch an den östlichen Ränder der Ozeane zu finden. Wir führen sie auf die unterschiedliche Darstellung der Rossbywellenausbreitung mit den unterschiedlichen Advektion-Diffusions-Schemata der Modelle zurück.
  - Austauschvorgänge mit den Randmeeren sind nach wie vor ein Problem der Ozeanmodellierung. Es manifestiert sich auch in unseren Modellen durch eine zu starke Vermischung des überströmenden Wassers. Bodengrenzschichtmodelle müssen präziser parametrisiert und eingesetzt werden.
  - Das GM Schema führt zu einer Verbesserung der Wassermassenverteilung im Modell, die Dicke der Thermokline und auch die Ventilationsraten einiger Wassermassen wird realistischer. Dies betrifft im wesentlichen das NADW.
  - Die verfügbare potentielle Energie (APE) wird allerdings zu gering und ein zu schwacher ACC stellt sich ein. Ekman-Pumpen und die mittlere Advektion ist zu schwach, um genügend APE zu erzeugen. Eine Feinabstimmung der Parametrisierungen erscheint unabdingbar.
  - Die Aufnahme von Spurenstoffen (in unserem Modell MOM2 teils durch künstliche Tracer repräsentiert) hängt stark vom Advektions-Diffusion-Schema ab, allerdings auch von den Anfangsbedingungen (d.h. von dem Zustand, der bei Beginn des Experiments vorlag). Der Südliche Ozean spielt eine herausragende Rolle in der Aufnahmefunktion, die Deaconzelle bestimmt in einem großen Maß den Gesamtinhalt und die räumliche Verteilung der Tracer.

- Vergleich der Zirkulation in den beiden Modellen MOM2 und HOPE:

  - Die Modelle ergeben eine sehr ähnliche Zirkulation und wir können nicht generell feststellen, daß eins 'besser' als das andere ist. Die Ergebnisse liegen im Großen und Ganzen nahe an der beobachteten Klimatologie, zum Teil sicherlich wegen der kurzen Integrationszeit.
  - Die Wärme- und Süßwasserklimatologien sind nicht geeignet, die Modelle zu verifizieren (oder falsifizieren), da die Ungenauigkeiten zu groß sind.

- Unterschiede in der thermohalinen Zirkulation des globalen Ozeans hängen stark von Unterschieden im Südlichen Ozean ab. Die Wassermassen nahe der Antarktis sind in beiden Modellen schlecht wierdergegeben. Zu geringe meridionale Dichtegradienten führen zu einem zu schwachen ACC. Probleme sind auch bei der Formation von Wassermassen auf den Schelfgebieten zu sehen. In den Antarktischen Randmeeren (Weddell- und Rossmeer) zeigen beide Modelle tiefreichende Konvektion, während die Schichtung eigentlich stabil sein sollte.
- Einige Wassermasseneigenschaften sind in MOM2 besser dargestellt, dies ist wahrscheinlich auf das verwendete FCT-Schema und die GM-Parametrisierung zurückzuführen. In früheren Experimenten mit HOPE wurde gefunden, daß GM in diesem Modell kaum zu Verbesserungen der Wassermassenstruktur führte.
- In der Arktis erscheinen großen Defizite in den Modellen. Der Export von Meereis durch die Framstraße ist zu gering und die Halokline im Arktischen Ozean ist zu dick.

Wir empfehlen eine längere Integrationszeit, um feinere physikalische Eigenschaften und Modellunterschiede sichtbar zu machen. Dabei sollte auf die Filterung in MOM2 verzichtet werden, da sie zu einer Verschiebung von Zirkulationmerkmalen in weiter südlich liegenden Bereichen führt (z.B. im Ostgrönlandstrom).

Chapter 2

The German OMIP project

The main objective of the present project is an intercomparison of current state-of-the-art ocean models with respect to the simulation of the mean state of the oceanic circulation and long-term variations of it, with emphasis on the global (and thus coarse resolution) models used in the German climate research community. The present contract concerned two general ocean circulation models but the original plan was to compare four models: the 'classical' GFDL model originated by Bryan (1969) and Cox (1975) and further developed as MOM, MOM2 and FSCC, and the newer models LSG, HOPE and OPYC (Maier-Reimer and Mikolajewicz 1992, Maier-Reimer et al. 1993, Wolff et al. 1997, Oberhuber 1993 a,b,c). For various reasons (mainly personnel problems and leaving of one model originator from the research community) we had to abandon the models LSG and OPYC. We also had to cancel the plans to incorporate studies of decadal variability with these models. In this report we describe the work with global versions of HOPE and MOM2 with respect to simulating the oceanic climatology, i.e. the mean annual cycle of the ocean circulation.

The study is part of the international project OMIP (Ocean Model Intercomparison Project). Other studies in this framework include various sensitivity investigations with particular models, as e.g. by Gerdes et al. (1991), and intercomparison between level and isopycnal models, as e.g. Chassignet et al. (1996), Roberts et al. (1996) and Marsh et al. (1996), and the DYNAMO Project (Dynamo Group 1997, Willebrand et al. 2000) which compared the performance of three high-resolution models of the North Atlantic. MOM was part in all these studies as well.

2.1 Aims of the project

The specific scientific and technical aspects of the present study are:

- to generate a parallel version of the MOM2 code which includes a sea ice module.
- to establish and use unified atmospheric forcing conditions for different ocean model configurations.
- to generate a set of atmospheric forcing fields which represents a typical annual period, from the ECMWF Reanalysis (ERA). This includes an improved handling of continental run-off and tuning of bulk formulae.
- to perform a detailed comparison of hydrographic conditions and circulation properties of the resulting ocean circulation in the models.
- to establish recommendations for global ocean modeling on the basis of our experiments.

The work was carried out at the MPI in Hamburg and the AWI in Bremerhaven, the computing was performed at the DKRZ and the computing center of AWI.

2.2 Achievements and problems in ocean modeling

It is generally accepted that the oceanic circulation has a profound influence on the mean state of the earth's climate and on climate changes on decadal and longer time scales. Large-scale transports of heat and fresh water by ocean currents are key climate parameters. The stratification and circulation in the upper ocean is crucial for the penetration and timing of the expected warming signal into the ocean. Vertical motions and water mass formation processes in high latitudes are an important controlling factor for the oceanic uptake of carbon dioxide through the sea surface and thus directly influence the radiative forcing in the atmosphere.

For quantitative predictions of climate change, three-dimensional ocean circulation models are a necessary which are able to simulate the present circulation and water mass distribution, including their seasonal variability, with sufficient accuracy. The main problems in ocean circulation modeling arise from uncertainties in the parameterization of unresolved motions, from insufficient spatial resolution, and from poor estimates of air-sea fluxes. Despite a long history of intensive oceanographic research ocean modeling is much less advanced than atmospheric modeling though oceanic physics are generally less complex than atmospheric physics. However, many important processes in the ocean are not directly observable and thus less understood.

Most large-scale models are based on the Primitive Equations (PE), following the work by Bryan (1969). A number of models have been based on the code developed at GFDL Princeton by M. Cox and further expanded by a large community, and some new developments (LSG, HOPE and OPYC) have been achieved by the model builders at the MPI in Hamburg. For the performance of these models on decadal and longer time scales, an accurate parameterization of subgrid-scale mixing of heat and salt is extremely important. New schemes have recently been proposed and tested in the models. The mixing rate controls the amount of vertical overturning and water mass formation in high latitudes. The main contribution to poleward heat transport arises from vertical overturning, whereas the contribution associated with the horizontal gyre-scale circulation is somewhat smaller.

The underestimation of the heat transport by most models can be related to the resolution. Models with finer resolution have an enhanced heat transport than those with coarser resolution. In coarse models not only the strength of the western boundary currents is less than observed but also the observed separation of the Gulf stream is not at the right place. The thermocline in these models is generally warmer and more diffusive than observed.

The observed hydrographical parameters temperature, salinity and other water mass properties are the primary information for the validation of ocean models. Analysed data sets (e.g. Levitus, 1982, Levitus and Boyer, 1994, Levitus et al. 1994) have been very practical. The poleward transport of heat in the ocean is itself not a well-observed variable, and estimates from zonal hydrographic sections continue to have the highest reliability. Direct observations of the fluxes of heat and fresh water at the sea surface are not very accurate. Satellite altimeter observations have improved their accuracy and become an important tool to monitor the circulation on longer time scales.

Many specific recent developments in sub-grid scale parameterizations and in numerical techniques have been implemented in the models used in this intercomparison. They are described in the next section. Advances in establishing improved model forcing are discussed in section 5.

2.3 Summary of results

OMIP is an international effort to compare and improve Ocean General Circulation Models (OGCM). The present project contributes with an intercomparison of two global OGCMs (with sea ice), the MOM2 of the GFDL family of models and the HOPE model of the MPI Hamburg. The intercomparison is restricted to the mean annual cycle in these models, obtained with the same forcing functions in form of parameters of a mean seasonal cycle with typical daily fluctuations superimposed, derived in this project from the ECMWF Reanalysis ERA. The report presents a description of the models, the obtained forcing functions, some technical achievements

for the parallelization of MOM2 with a sea ice module, some preparatory control experiments and the resulting ocean circulation in the intercomparison experiments.

The results of the project are briefly summarized in the following. Extended interpretations of results can be found in the sections 6.1 and 7.10.

- TECHNICAL ACHIEVEMENTS

  The parallelization and scalability of the MOM2 Model with the coupled sea ice model has been greatly enhanced within the scope of the OMIP project. This is of some importance, as the regular domain decompositioning approach adopted here, where subdomains can be defined in longitudinal as well as latitudinal direction for optimal load balance, has not been aimed for in the parallelization of the forthcoming GFDL MOM3 model release, which still will be restricted to only a one dimensional domain decompositioning approach.

  Another advantage of this parallelization approach is, that the basic concept of the memory window is still used in the parallel code, which gives the MOM user the possibility for parallelizing over the memory window. This gives a high memory saving possibility and allows the user to calculate model configurations with much more grid points. The good scalability which has been demonstrated in the OMIP parallel MOM2/sea ice version further supports such an undertaking. Furthermore some preliminary work was also done for the investigation of coupling strategies with an atmospheric model. Here special attention was given to study the future use of external flux couplers (e.g. NCAR flux coupler) and the feasability of flexible coupling strategies in the parallelized version of the MOM2/seaice model.

- FORCING FUNCTIONS

  The forcing data have been derived from the data produced by the European Centre for Medium-Range Weather Forecasts (ECMWF) in the re-analysis project ERA. A mean annual cycle from the 15 years of ERA with daily fluctuations superimposed has been produced. Fresh water fluxes over the continents have been transformed into runoff by using a simple scheme based on catchment areas and main drainage basins. The heat and fresh water budgets of the forcing data have been closed independently of the ocean models.

- SENSITIVITY EXPERIMENTS WITH MOM2 IN SECTION 6.1

  - Advective signals associated with major water masses can be well represented at 2°horizontal resolution. The large scale water mass structures are generally well reproduced.
  - Different deficiencies exist in the tropics and eastern parts of the mid-latitudes; these problems are possibly associated with Rossby wave dynamics with different advection-diffusion schemes
  - Exchanges with adjacent seas represent a still unsolved problem (under extreme conditions) that is aggravated by the excessive mixing of overflow waters with ambient waters. Bottom boundary layer parameterizations could ameliorate this problem.
  - The Gent-McWilliams (GM) scheme provides a better representation of water masses by reducing thermocline thickening and additional ventilation (through eddy induced transports) of certain water masses. This includes the NADW. Ekman pumping and mean circulation are not sufficient to re-supply the APE that was removed by the GM scheme. One consequence is a weak ACC. Diapycnal mixing can enhance the APE supply, however, water masses like the AAIW are negatively affected. Together, this defines a need for a deeper understanding of the interaction of different parameterizations that could result in a finer tuning of the available schemes.
  - Tracer uptake of the ocean depends on the advection-diffusion scheme used. The Southern Ocean plays the most important role in the tracer uptake function of the ocean. The Deacon cell determines inventory and spatial distribution of tracers.

  - Water mass formation processes in high latitude Southern Ocean seas are deficient in all model versions.

- MAJOR DIFFERENCES IN THE CIRCULATION IN THE INTERCOMPARISON EXPERIMENTS OF MOM2 AND HOPE
  - The model results are very similar, most of the time we cannot decide which result is better based on the available data sets. The model results are close to climatological fields in many cases.
  - The heat flux climatologies are not suited to verify models (perhaps the other way round) because the uncertainties are too large. The same holds even more so for the climatologies of the fresh water fluxes.
  - The Southern Ocean is of great importance for the differences between the models, e.g. the upwelling branch of the THC. Water mass properties near Antarctica are flawed in the models. The low meridional density difference leads to weak ACC transports. Problems exist with water mass formation and transport off the shelves. Deep convection occurs in the interior of the Weddell and Ross seas where the stratification should be stable.
  - The Gent-McWilliams parameterization has mixed effects on the model results.
  - Longer integration times are necessary to assess the more subtle differences in model physics. Filtering should be avoided because it contaminates downstream (lower latitude) results (e.g. East Greenland Current in MOM2).
  - Some water mass properties and distributions are superior in MOM, probably a consequence of both, the FCT advection scheme and the GM parameterization.
  - Pronounced model - data discrepancies exist in the Arctic. Exchanges between the Arctic and neighboring oceans must be improved. The sea ice export is far too low. This is one reason for the thick halocline that will result in reduced sensitivity to climate forcing.

2.4 Acknowledgements

We gratefully acknowledge the support from BMBF and the assistance by the GFDL-MOM-Group, the MPI-HOPE group, the DKRZ, and the computing center of AWI. We also express our gratitude to the scientific staffs of the Max-Planck-Institute for Meteorology and the Alfred Wegener Institute for Polar and Marine Research for their help and interest. NCEP re-analysis data were provided by the NOAA-CIRES Climate Diagnostics Center, Boulder, Colorado, USA, from their Web site at http://www.cdc.noaa.gov/. DO acknowledges support from IMAU, University of Utrecht, while preparing this report during an extended stay.

Chapter 3

The numerical models MOM and HOPE

Both models of this study follow the traditional route of ocean modeling. They use the Primitive Equations (PE) to represent the dynamics and thermodynamics of large-scale ocean circulation, focussing on the simulation of water mass formation and transport as reaction to forcing by winds and exchange of heat and freshwater with the atmosphere. In addition, the numerical realization of the model equations is standard as well, the model codes are formulated in level (geopotential) coordinates on a sphere and allow for a realistic geometry of the oceanic basins and bathymetry. Advection terms are formulated in central differences. A major difference between HOPE and MOM2 is the handling of the ocean surface which is treated the traditional rigid-lid approximation MOM2 while HOPE has a free surface with an implicit code for computing the barotropic part of the dynamics. The model configurations used here have coarse resolution, thus not permitting any meso-scale eddy activity to mix and transport oceanic properties. Subgrid-scale processes are parameterized by current-state-of the-art algorithms. Whereas MOM2 exists in a parallel version – and is used here in this form, the parallelization of the sea ice module is part of the present project – the HOPE is not parallelized.

Both models, in particularly MOM2, have a long list of applications in oceanic and coupled modeling and have proved to yield realistic mean circulations. Nevertheless, there are many problems, as described the previous section. Some previous and additional studies are discussed in section 6 below. This section describes the physics and numerics of the models.

3.1 The Modular Ocean Model MOM

MOM continues a long tradition of three-dimensional ocean models developed at the Geophysical Fluid Dynamics Laboratory (GFDL) at Princeton (Bryan, 1969, Cox, 1984, Pacanowski et al. 1991, Pacanowski, 1996, Pacanowski and Griffies, 1999). MOM and its predecessors are widely used by many groups and for different purposes ranging from regional modeling (e.g. Beckmann et al., 1994) to global modeling (e.g. Danabasoglu and McWilliams, 1995, England, 1993). It has been used as the oceanic component for coupled climate models (e.g. Manabe and Stouffer, 1994; Philander et al., 1992) and several ocean GCMs derive from the basic GFDL design (e.g. Semtner and Chervin, 1988). Like HOPE, MOM is a finite difference version of the primitive equations. As described by Bryan (1969), the equations consist of the Navier-Stokes equations subject to the Boussinesq, hydrostatic, rigid lid, and thin shell approximations along with a nonlinear equation of state. The approximations involved in the primitive equations are discussed in detail by Müller and Willebrand (1985).

MOM contains a large number of numerical options, alternative parameterizations for subgrid-scale processes, and diagnostic options. Criticism of earlier versions of the model (staircase topography, high diffusivity) have been addressed in the current version by a partial bottom cell

topography (Pacanowski and Gnanadesika, 1998), bottom boundary layer algorithms (Beckmann and Döscher, 1997), and the implementation of alternative advection schemes (Gerdes et al., 1991, Hecht et al., 1995). In this project, the model was coupled with a thermodynamic-dynamic sea ice model with viscous-plastic rheology (Hibler, 1979). The sea ice model is similar to the sea ice model used in HOPE (described below, see section 3.2). However, the coding and the treatment of the momentum equation follow Kreyscher et al. (1997). The coupling procedure is that of Hibler and Bryan (1987) and differs from that in HOPE. Here, the ocean model predicts the total mass transport in the uppermost level, including the sea ice component. The forcing is due to the wind stress and the internal stresses generated in the sea ice. We assume that the wind stresses over ice and ocean are the same. This assumption, however, is not crucial and could be relaxed without difficulty. An ocean-ice drag does not appear in the momentum equations for the ocean model because the ocean-ice boundary is internal to the uppermost grid box of the ocean model. This treatment ensures that the total Ekman transport is considered in the ocean model. The vertical velocity at the bottom of the uppermost model level thus reflects the divergence of the total mass transport, not only that of the oceanic component. The adaptation of MOM for massively parallel computers (described in section 4) was the other major modification of MOM that was performed in this project.

The version 2 of MOM, MOM2, that is used in the model intercomparison experiments is described in the comprehensive documentation by Pacanowski (1996). We shall here restrict the discussion to a description of the options utilized in the comparison experiments of section 7 and especially those that lead to differences in the physical description of the system compared to HOPE. Other options have been used for the sensitivity studies of section 6.1 and are described there. Common aspects of HOPE and MOM, especially the specification of surface fluxes, are given in section 5.

Time stepping in MOM is usually done with a time-centred Leapfrog scheme. Time splitting characteristics are suppressed by occasionally applying a mixing scheme. For that purpose we use an Euler backward scheme every 19 time steps. The time steps differ among prognostic variables; the external (barotropic streamfunction) and internal modes are both stepped forward with 1200 sec. The tracer equations, on the other hand, use a time step of 6 hours. This technique, called 'distorted physics' by Bryan (1984), effectively slows down barotropic and internal gravity waves. It also affects the baroclinic instability in the model. However, advection and baroclinic Rossby waves, the most important processes of signal spreading in coarse resolution models, are virtually unaffected (Bryan, 1984). The ice model uses the tracer time step of the ocean model.

The model spans the global ocean including major marginal seas like the European Mediterranean, the Arctic Ocean, and Hudson Bay. The horizontal resolution is T63 (slightly better than 2°) and thus corresponds to the horizontal resolution in HOPE. In the vertical, the model contains 29 levels of unequal spacing (see Table 7.1). The vertical resolution is somewhat higher than for HOPE to compensate for the better representation of topography due to the partial cells available in HOPE. The newly available option of partial cells in MOM was not utilized here because most climate models are run with the full cells of previous versions of MOM. The discretization with full cells in the vertical is one of the characteristics of the model and has been widely criticized recently.

The bottom topography was derived from the ETOPO5 data set by averaging the depths from the 5' squares of the data set that fall into one model grid box. No further adjustments were applied with the exception of the Straits of Gibraltar and some modification of the Greenland-Scotland Ridge. The Straits of Gibraltar were opened to contain at least two active tracer grid boxes so that an advective exchange between the Atlantic and Mediterranean is possible. The amount of Mediterranean water that enters the Atlantic can not be determined a priori from the chosen width and depth of the passage. In our case, we obtained a too large outflow of saline water into the Atlantic in the final comparison experiment (see section 7). However, we decided to keep the topography of the initial experiments (section 6.1) to allow direct comparisons. The Greenland-Scotland Ridge was made deeper at the Denmark Strait and at the Faeroe Bank Channel where the averaging from the ETOPO5 data set yielded too shallow passages connecting the Nordic Seas with the Atlantic proper.

The spherical coordinates of the model grid lead to very small zonal grid distances near the poles. This is especially critical in the Arctic. Here we filter the prognostic variables of the ocean model such that effectively only length scales of larger than two zonal grid distances at 78° N are retained.

Friction is implemented as a simple Laplacian mixing term (the second r.h.s. term in equation (3.2) below) with a constant horizontal mixing coefficient of $A_H = 10^5 \mathrm{m}^2\mathrm{s}^{-1}$ and $A_V = 10^{-3}\mathrm{m}^2\mathrm{s}^{-1}$ for vertical mixing of horizontal momentum. The side walls are no-slip boundaries while the bottom is a free-slip surface (no bottom friction).

The tracer equations are implemented with the FCT advection scheme (Zalesak, 1978, Gerdes et al., 1991) that includes (small) implicit diffusion. By construction, this implicit diffusion is sufficient to avoid false extrema in the advected quantities. Additional mixing for numerical purposes is not necessary (a fact exploited in the V1.2 experiment of section 6.1). Explicit diffusion of tracers is provided by mixing in locally defined neutral directions. A small angle approximation is used to suppress small off-diagonal elements in the tensor that defines the rotation of the diffusive fluxes from the coordinate directions. No background diffusion in coordinate directions is used. The isoneutral diffusion coefficient is $A_I = 5 \times 10^2 \mathrm{m}^2\mathrm{s}^{-1}$. Diffusion in neutral directions is reduced should the slope of these directions becomes too large to be numerically stable at the chosen time step. The re-scaling of Gerdes et al. (1991) is used with a critical slope above which the limitation sets in of $sl_{max} = 0.01$. We employ the Gent and McWilliams (1990) parameterization for eddy induced transport velocities to include the effect of mesoscale eddy generation on the tracer distributions. Here we use the same (thickness diffusion) coefficient A_I as for isoneutral diffusion.

Diapycnal mixing is here restricted to Laplacian mixing with a prescribed diffusion coefficients that increase from $0.3 \times 10^{-4}\mathrm{m}^2\mathrm{s}^{-1}$ at the surface to $1.3 \times 10^{-4}\mathrm{m}^2\mathrm{s}^{-1}$ at the lowest level according to an arctan profile (Bryan and Lewis, 1979). There is no explicit mixed layer scheme used in our experiments. Deep winter mixed layers due to statically unstable stratification are generated by a convection scheme. Here, we use Rahmstorf's algorithm that completely removes static instability from the water column in one pass. Unstably stratified boxes are mixed during this procedure.

3.2 The Hamburg Ocean Primitive Equation model HOPE

Compared to the GFDL-MOM family of models the Hamburg Ocean Primitive Equation general circulation model HOPE is a quite young development. We use a global version which is the oceanic component in a coupled general circulation model (CGCM) (Frey et al. 1997, Venzke et al. 2000) with the same horizontal resolution as the model described here. The version used in this project has as addition the sea ice component. In a coarser global version, it was used in studies of the impact of sea ice on deep ocean water-mass characteristics (Stössel et al. 1998, Kim and Stössel 1998), and long-term simulations of natural variability (Kim et al. 1998, Stössel and Kim 1998, Drijfhout et al. 1996). Regional studies with higher resolution have been conducted by Marsland and Wolff (2000).

The model is described in detail in Wolff et al. (1997). It is formulated on horizontal (z-) surfaces. The prognostic variables are horizontal velocities $\boldsymbol{v}$, potential temperature θ and salinity S, and sea-surface elevation ζ. These variables are calculated from the non-linear horizontal momentum equations, conservation equations for heat and salt, and the continuity equation for an incompressible fluid. The baroclinic pressure p is calculated from the hydrostatic equation using a nonlinear equation of state (UNESCO 1983), and the Boussinesq approximation.

The momentum equations

$$\frac{d}{dt}\boldsymbol{v} + f\boldsymbol{k} \times \boldsymbol{v} = -\frac{1}{\rho_0}\boldsymbol{\nabla}(p + \rho_0 g\zeta) + \boldsymbol{F}_H + \boldsymbol{F}_V. \tag{3.1}$$

include parameterizations for horizontal and vertical turbulent viscous momentum dissipation $\boldsymbol{F}_H$ and $\boldsymbol{F}_V$. The horizontal viscous dissipation $\boldsymbol{F}_H$ is composed of a term depending on the local rate of strain and of harmonic and biharmonic background terms,

$$\boldsymbol{F}_H = \boldsymbol{\nabla} \cdot (\nu_A T^2 \boldsymbol{\nabla} \boldsymbol{v}) + A_H \nabla^2 \boldsymbol{v} - B_H \nabla^4 \boldsymbol{v}, \tag{3.2}$$

with constant coefficients $A_H = 150\mathrm{m}^2\mathrm{s}^{-1}$ and $B_H \cdot \Delta t/(\Delta x)^4 = 10^{-3}$. The coefficient T^2 at time step n is composed of the squared strain rate at time step n and of T^2 at the previous time step: $(T^2)^n = \lambda_{T1}(v_x^n + u_y^n)^2 + \lambda_{T2}(T^2)^{n-1}$. With the model time step $\Delta t = 2\mathrm{h}$ and with $\lambda_{T2} = 0.9$, this defines a viscous memory time scale of 20 h. The other two coefficients are $\lambda_{T1} = 0.1$ and $\nu_A = 4.5 \cdot 10^{15} \cos\phi\, \mathrm{m}^2\mathrm{s}$, where ϕ denotes the latitude. At lateral walls and at the bottom, Newtonian friction is applied in addition to no-slip conditions. At lateral boundaries the Newtonian-friction coefficient is of the size of the Coriolis parameter, whereas at the bottom, the coefficient is constant ($= 10^{-7}\mathrm{s}^{-1}$).

The vertical eddy viscosity term

$$\boldsymbol{F}_V = \frac{\partial}{\partial z}\left(A_V \frac{\partial \boldsymbol{v}}{\partial z}\right) \tag{3.3}$$

also depends on the ocean state at the previous time step as well as on the actual state of the ocean. The eddy coefficient A_V includes a term accounting for shear instability with a dependence on the local Richardson number $\mathrm{Ri} = -g\rho_0{}^{-1}\partial\rho/\partial z \cdot [(\partial u/\partial z)^2 + (\partial v/\partial z)^2]^{-1}$ in a way similar to that proposed by Pacanowski and Philander (1981), a simple mixed-layer parameterization, and a background term representing mixing by internal wave breaking:

$$A_V^n = (1-\lambda_V)A_V^{n-1} + \lambda_V \left[A_{V0}(1 + C_{RA}\mathrm{Ri})^{-2} + \delta_{\Delta\rho} W_\rho + A_b\right]. \tag{3.4}$$

λ_V is set to 0.4, corresponding to a decay time of 4 hours. C_{RA} is set to $5 \cdot l/4$, where l is the number of neighboring wet grid cells. The vertical eddy viscosity is thereby increased near lateral boundaries. In addition, $10^{-3}\mathrm{m}^2\mathrm{s}^{-1}$ is added to the final value of A_V at the lower boundary of each water column. Both formulations serve to simulate stirring by topographic features. The value for small Richardson numbers is $A_{V0} = 2.5 \cdot 10^{-3}\mathrm{m}^2\mathrm{s}^{-1}$.

The term $\delta_{\Delta\rho} W_\rho$ symbolizes the mixed-layer parameterization. In cases of weak surface stratification, i.e. when the density difference $\Delta\rho$ between the surface layer and an underlying layer is smaller than a critical value ($\Delta\rho < 7.7 \cdot 10^{-6}\rho_0 \Delta z_1 \mathrm{m}^{-1}$), the vertical eddy viscosity coefficient is increased by $4 \cdot 10^{-3}\mathrm{m}^2\mathrm{s}^{-1}$ multiplied by a vertical decay coefficient of 0.4^k, where k is the level index. The critical value is set according to Latif et al. (1994) who tuned it to give the best results in the tropical Pacific. However, we use density instead of temperature differences for the mixing criterion, so that the formulation can be applied also at high latitudes. The background viscous coefficient A_b is set to $5.0 \cdot 10^{-5}\mathrm{m}^2\mathrm{s}^{-1}$. High values of the total vertical eddy viscosity coefficient can diffusively propagate into the interior.

The momentum flux through the sea surface is composed of the interfacial air/water and sea ice/water stresses, applied to the ice-free and ice-covered part of each grid cell, respectively. The air/water stress $\boldsymbol{\tau}_a$ has been taken from the ECHAM4 atmospheric general circulation model for the developing phase of the model (see section 6.2), while the ice/water stress $\boldsymbol{\tau}_o$ is calculated with a quadratic drag law: $\boldsymbol{\tau}_o = -\rho_0 c_w |\boldsymbol{v}_1 - \boldsymbol{v}_I|(\boldsymbol{v}_I - \boldsymbol{v}_1)$ with drag coefficient $c_w = 5.5 \cdot 10^{-3}$. Here, $\boldsymbol{v}_1$ is the velocity in the uppermost ocean layer. The two-dimensional ice velocity $\boldsymbol{v}_I$ is calculated from a momentum balance equation, in which the advection terms are neglected:

$$\frac{\partial}{\partial t}\boldsymbol{v}_I = -f\boldsymbol{k}\times\boldsymbol{v}_I + \frac{\boldsymbol{\tau}_a}{\rho_I h_I'} + \frac{\boldsymbol{\tau}_o}{\rho_I h_I'} + \frac{\boldsymbol{F}_I}{\rho_I h_I'} - g\boldsymbol{\nabla}\zeta. \tag{3.5}$$

where $\boldsymbol{F}_I$ is the force due to the internal ice resistance. It is formulated as in Hibler (1979), i.e. it has a viscous-plastic constitutive law with an elliptical yield curve. The terms ρ_I and h_I' are the density of the sea ice and the ice thickness, respectively.

Salinity and potential temperature are determined from conservation equations including vertical and horizontal eddy diffusivity parameterizations,

$$\begin{aligned}\frac{dS}{dt} &= \frac{\partial}{\partial z}\left(D_V\frac{\partial S}{\partial z}\right) + D_H\nabla^2 S + \boldsymbol{\nabla}\cdot(\nu_D T^2\boldsymbol{\nabla}S)\\ \frac{d\theta}{dt} &= \frac{\partial}{\partial z}\left(D_V\frac{\partial \theta}{\partial z}\right) + D_H\nabla^2\theta + \boldsymbol{\nabla}\cdot(\nu_D T^2\boldsymbol{\nabla}\theta)\end{aligned} \tag{3.6}$$

where $\nu_D = 5.5\cdot 10^{14}\mathrm{m^2 s}$ and $D_H = 1.5\cdot 10^3\mathrm{m^2 s^{-1}}$ are constant coefficients, and T^2 is defined as for the horizontal viscosity. All parameterizations of temperature and salinity diffusion conserve heat and salt, respectively. The vertical eddy diffusivity D_V depends on the local Richardson number in a similar way as the vertical eddy viscosity:

$$D_V^{n+1} = (1-\lambda_V)D_V^n + \lambda_V \max[D_{V0}(1+C_{RD}Ri)^{-3} + \delta_{\Delta\rho}0.5W_\rho, D_b]. \tag{3.7}$$

This formulation slightly deviates from that used by Latif et al. (1994). We kept their parameterization of the background diffusion with a constant coefficient $D_b = 10^{-6}\mathrm{m^2 s^{-1}}$ in the upper ocean, but specified it to depend on depth below 500 m, using the profile of Bryan and Lewis (1979). D_{V0} and C_{RD} are $2.5\cdot 10^{-3}\mathrm{m^2 s^{-1}}$ and $5\cdot l/4$ respectively, they thus have the same values as in the vertical dissipation of momentum. At large depths, the net coefficients amount to the background values.

At the lateral boundaries and at the sea floor, zero-flux conditions are used. Surface salinity changes according to internal dynamics by advection and diffusion, and to dilution by freshwater fluxes through the free surface. The latter includes precipitation, snow fall over open water, snow melt, sea ice growth or melt, continental runoff, and evaporation. The sea-surface elevation ζ is a prognostic variable. It is calculated from the vertically integrated conservation of mass (volume in the Boussinesq approximation)

$$\partial\zeta/\partial t = -\boldsymbol{\nabla}\cdot\int_{-H}^{0}\boldsymbol{v}dz + Q_\zeta \tag{3.8}$$

where H is the water depth, and Q_ζ the total net freshwater flux through the surface.

Heat fluxes are calculated separately over the ice-free and ice-covered part of each grid cell. The surface heat-flux calculation over open water depends on whether the grid cell is located in an ice region or not. The ice is considered to be a two-dimensional slab floating on the water. Continuity equations are solved for the concentration A_I, the grid-cell-mean ice thickness $h_I = h_I' A_I$, and snow depth h_S. Source terms for the mean ice thickness or ice volume are calculated according to the net heat flux through the ice-free part of the grid cell, the conductive heat flux through the snow/ice cover, and surface melt. Net upward heat flux through the ice-free part of the grid cell is interpreted as new-ice growth when the upper ocean temperature is at freezing point. In

this case, the ice concentration is also changed assuming that new ice is formed with a thickness of 50 cm. The conductive heat flux through the snow/ice cover is proportional to the inverse effective ice thickness and the difference between the skin temperature and freezing point. The skin temperature is calculated from a heat balance equation. The effective ice thickness includes the snow depth and accounts for the different thermal insulation properties of snow and ice. Snow accumulates on the sea ice when the net atmospheric freshwater flux is downward and the near-surface air temperature is below freezing point. It melts when the calculated skin temperature is above freezing point. When no more snow is present at melting conditions, surface melt of the sea ice starts. For more details see the technical report of Wolff et al. (1997).

In cases of unstable stratification, convective adjustment is applied. Each pair of vertically adjacent unstably stratified grid boxes is mixed, with heat and salt being conserved. Only one swap is done at each time step. The freezing and melting of sea ice is associated with fluxes of salt and water through the water/ice interface. The corresponding changes of sea surface salinity under freezing conditions destabilize the upper water column and may initiate convective adjustment. In the weakly stratified Southern Ocean, this process acts as an upward pump of heat and salt, but it is confined in nature to the upper ocean in deep water (Martinson 1990). A salinification of bottom water is supposed to occur only in shallow shelf areas. In large-scale OGCMs, convective adjustment is often too strong in the Southern Ocean, and this destroys the weak stratification. The adjustment is therefore switched on only if the density gradient $-\partial\rho/\partial z$, evaluated at the interface between two layers, exceeds the critical value of $0.6 \cdot \rho_0 \cdot 10^{-12}\mathrm{m}^{-1}$. This is the largest value that could be used without generating instabilities in the equatorial region.

It is still in debate whether the sinking of dense surface water after haline rejection during the freezing of sea ice occurs in filaments without much dilution, or whether the entire surface column beneath the ice is convectively stirred. In any case, neither a 'rain' of brine-enriched surface water nor local downslope motion of dense water is resolved in the present model. We choose to distribute the salinity increase, associated with freezing of ice, to the upper two layers of the ocean (70% is left in the surface layer). This partially decouples the surface layer from the adjustment process and improves the deep and bottom water characteristics (Legutke et al. 1997). A similar formulation has been used in Maier-Reimer et al. (1993).

Both the ocean and sea ice equations are discretized on an Arakawa-E type grid (Arakawa and Lamb 1977). The model domain includes the Baltic and Mediterranean Seas, as well as the Hudson and Baffin Bays. The Arctic Ocean is connected to the Pacific by the Bering Strait, and to the Atlantic by the Denmark Strait and the Iceland- Scotland Passage. Besides the continental land masses of America/Greenland, Africa/Eurasia/Indonesia, Australia/New Guinea, and Antarctica, there are 5 additional islands. These are Svalbard, Iceland, New Zealand, the Philippines, and Madagascar. The northernmost grid cell is treated as an island as well. At its lateral walls, a no-slip condition is applied for the ice velocity. The zonal density gradients are set to zero near the pole, and the baroclinic velocity is computed from geostrophy to avoid fast internal waves in this region.

The vertical levels are concentrated in the upper ocean with 12 layers above 500 m. A good resolution of the topography, however, is guaranteed since the model formulation allows for partial grid cells at the bottom. The height of the lowermost grid box is specified such that the accumulated height of all boxes at each grid point is equal to the local observed water depth. Thus, the resolution of the bottom topography is limited by the horizontal resolution of the grid only, but not by the number of computational levels. The baroclinic pressure is computed at a constant depth for each layer, and thus does not induce spurious bottom-pressure terms. It has been shown that this formulation gives a smoother flow field above topographic features (Adcroft et al. 1997).

Chapter 4

Parallelization and scalability of the MOM2 model and technical framework for the ocean/sea ice coupling

To get reliable comparisons in the scope of OMIP, simulations with the models should run for about 100 years or more. This implies the use of high end supercomputers. The parallelization ofa model such as MOM2 – which was originally optimized for vector machines – requires to solve the following problem. On the one hand, the performance of the programme should be as high as possible. On the other hand, the modifications in the code have to be as small as possible to ensure the acceptance of the parallel code by the user community.

MOM itself has a modular structure and allows the user to choose the physics to be implemented in the simulation. At the beginning the model configuration must be defined. This includes the grid and topography, initial and surface boundary conditions, the convection and subgrid-scale mixing schemes. With the accordant options for the preprocessors the specific model code is obtained. Typical length of such a model configuration, as in OMIP, is about 100.000 up to 150.000 lines of code.

The model is based on Reynolds-averaged Navier-Stokes-equations and the corresponding thermodynamical balances. The prognostic values (velocity, salinity, temperature) are treated in different parts of the programme. The velocities are splitted into the vertical averages and the deviations. The calculations of the average - the barotropic part - can be formulated via an elliptic equation of Helmholtz-type for the 2D streamfunction. This is solved by a preconditioned conjugate gradient method. For calculation of the baroclinic part of the velocities and the tracers an explicit time stepping scheme is used. For each time some 2nd or 4th order nonlinear partial differential equations are to be solved.

The flow chart for the original programme is given in Figure 4.1. It starts with an initialization section and ends with some diagnostics and output. In between, the time integration is done in the outer time stepping loop. This loop includes all parts of the programme where new prognostic values are calculated. There is an extra loop over those sections where the 3D equations are solved, the memory window loop. Most of the time is spent in this memory window loop. Only 5 to 10 % are used for solution of the barotropic equation.

The basic concept of the memory window is still used in the parallel code because of the following reasons: at first it provides the MOM user with the possibility for parallelizing over the memory window by means of a simple 1D domain decomposition. At second, a lot of intermediate values needed for calculation of the new time step are calculated in this memory window. Therefore, these arrays have to be dimensioned only to the size of the memory window and not to the

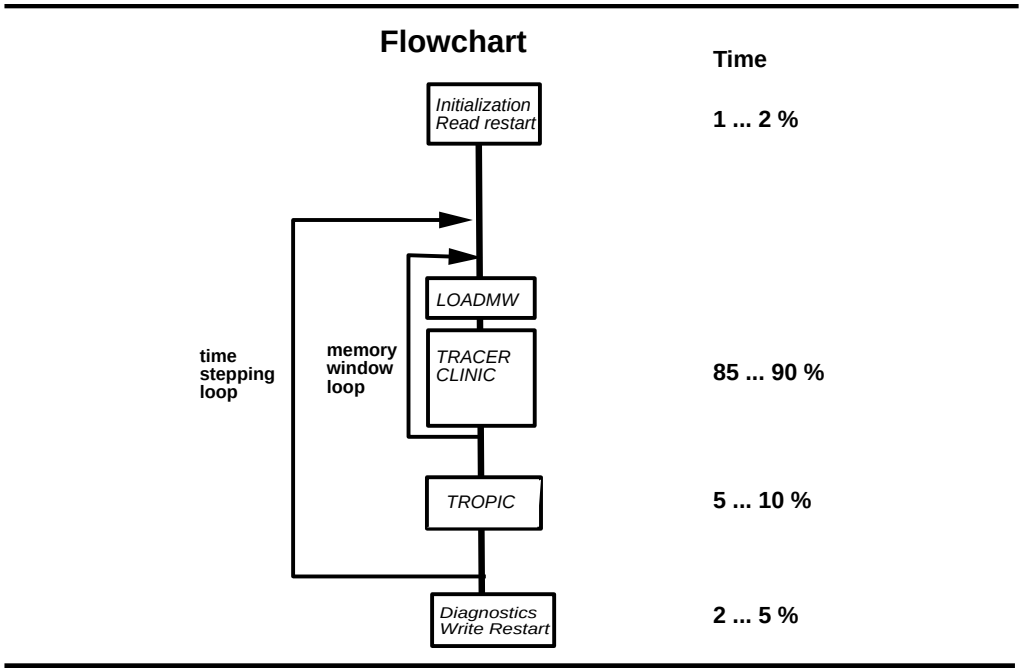

Figure 4.1: Flowchart and computing times for MOM2.

size of the whole computational area. This implies a high memory saving possibility and allows to calculate model configurations with much more grid points.

Figure 4.2 shows the memory window technique for the simplest case, where the algorithm needs only information from the first neighbor points. The first 3 rows must be loaded from disk to memory. Then the calculation of the new values on row 2 starts (assume mixed boundary conditions). The new state values are stored back on disk. Then the memory window is shifted and the next row is loaded from disk. Now new state values on row 2 of the memory window are calculated. The procedure is continued by storing the new values on disk, shifting the memory window, loading new row from disk, and so on.

For parallelizing we use the domain decomposition technique. As mentioned above for the baroclinic velocities and the tracers we have to solve 3D equations, for the barotropic part only a 2D equation. The numerics implemented into the model uses local operators in the $x-y-$plane. This means that information is needed only about some neighbors of the actual grid point. For 2nd order algorithm it suffices to have information of the first nearest neighbors, for 4th order algorithms one needs the second nearest neighbors, too. And a special case - the flux corrected transport algorithm - needs even more neighbored grid points.

The physics in z direction is much more complicated. Convection can require to exchange information inside the whole water column. Therefore we use a 2D domain decomposition in the $x-y$-plane. The calculations are carried out over all grid points. Then they are multiplied with a land sea mask to get the right values only on wet (water) grid points. Therefore, load balancing problems are generally avoided which might come from the topography, and we can use an uniform distribution of work on the processors. Since the most inner index for calculation the 3D arrays in the memory window is in E-W-direction the number of processors in this direction should be kept small to prevent too small inner loops.

The parallelized programme looks like shown in Figure 4.3. It begins with some global initializations. The first processor reads the restart file and broadcasts all information to the other processors. Then all processors initialize some arrays in its subdomains and allocate the memory

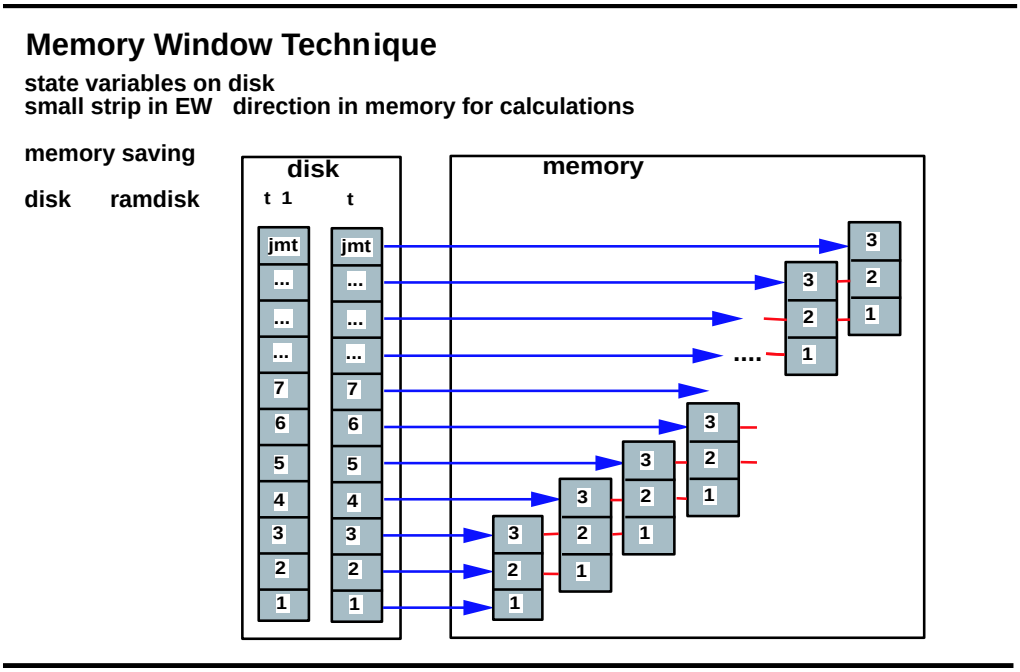

Figure 4.2: MOM2: memory window technique.

for the ramdisk. Each processor can now execute the memory window loop on its subdomain, independent on the other processors. For testing purposes there is an option for solving the barotropic equation in a sequential manner. For this case one has to exchange the results of TRACER and CLINIC and then start to execute the sequential TROPIC. Otherwise no additional communication is needed at this moment and the parallel TROPIC is called. Apart from TROPIC, communication is needed only once per time step, where the values of the borders are exchanged between neighboring processing elements (PE). This is illustrated schematically in Figure 4.4. Each PE holds ramdisk values which includes the values on the grid points of its subdomain and - depending on the order of the algorithm - some ghostpoints. These borders have to be exchanged for each time step. The communication necessitates the fast CRAY Shmem-put/get routines. This implies that the ramdisk has to be allocated via shpalloc.

Parallelization of the sea ice model is not so difficult, as the sea ice model is structured much simpler than the ocean model. The flowchart of the sea ice model (Figure 4.5) shows that the main time is spent in a routine DRIFT, where the momentum equation is solved. This is done originally by a red-black-relaxation. The formulation of the model is 2-dimensional. So we can use a 2-dimensional domain decomposition approach such as in MOM2.

But in general, sea ice covers only a part of the considered ocean region. Especially for the global model configurations in OMIP this is the case. Therefore, a reasonable subdomain must be defined as working region for the ice model. This implies either redistribution of data when going from ice model to ocean and vice versa or load imbalance.

The coupling between ice and ocean is performed via surface boundary conditions. These are some 2D arrays like the surface velocity of the ocean (which determine the drift forces of the ice) or the atmospheric heat flux modified with the melt (which implies the surface temperature of the ocean). The coupling interface is programmed up to now only via the first PE which gathers all information in the actual submodel and scatters it in the other submodel.

Modifications in the code have to be done only on some locations. We have to include a new subroutine, named here 'setup-parallel', where all values are calculated which we need for

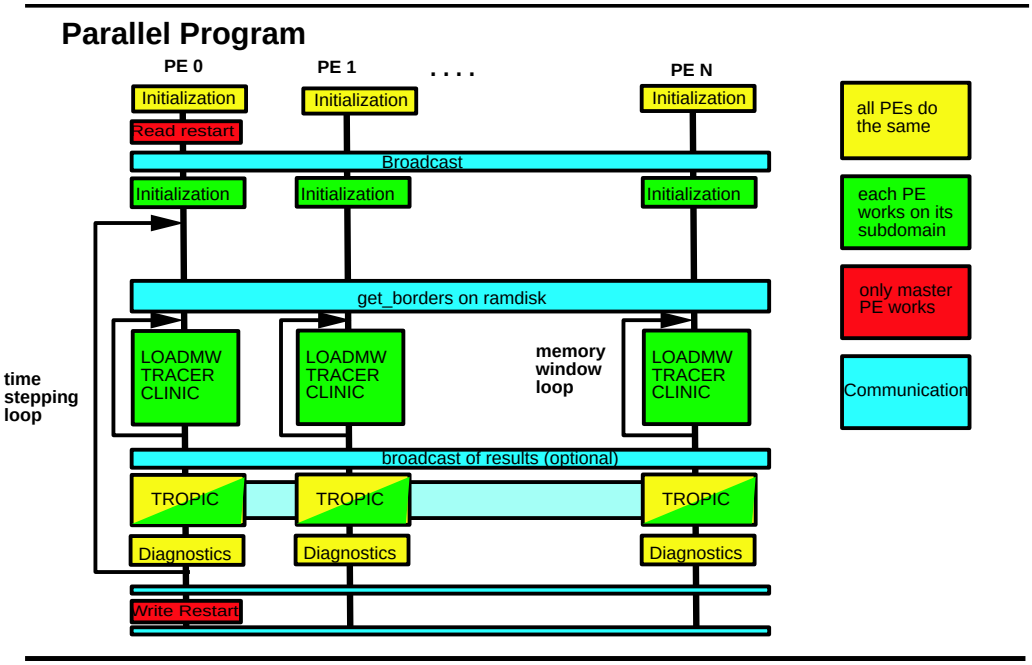

Figure 4.3: MOM2: parallelisation and distribution of workload.

parallelization. Reading and writing restart files have to be modified. And for coupled models, there is the interface between the submodels, as mentioned above.

Typical subroutines in the model consist of loops with local operations and thus these loops can stay unmodified. But in the parallel version some of the values are not just local values and have to be communicated. They were calculated in setup-parallel and handed over via an extra include file. It includes all information about parallelization like the ID of the processor, the neighboring processors and so on. The include-file, where the arrays are defined, has to be modified, too. The arrays now are divided into global arrays dimensioned to the original size of the ice model and local arrays, which can be dimensioned much smaller. At last, some communication routines have to be called.

The benefit of the parallelization will be shown with two examples. Let us consider 2 model configurations. First a high resolution Arctic model with a resolution of 1/4 degree. It includes $243 \times 170 \times 60$ grid points. One additional tracer is introduced. For mixing, the simplest scheme with constant coefficients is used. The time steps is 1 hour. To eliminate the singularity on the north pole a rotated grid is used. In this model the ice covers nearly the whole ocean. Thus both submodels uses the same domain decomposition.

The other case is a global model with much lower resolution of about 2 degrees. It consists of $194 \times 92 \times 29$ grid points. Here 3 passive tracers are included. The advection scheme is the earlier mentioned Flux corrected transport scheme and the time step is 6 hours. For global models the poles can not be eliminated with a simple rotating of the grid which would displace the problem only to another point of the model region. To remove the instabilities near the poles the highest wave numbers can be filtered out of the solution. Unfortunately with respect to the parallelization scheme, filtering is in general nonlocal – one needs information about the whole latitude.

At the Alfred Wegener Institute a Cray T3E-600 with 138 PEs was used for the calculations. This is only a small machine with respect to the number of workgroups working on it. So we are interested to improve efficiency also when using only a moderate number of processors for our applications. The performance data for the 2 models are shown in Figure 4.6. 10 time steps are

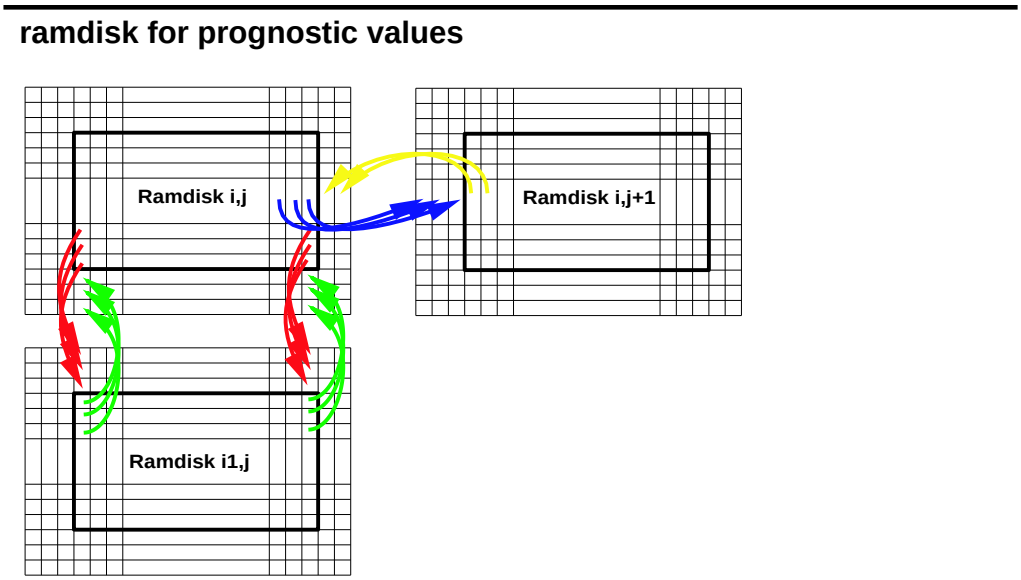

Figure 4.4: MOM2: exchange and boundary values.

calculated on 16 PEs. When we extrapolate the time for the first time steps to a long model run - the Arctic model needs about 2000 hours CPU time for 100 years, the global model only about 200 hours. The main part of the work is done in subroutine TRACER, followed by the dominating subroutine in the ice model DRIFT. The coupling needs only 1 % of the time. Therefore for 16 PEs the interface between the submodels can be performed via one PE. The performance per PE for subroutines where the main calculation are done (TRACER, CLINIC, TROPIC, DRIFT) is overall satisfactory.

For the global model the subroutine LOADMW which manages the memory window loading and shifting becomes a problem. It uses 7% of the time but calculates only some intermediate values. The solution is to open the memory window, so more rows can be calculated before one has to shift the memory window again.

The speedup for the Arctic model is limited by the daily forcing - each day the model reads new data from disk. The global model works with monthly means, thus less input is necessary. Here the ice model limits the scalability, because the ice region is much smaller than the ocean region. The global model needs 2 PEs at minimum, the Arctic model 6 PEs. Because of the higher number of grid points the Arctic model scales better compared with the global model.

The global version was used for the different experiments in OMIP with the coupled ocean-sea ice model. Furthermore, some preliminary work was also done for coupling with an atmospheric model. This can be done in 2 different ways. For small configurations the atmosphere is coupled internally, this means we have in one programme the calls of ocean, sea ice and atmosphere. But the memory requirements limits the number of grid points which can be considered in such a programme. Thus, a second way is to couple the programmes externally via flux couplers (e.g. the NCAR flux coupler OASIS). Then each submodel can be calculated on different machines and only the fluxes have to be exchanged between the models. This approach is fully suited for the close interaction between ocean, sea ice and atmosphere. This work was continued in the DFN Gigabit West Testbed project (Verteilte Berechnung von Klima- und Wettermodellen) and will be published in the Berichte zur Polar- und Meeresforschung of AWI (Frickenhaus and Hiller, 2000).

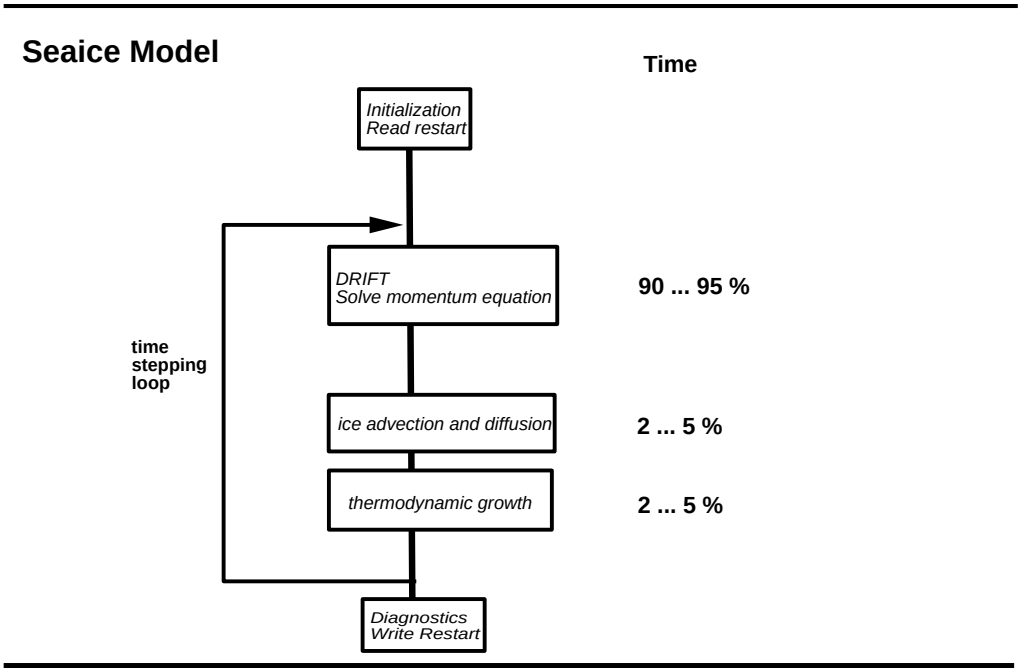

Figure 4.5: MOM2: flowchart and computing times for the sea ice model.

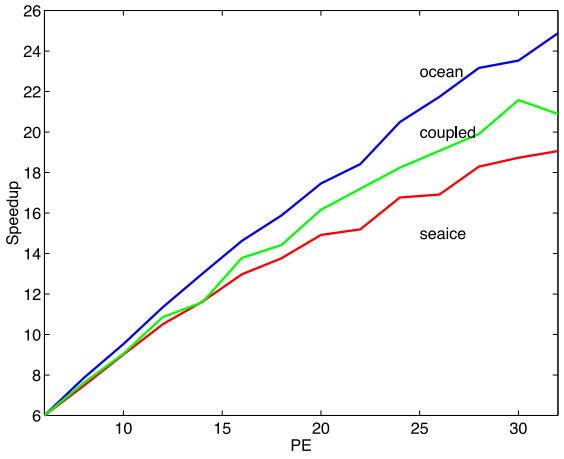

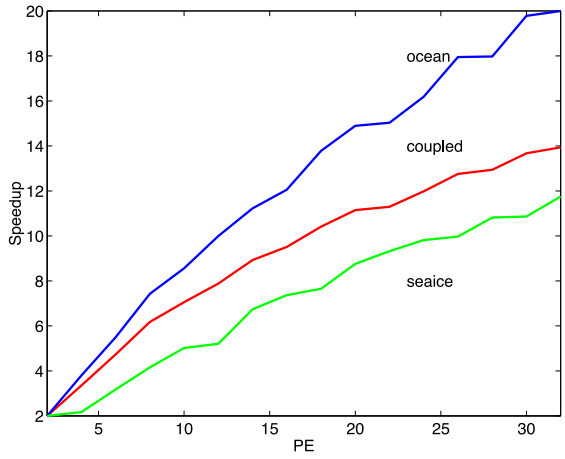

Figure 4.6: MOM2: scalability of the Arctic model (upper panel) and the global model (lower panel) configuration.

Chapter 5

The forcing

A climatological data set for forcing global ocean models has been established in this project. It has been derived from the data of the re-analysis project of the European Centre for Medium-Range Weather Forecasts (ECMWF). These data are called ECMWF ReAnalysis (ERA). A short description of these data is given in section 5.1. The motivation to produce such a data set arose from the international ocean model intercomparison project (OMIP). For this project a data set was necessary which is global, which can provide a resolution in time considering also weather time scales, and which has a resolution in space horizontally somewhat better than coarse ocean models have. The ERA seemed to be best appropriate for this purpose.

In OMIP, the focus lay on an intercomparison of the mean global oceanic circulation. This led to the consequence to produce a mean annual cycle from the 15 years of ERA with daily fluctuations superimposed. The parameters used will be described in section 5.2 and the mean annual cycle in section 5.3.

That the ocean models are global led to some more consequences. The precipitation and evaporation over the continents had to be considered and transformed into runoff. But, because the focus lay only on the mean circulation, a correct simulation of the annual cycle of the runoff peaking sometime in spring or summer was not imperative. Therefore, the runoff scheme developed for this purpose, is relatively simple. It can be and has been run independent of the ocean models so that the resulting output is available. The runoff model will be described in section 5.4.

Global ocean models should include sea ice models, e.g. the model of Hibler (1979) with full rheology. For such models the approach to relax ocean model temperatures to Levitus' climatology cannot be maintained. Therefore, an approach using the budget of heat flux is pursued, which depends on the ice conditions in the model, in particular on the distribution of the ice concentration.

Furthermore, for global ocean models whose mean circulation is compared, it is necessary that the budgets of both the heat and of the fresh water fluxes have to be closed. In order not to prefer one of the models the closure procedure has been independent of the model formulation. The closure procedure will be described in section 5.5.

To get an impression of the quality of the OMIP-Forcing data set it will be compared with other climatologies, which will be described in section 5.6. The preparation of an atlas of this new climatology will be described in a separate publication.

5.1 Data source

The ERA Project has produced a validated 15 year set of assimilated data for the period 1979 to 1993. In many areas of the globe the density of available observations is far below that needed to support the analysis with the required accuracy. In such areas a simple analysis would rely mainly on satellite based observations: cloud cleared radiance data or retrieved temperature and humidity data from the NOAA-Satellites, and cloud motion wind data from geostationary satellites.

A data assimilation scheme attempts to make use of a numerical forecast model to propagate information concerning the state of the global atmosphere from data rich areas to data sparse areas. Output from the forecast model is used, together with the observations and forcing fields, as input to the analysis. Results from the analysis, after initialization, are then used as initial conditions for the next forecast. These processes are repeated in a cyclic fashion.

Thus, continuous data assimilation over a long period is equivalent to running the forecast model as a global circulation model and relaxing towards the observations and forcing fields at six hourly intervals. In addition, two further cycles are included at twelve and twenty-four hourly forecast intervals. These cycles are coupled to the six-hourly cycle, because they are based on the same initializations.

All forecasts are made available through the MARS system. In the corresponding User Guide (MARS, 1995) all parameters are summarized and listed according to their codes. The surface parameters are on a Gaussian grid with T106 truncation, which corresponds to a resolution of $1.125° \times 1.125°$.

5.2 The parameters

As a first approach all three forecast cycles have been averaged to daily values: four six-hourly forecasts, two twelve-hourly forecasts and two twenty-four-hourly forecasts per day. For this averaging procedure the forecasts have been chosen in such that for all eight forecast the endpoints of the intervals lay within 24 hours.

In the following, we present the parameters which have been used. Some of them had to be combined to new ones. The total precipitation has been calculated by summing large scale precipitation, MARS-code 142, and convective precipitation, MARS-code 143. Runoff has been calculated by the runoff scheme described in section 4 using total precipitation minus evaporation, MARS-code 182.

The scalar wind and its daily standard deviation have been calculated from the wind components, MARS-codes 165 and 166. For the first approach, using all three forecast cycles, a total of eight forecasts are available to calculate the daily standard deviation. These parameters together with the mean sea level pressure are needed as input for the bulk formulae mentioned in section 5.

The sea ice models of the ocean models produce their own albedos in dependence of the current ice conditions. Therefore, they have to be forced by the total solar radiation, in which the reflected part of the solar radiation is still included. For this purpose, forecast albedos of ERA have been used. Total solar radiation R_{tot} has been calculated from net solar radiation R_{net}, MARS-code 176, and forecast albedo a, MARS-code 243, according to $R_{tot} = R_{net}/(1 - a)$.

The direct outputs of ERA for the long wave radiation, MARS-code 177, and the turbulent heat fluxes, MARS-codes 146 and 147, are used for the heat budget closure considerations and are plotted in the atlas over the continents.

Some of the parameters have been accumulated since the start of the forecast. Therefore, the forecasts of these parameters had to be divided by the corresponding number of seconds, 21600 for six-hourly forecast intervals, 43200 for twelve-hourly forecast intervals and 86400 for twenty-four-hourly forecast intervals before the averaging procedure.

The 2 m temperatures and 2 m dewpoint temperatures have undergone a correction after Harder et al. (1998). In the summer period from June 15 to August 15, air temperatures are not allowed to fall below 0°C. Dew point temperatures are adjusted accordingly so that the relative humidity of the air is conserved. This correction has been done for the mean annual cycle.

5.3 The mean annual cycle

The daily values are the basis for the mean annual cycle. All daily values of all 15 years were filtered by a Gaussian filter method. This method divides the data into a low pass and a high

New Code	Parameter	MARS-Codes
139	Sea surface temperature	139
142	Total precipitation	142*, 143*
146	Surface sensible heat flux	146*
147	Surface latent heat flux	147*
151	Mean sea level pressure	151
160	Runoff	142*, 143*, 182*
164	Total cloud cover	164
165	Scalar wind	165, 166
166	Standard deviation scalar wind	165, 166
167	2m temperature	167
168	2m dewpoint temperature	168
176	Total solar radiation	176*, 243
177	Surface thermal radiation	177*
180	East west surface stress	180*
181	North south surface stress	181*
182	Evaporation	182*

Table 5.1: List of parameters. A * denotes: Parameter has been accumulated since start of forecast.

pass. The low pass has been averaged to one year. From the high pass a particular year has been selected such that the variability is preserved as well as possible. This selected year has been added to the averaged low pass. The sum is called mean year in the following.

The Gaussian filter method resembles the method of the running mean. This method is a very simple filter and the corresponding characteristic filter function shows undesirable oscillations. They can be avoided by using a Gaussian filter (Schönwiese, 1992) whose characteristic function is exponentially decaying instead of oscillating. In the running mean method the weights are constant, whereas in the Gaussian filter method weights are applied which decrease symmetrically.

Consider a time series, $a_i, i = 1, \ldots n$, with n being the length of the time series. The filtered time series, $\tilde{a}_j, j = 1, \ldots n - 2m$, m being the filter width, is calculated by multiplication with the weights $w_k, k = -m, \ldots + m$ according to

$$\tilde{a}_j = \sum_{k=-m}^{+m} w_k a_{j+m+k} \quad \text{for } j = 1, \ldots n - 2m \tag{5.1}$$

Symmetrical filtering uses weights, then no phase displacements occur. Filter weights are be normalized to unity and then averages in the time intervals $(i - m, \ldots, i + m)$ are preserved.

In order to obtain weights implying an exponential characteristic filter function R, following algorithm has to be applied. If T_* is the period, for which $R(T < T_*) = 0$ is valid, then $T_* = 6\sigma$ with σ being the standard deviation of the normal distribution produces the not normalized weights

$$w_k = \frac{1}{\sqrt{2\pi}} e^{-\frac{1}{2}\left(k\frac{6}{T_*}\right)^2}, \quad k = 0, \ldots m \quad \text{and} \quad T_* = 2m + 1 \tag{5.2}$$

The characteristic filter function for the low pass yields

$$R_L(f) = e^{-\frac{1}{3}\pi^2 f^2} \tag{5.3}$$

Normally it is sufficient to break off the series w_k if $w_k < w_0/10$. When the low pass $\tilde{a}_j(L)$ is determined in this way, the high pass $\tilde{a}_j(H)$ is calculated by

$$\tilde{a}_j(H) = a_j - \tilde{a}_j(L) \qquad j = 1, 2, \ldots, n - 2m \tag{5.4}$$

and the characteristic filter function of the high pass becomes

$$R_H(f) = 1 - R_L(f) \tag{5.5}$$

The filter has been applied with $m = 15$ so that the averaging interval $(-m, \ldots, +m)$ has a total length of one month. Then, the daily values of the low pass have been averaged over all 15 years to obtain one year.

From the high pass a particular year was selected in the following way. At first, the search for this year was restricted to only one parameter, to the zonal wind stress, which is one of the most important parameters to force ocean circulation models. Then, a total of 15 mean years from this parameter have been calculated by adding every year of the 15 years of the high pass to the averaged low pass. From these 15 mean years and the 15 original years variances relative to monthly means have been calculated (Table 5.2), which are roughly equal to the squared high pass. The variances of the 15 mean years are approximately 75% of those of the 15 original years. In order to preserve the variability of the original data as well as possible, the specific year has to be chosen that provides a maximum of variance.

Both, the mean years and the original years have a maximum of their variances in the fourth year. This corresponds to 1982, a year when a strong El Nino event occurred. Therefore, the fourth year has been chosen to be the year of the high pass which has to be added to the averaged low pass. This year has also been chosen for the remaining parameters for reasons of dynamical consistency.

The original years of ERA follow the real calendar. Therefore, the months are different in length: there are either 28 or 29 days for February, implying a total of 365 or 366 days. The ocean models use idealized years, i.e. 12 months with 30 days, respectively, a total of 360 days, which is shorter than the real calendar. Therefore, the mean year has to be shortened by cutting the last 5 days of December. This procedure is combined with the procedure of producing a cycle, i.e. adjusting the first and the last days of the shortened mean year. The resulting mean year is called the mean annual cycle. This cycle has smooth transitions at the begin and the end of the year. Summarizing, one can also state that the cycle has smooth transitions at the begin and the end of every month. The time-related topology is preserved, and the variability of the original data is preserved at 75%.

5.4 The runoff model

The basis of the runoff model are two data sets provided by Hagemann and Dümenil (1998): the catchment areas of the 35 largest rivers of the world (the Baltic Sea is treated as a river) and the main drainage basins of the world, which correspond to the water sheds.

These data sets are horizonal distributions of different numbers defining the regions of the catchment areas and the drainage basins. To avoid an overlapping in these reference numbers, an offset has been introduced for the last data set. This one considers the whole area of the continents

No.	Year	Mean Year	Single Year
1	1979	0.78	1.06
2	1980	0.75	0.98
3	1981	0.74	0.99
4	1982	0.80	1.05
5	1983	0.78	1.03
6	1984	0.76	1.02
7	1985	0.77	1.02
8	1986	0.76	1.03
9	1987	0.78	1.04
10	1988	0.77	1.00
11	1989	0.75	1.00
12	1990	0.79	1.05
13	1991	0.76	1.01
14	1992	0.75	0.99
15	1993	0.78	1.03

Table 5.2: List of globally averaged variances relative to monthly means for the 15 years of daily averaged ECMWF Re-analysis data. Unit: $10^{-2}(\mathrm{Nm}^{-2})^2$.

whereas the first one covers only parts of it. Both data sets were combined in such a way that the reference numbers in the first one were in general preferred and those in the last one were used only to cover the areas not considered in the first one. The resulting data set is shown in Figure 5.1.

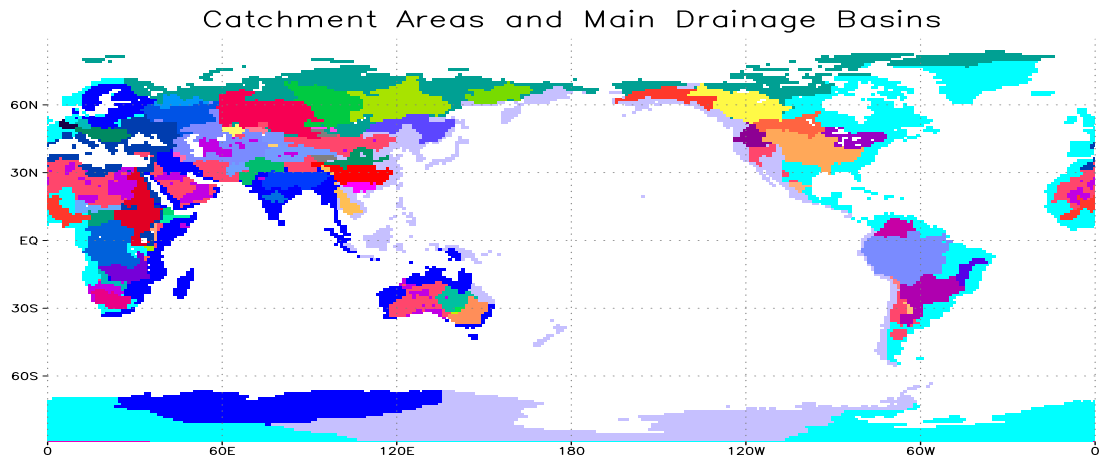

Figure 5.1: Catchment areas and main drainage basin of the runoff model

From this data set a quasi coast line is derived along the edges of the continents, which correspond essentially to the coast line but lies in the 'water' of the ocean models. The catchment area reference numbers a adjusted to this quasi coast line corresponding to the mouth coordinates in the T106 grid. From regions where no catchment areas exist but drainage basins exist whole lines of reference numbers are derived and attached to the quasi coast line. The reference numbers of those drainage points have been chosen which are the nearest to the points of the quasi coast line.

The distance between two points has been measured by the Manhattan distance: given two two-dimensional vectors $\boldsymbol{r} = (x, y)^T$ and $\boldsymbol{r}' = (x', y')^T$ with $x, x' = 1, \ldots n$ and $y, y' = 1, \ldots m$ and n and m being the dimensions of the T106 grid. Then, the Manhattan distance is defined by:

$$|\boldsymbol{r} - \boldsymbol{r}'| = |x - x'| + |y - y'| \tag{5.6}$$

In the next step, the coordinates of the quasi coast line have been assigned to the land points. Assigned were the coordinates either of the mouths if the land points were in the catchment areas, or of the nearest quasi coast line points, if the land points were in the drainage-only defined regions. In the last case up to seven nearest quasi coast points with the same Manhattan-distance were possible. This yielded seven horizontal fields of coordinates for each of the two coordinate directions.

In the following step, these fields were used to gather the difference of the mean annual cycles of precipitation and evaporation at the land points and to put it instantaneously, i.e. directly for every day, to the quasi coast line, whereby up to seven coordinates per land point were considered. Because the continental runoff is non-negative by definition but could become negative during this procedure, negative runoffs were set to zero and positive ones reduced correspondingly.

Furthermore, closed basins with no runoff had to be considered, where the water is circulating only within the basin and does not reach the oceans. Such a basin is for example the Caspian basin including the Caspian Sea and the catchment area of the Volga being the main fresh water provider for this inland sea. To judge the quality of the model, the model estimate for the 35 main rivers is compared with the observations of annual runoff for these rivers (Dümenil et al. 1993) as shown in Table 5.3.

River	Observations	Model Estimates
Amazonas	154943	141505
Congo	40269	85215
Ganges/Brahmaputra	33485	22230
Orinoco	31171	39110
Yangtze	29043	17619
Jenissei	17691	9484
Lena	16640	8449
Parana	16566	35704
Baltic	15323	9915
Mississippi	14779	22032
Ob	12559	10119
Amur	9791	7137
Mekong	9485	17576
Mackenzie	9153	7539
Wolga	8105	6453
St.Lawrence	7657	8684
Xun	6998	7415
Donau	6435	4823
...		

[list of rivers] Table 5.3: List of annual runoffs of the 35 main rivers. Unit: $m^3 s^{-1}$. Continued below.

It can clearly be seen that there are systematic errors. The runoffs of the Sibirian rivers are underestimated and those of the African rivers are overestimated. Assuming, that there are no systematic errors in this very simple runoff model, this would mean, that in Africa evaporation is

River	Observations	Model Estimates
...		
Yukon	6371	5634
Columbia	5446	6906
Sambesi	3342	15589
Dvina	3335	2462
Kolyma	3244	2878
Godavari	3061	1653
Nil	2935	21589
Sao Francisco	2807	15086
Nelson	2405	4157
Rhein	2287	1250
Indus	2262	6724
Huang	1444	2647
Chari	1062	13909
Niger	1055	19766
Elbe	782	978
Murray	258	2319
Oranje	145	1865

Table 5.3: Continued: list of annual runoffs of the 35 main rivers. Unit: m^3s^{-1}.

underestimated. This can be explained by the observing system. Evaporation during the irrigation of the fields is not recorded.

For a good simulation of the sea ice in the Arctic by the ocean circulation models, a realistic simulation of the Sibirian river runoff and of the glacial runoff is necessary. Therefore, the observations of annual runoffs (Dümenil et al. 1993) have been prescribed for every day and the difference between them and the model estimate plus the runoff of the closed basins are put into the Arctic if positive and into the 'Non-Arctic' if negative. This procedure has been applied for every day so that the budget is closed every day.

5.5 Closure procedure

The heat flux budget consists of one incoming component, the short wave solar radiation and three outgoing components, the long wave radiation and the two turbulent heat fluxes, the latent and the sensible heat flux. The fresh water flux budget consists of two incoming components, the precipitation and the continental runoff, which has been calculated from precipitation and evaporation over the continents, and one outgoing component, the evaporation. Instead of using evaporation from ERA over the oceans, it is calculated from the latent heat flux in dependence on the ice conditions. Because there is no ice concentration (equivalent names: ice compactness or ice coverage) available in ERA ice conditions are simulated by comparing sea surface temperature with the freezing point. By this way ice concentrations of 0% and 100% can be distinguished. In the first case the heat of vaporization is used and in the last case the heat of sublimation.

The budgets of heat and the fresh water must be closed in order to preserve mass and to avoid a long-term heating or cooling of the ocean model. The budgets are closed when zero imbalances arise, defined by the net heat and net fresh water fluxes integrated over the oceans and over the whole year. Because these fluxes are calculated from several input parameters, their budgets cannot be closed directly by simply subtracting their mean, but only indirectly by adapting the formulae for these fluxes. Therefore, an adaptation procedure with pre-defined finite precision is necessary. The budgets are considered as closed when the following conditions are fulfilled

$$\int_{ocean}\int_{year} (Q_{sw} - Q_{lw} - Q_{la} - Q_{se})\, d\lambda d\phi dt \overset{!}{<} \varepsilon_h \tag{5.7}$$

$$\int_{ocean}\int_{year} (P + R - c\, Q_{la})\, d\lambda d\phi dt \overset{!}{<} \varepsilon_f \tag{5.8}$$

with

Q_{sw}	:	short wave solar radiation
Q_{lw}	:	long wave radiation
Q_{la}	:	latent heat flux
Q_{se}	:	sensible heat flux
P	:	precipitation
R	:	continental runoff
c	:	heat of vaporization or sublimation, dependent on ice conditions.

The bounding coefficients are chosen as $\varepsilon_h = 0.1 W m^{-2}$ and $\varepsilon_f = 0.1$ mm/month, respectively. The adaptation proceeds as follows. Because the evaporation is calculated from the latent heat flux, its formula is adapted first. The latent heat flux is calculated by using the drag coefficients after Large and Pond (1982), which have been used by Oberhuber (1988) for his atlas. In contrast, the specific humidity of the air is not calculated using 2 m air temperature and relative humidity, but using only 2 m dew point temperature. But following Oberhuber's work, the Charnock constant is modified until (5.8) is satisfied.

Afterwards, to close the heat budget, the formula for the long wave radiation is adapted. The net effect of long wave radiation is taken from Berliand (1952) as Oberhuber (1988) proposed. Budyko (1974) proposed the cloudiness factor c' in this formula to vary linearly with latitude ϕ. His table has been transformed into a linear equation, which is symmetric to the equator:

$$c' = 0.5 + 0.4 \frac{\phi}{90^\circ} \tag{5.9}$$

Deviating from Oberhuber (1988) we do not use the formula of Magnus for the water vapor pressure (Möller, 1973) but the formulae of Buck (1981), which are dependent on the ice conditions. The formula for the long wave radiation is multiplied with a factor which adjusted in order to fulfill (5.7).

The outgoing components of the heat flux budget are dependent on the sea surface temperature. When the ocean models are running these components are calculated from the sea surface temperatures of the models. That means that one of the models should have been involved in the adaptation procedure. But in order to maintain the equality in the treatment they have been totally excluded from the closure procedure. The sea surface temperatures of ERA have been used instead.

When the closure procedure was started both budgets had positive imbalances. That means for the heat flux budget, that in principle the incoming component, the solar radiation, had to be decreased and the outgoing components had to be increased. An increasing of the turbulent heat fluxes helped also the fresh water flux budget to get closed. But a further increasing was only possible by increasing also the precipitation. But neither solar radiation could be decreased nor precipitation could be increased without using outside data.

But a chance to change them under this restriction arose from the heat und fresh water flux budgets of the direct outputs of ERA. Instead of following the first approach of averaging all three forecast cycles, every cycle was regarded separately. That means from each forecast cycle a mean

Parameter	6-hourly fc	12-hourly fc	24-hourly fc
Precipitation	87	91	95
Net fresh water flux	-13	-10	-8
Net fresh water flux global	-4	-1	1
Solar radiation	165	163	161
Net downward heat flux	8	4	< 1

Table 5.4: Oceanic means of heat and fresh water fluxes from mean annual cycles for each forecast cycle (fc) of ERA. First three rows in mm/month. Last two rows in Wm^{-2}.

annual cycle has been produced as described in section 5.3. Oceanic means of the heat and fresh water fluxes are listed in Table 5.4.
Table 5.4 shows the following trends in dependence of the forecast cycle. Precipitation increases and solar radiation decreases with increasing forecast interval. In addition, the imbalances of the oceanic heat flux budget and the global fresh water flux budget diminish, so that they are closed for the cycle with the longest forecast interval if the level of precision is somewhat lowered compared with ε_h in (5.7) and ε_f in (5.8).

Both, the trends in precipitation and solar radiation and the closed budgets indicate that the chance to get the budgets closed with acceptable fluxes is higher when not an average of all three cycles is used, but only the 24-hourly forecast interval cycle. For this cycle only two forecasts per day are available. The ratio of the daily standard deviation of the scalar wind to its daily mean based on these two values is 18%.

Starting the closure procedure on basis of this cycle, the second condition in (5.8) is satisfied with a Charnock constant 0.0187. This value lies in the range of values which can be found in the literature: from 0.010 to 0.035 (Fairall et al. , 1996). The first condition in (5.7) is fulfilled when the long wave radiation is multiplied by a factor of 1.045.

5.6 Other climatologies

The quality of the OMIP-Forcing was judged by comparison with other climatologies. The following data sets have been used for this purpose: the Comprehensive Ocean Atmosphere Data Set COADS in three different versions, Oberhuber (1988), da Silva et al. (1994) and SOC (1997), the direct outputs of ERA (1997), the data of the ReAnalysis project of the National Center for Environmental Prediction (NCEP) and National Center for Atmosperic Research (NCAR), and the data of the atmospheric circulation model ECHAM4 of the MPI (Legutke and Maier-Reimer 1999, Roeckner et al. 1996). In table Table 5.5 the time period covered by these data sets and the resolution in time are listed.

The main differences of these data sets are the resolution in time and the use of circulation models. The COADSs have been calculated without the help of any models, but they have only a monthly resolution. The other data sets have been calculated on the basis of such models, but are much finer resolved in time. Another difference refers to the horizontal distribution of the data sets. All the model based data sets are global whereas the COADS of Oberhuber (1988) and SOC (1997) do not cover the whole globe.

The forcing data, the atlas and their description are available over the following web-address: http://www.mpimet.mpg.de/Depts/Klima/natcli/omip.html. The following pictures compare the annual mean of heat and freshwater fluxes of the various analyses.

Climatology	Time period covered	Resolution in time
ECHAM4	15 years	daily
COADS Oberhuber (1988)	1950-1979	monthly
COADS da Silva (1994)	1945-1989	monthly
COADS SOC (1997)	1980-1993	monthly
NCEP ReAnalysis	1958-1997	six-hourly*
ECMWF ReAnalysis	1979-1993	six-hourly*
OMIP-Forcing	mean annual cycle	daily

Table 5.5: List of climatologies. A * denotes: minimum resolution. ECHAM4: output prepared to force an ocean model. NCEP: a monthly long-term mean has been copied over the web-page.

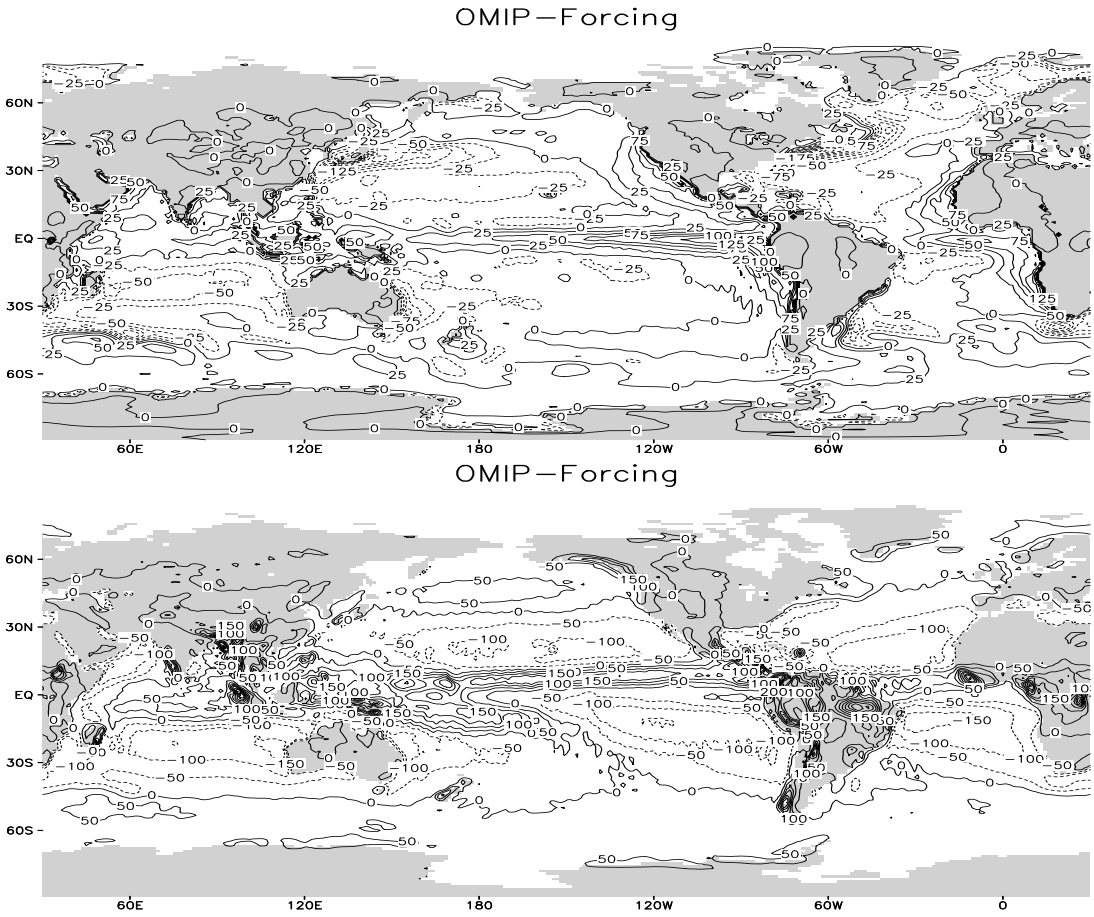

Figure 5.2: The heat and freshwater fluxes of the OMIP forcing, annual mean. Units: Wm^{-2}, mm/month.

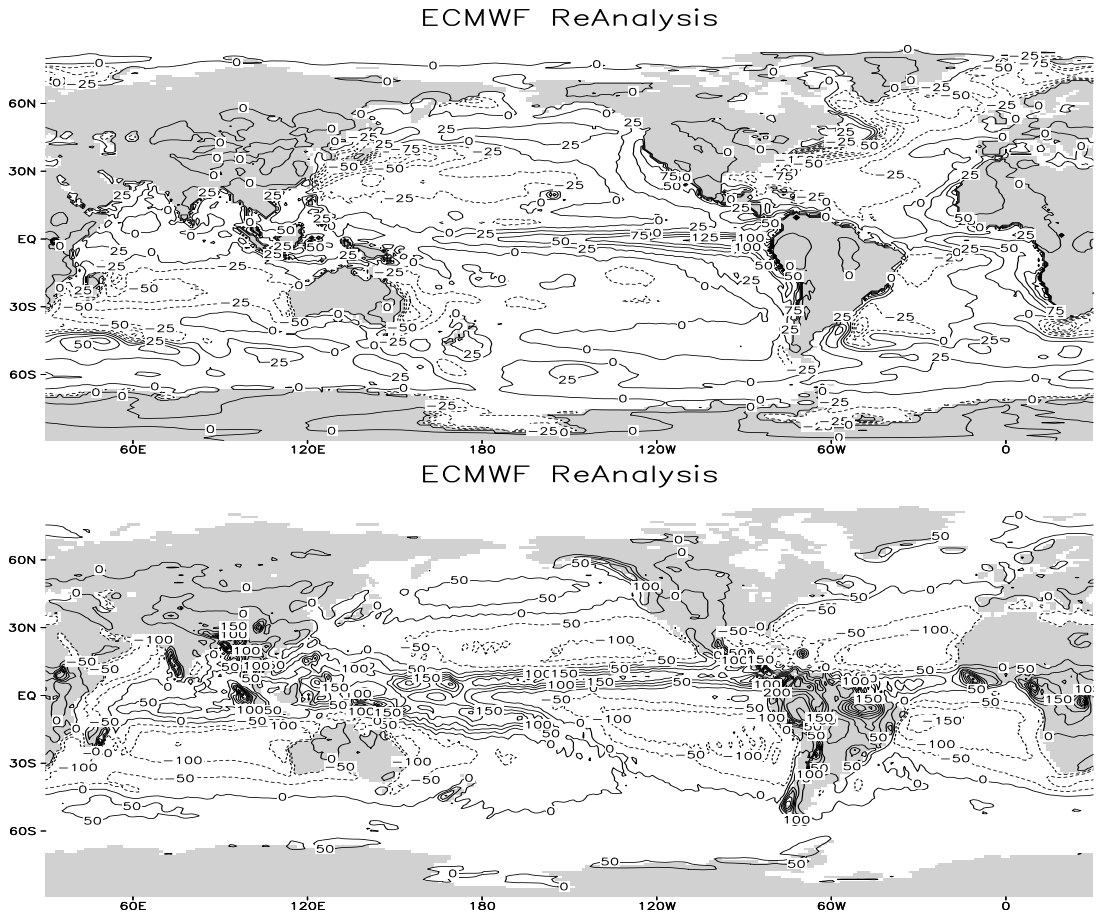

Figure 5.3: The heat and freshwater fluxes of the ECMWF reanalyse, annual mean. Units: Wm^{-2}, mm/month.

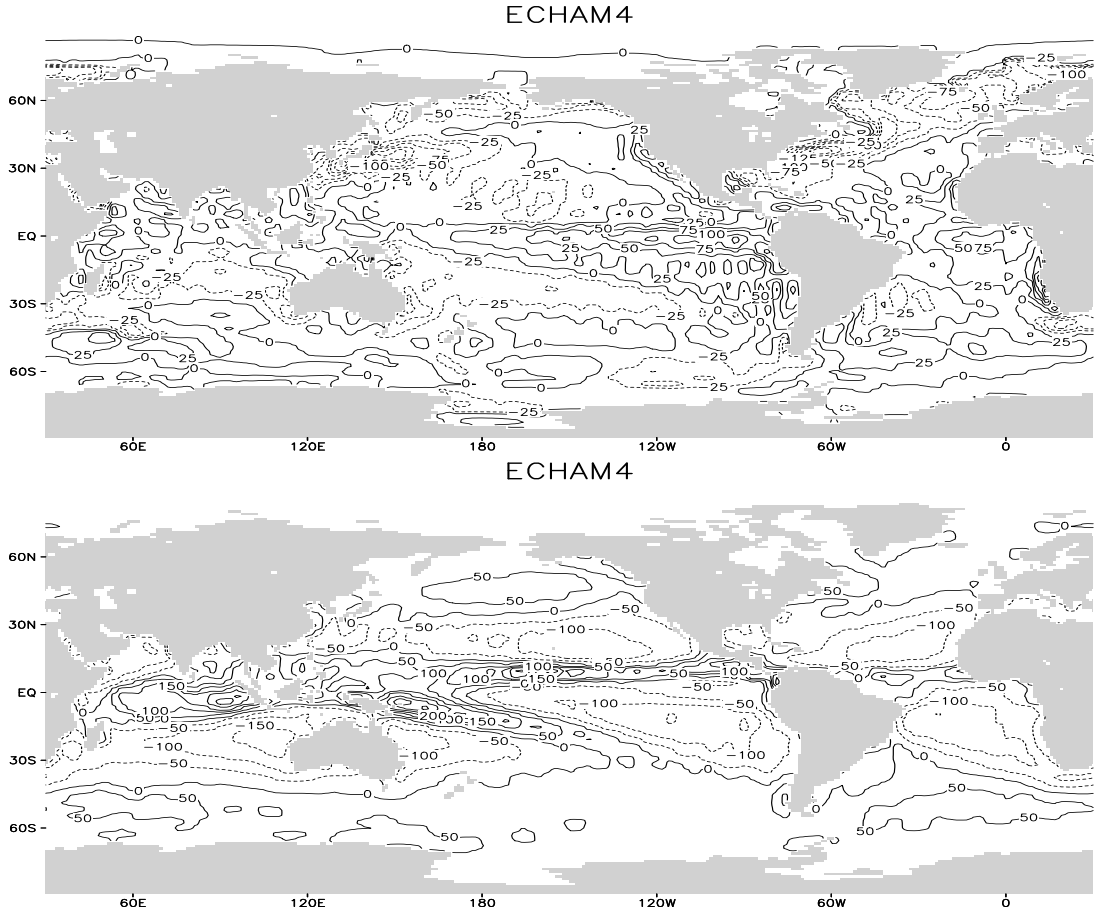

Figure 5.4: The heat and freshwater fluxes of the ECHAM4 model, annual mean. Units: Wm^{-2}, mm/month.

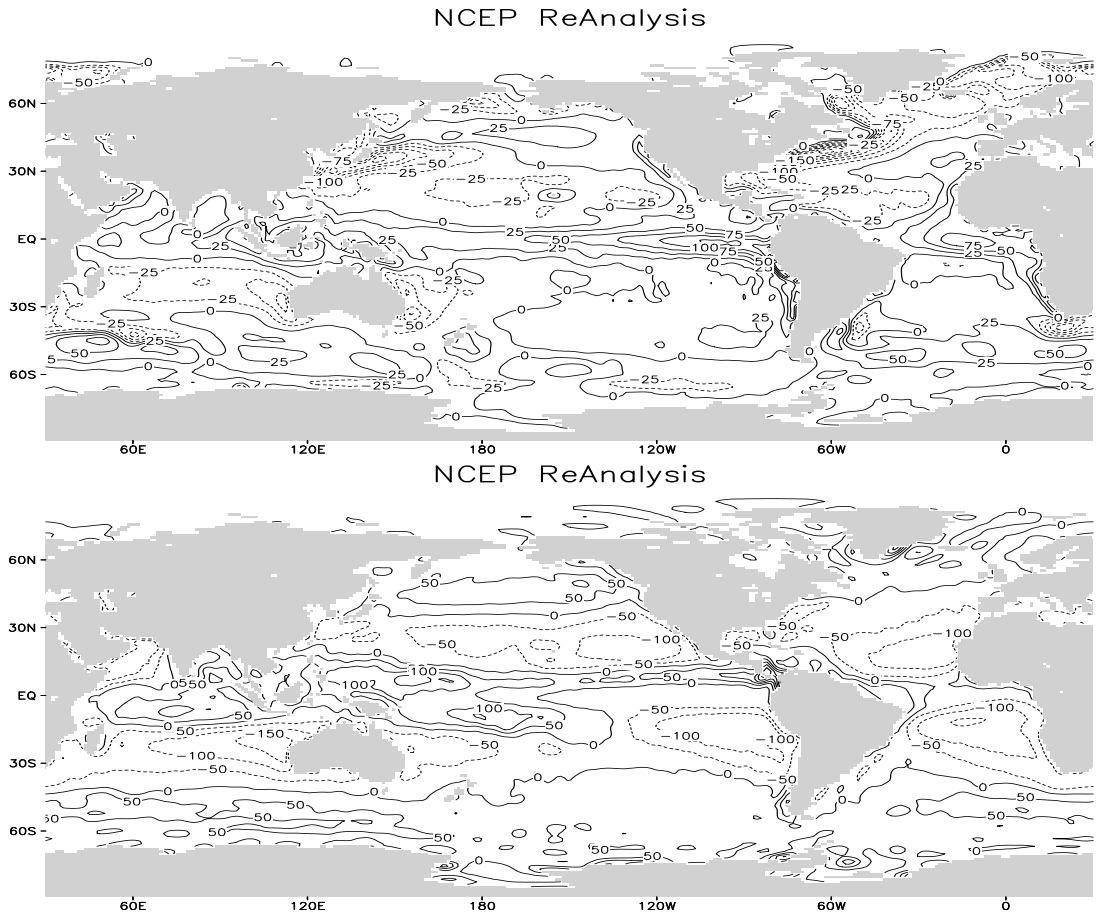

Figure 5.5: The heat and freshwater fluxes of the NCEP ReAnanlysis, annual mean. Units: Wm^{-2}, mm/month.

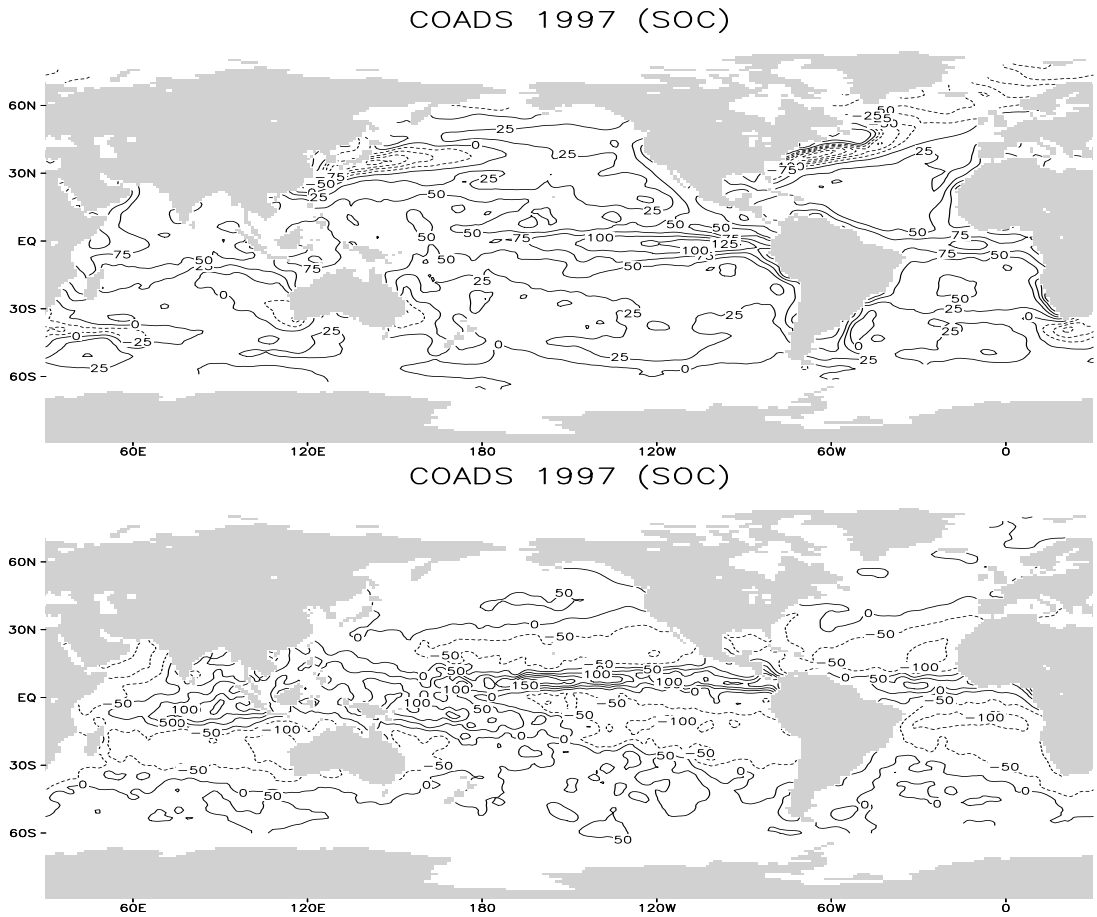

Figure 5.6: The heat and freshwater fluxes of the COADS SOC analysis, annual mean. Units: Wm^{-2}, mm/month.

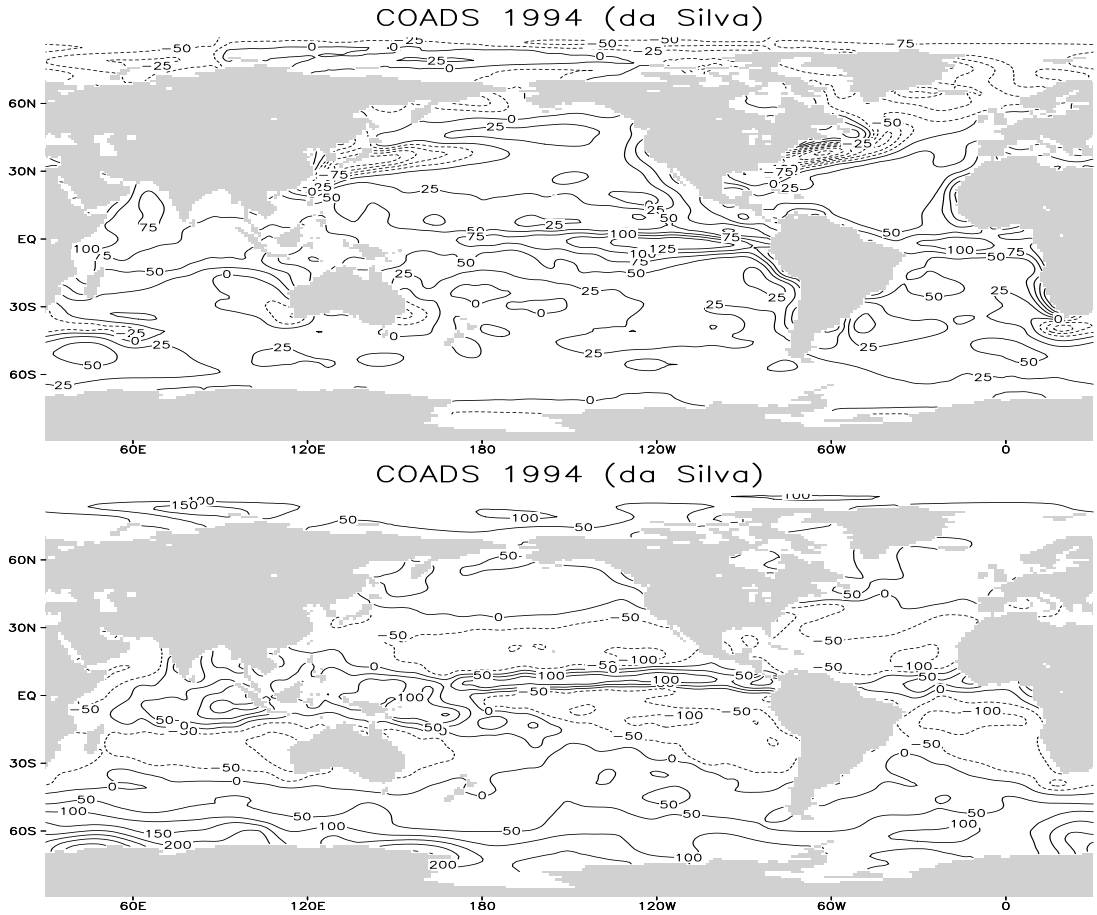

Figure 5.7: The heat and freshwater fluxes of the COADS da Silva analysis, annual mean. Units: Wm^{-2}, mm/month.

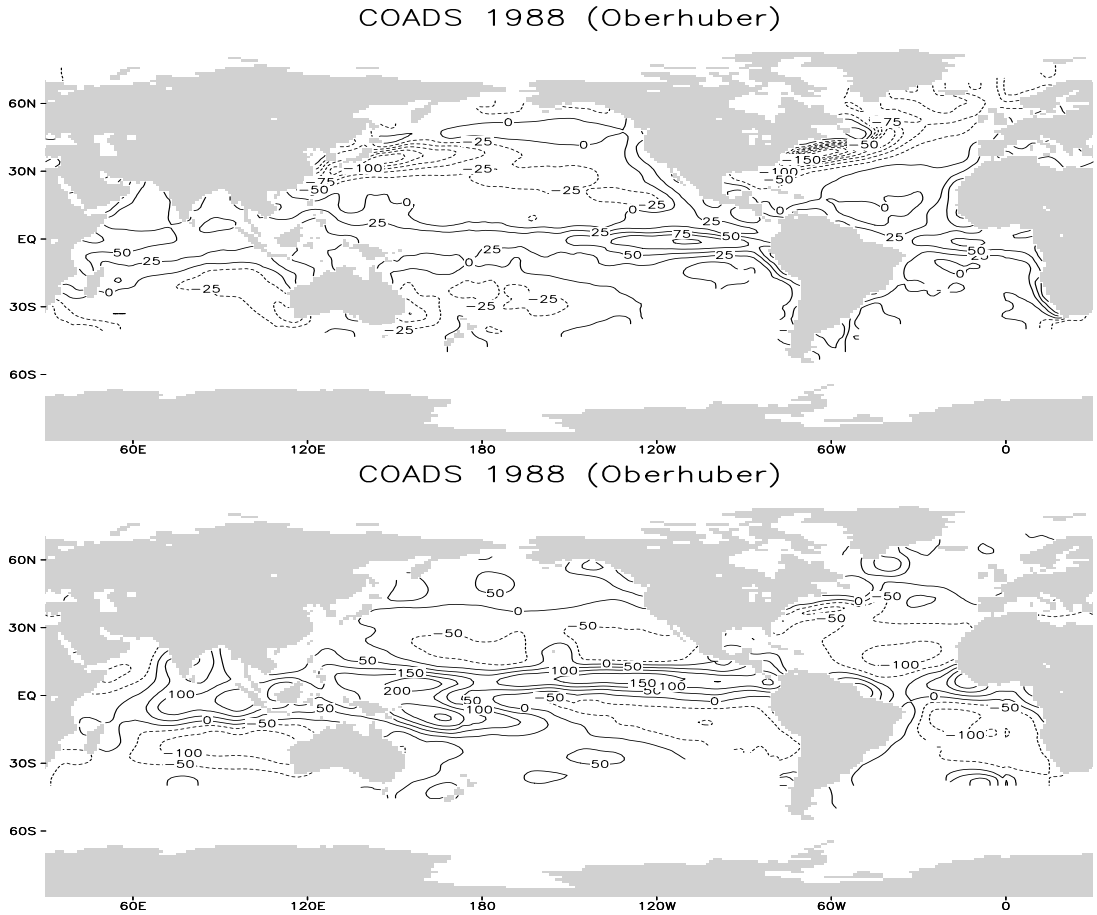

Figure 5.8: The heat and freshwater fluxes of the COADS Oberhuber analysis, annual mean. Units: Wm^{-2}, mm/month.

In order to compare the OMIP-Forcing with the other climatologies the implied meridional transports and zonal means are shown. Let $F(\lambda, \phi)$ be the heat or fresh water flux. Then the meridional heat or fresh water transport $T(\phi)$ is calculated as

$$T(\phi) = \int_{NorthPole}^{\phi} d\phi' \int_{\lambda_{west}}^{\lambda_{east}} F(\lambda, \phi') d\lambda \tag{5.10}$$

λ_{west} and λ_{east} are determined by the basin chosen for integration: Atlantic, Pacific, Indian Ocean and the global case.

At first, the meridional heat transports are shown for all three basins and the global case (Figure 5.9). Observations are overlaid by using error bars from various authors (Macdonald and Wunsch 1996, Johns et al. 1997, Rintoul 1991, Saunders and King 1995, Rintoul and Wunsch 1991, Bryden et al. 1991, Wijffels 1995) In the global case only the OMIP-Forcing has almost zero meridional transport south of 70° indicating that the heat budget is closed. The transports of the COADS SOC and COADS da Silva climatologies are strongly negative south of 30°N indicating a high imbalance in the heat budget.

In the global and the Atlantic cases the transports of the OMIP-Forcing are in the Northern hemisphere at the lower bound of the climatologies and in the Southern hemisphere at their upper

bound. In the global case the difference between the OMIP-Forcing and the direct outputs of the ERA is larger in the Southern hemisphere than in the Northern one. Such a large difference can also be found in the Pacific case. In the Atlantic the transports are smaller than observed, but in the Pacific they fit rather well. In the Indian Ocean all COADS climatologies fit better to the observations than the model based data sets, i.e. the re-analysis data and output of ECHAM4.

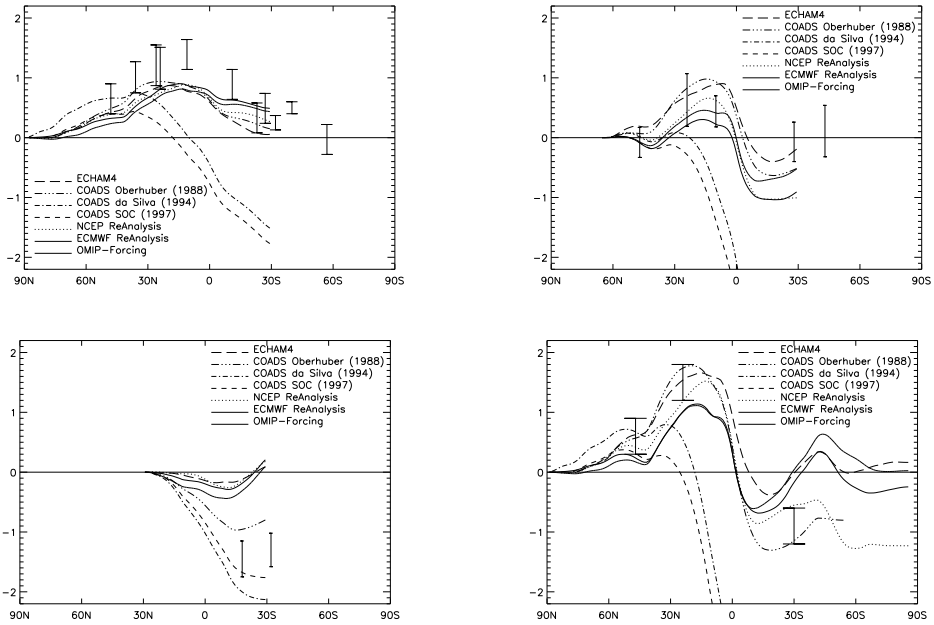

Figure 5.9:
The meridional heat transport, implied by the OMIP-Forcing and other climatologies, for the Atlantic, Pacific and Indian Ocean, and the global case (lower left panel). Units PW.

The global meridional fresh water transports are shown for two cases: with and without continental runoff (Figure 5.10). The case without runoff has been chosen to demonstrate that the OMIP-Forcing lies rather in the range of the other climatologies, except in the Southern Ocean where it has the highest values. The case with runoff can only be compared with the ECHAM4 model output, where also runoff is considered. Both climatologies are closed indicated by almost zero fresh water flux south of 70°S as in the heat flux case. The OMIP-Forcing is in good agreement with the ECHAM4 climatology in the Northern but not in the Southern hemisphere.

Furthermore, zonal means are shown for the net heat and fresh water fluxes, and for three other quantities (Figure 5.11), but again for the global case only. For the net heat flux the OMIP-Forcing lies in the range of the other climatologies. The COADS SOC and COADS da Silva data sets provide higher values in the tropics and subtropics. In the Arctic region the spread of the data sets is increasing with latitude. The absolute values of the net fresh water flux of the OMIP-Forcing are almost the biggest ones as well in the tropics where precipitation dominates, as in the subtropics where evaporation dominates.

There are three other quantities which have been considered: the turbulent kinetic energy input, the buoyancy and the coupling coefficient $\partial Q/\partial T$ of the Newtonian cooling following the algorithms of Oberhuber (1988). Regarding these quantities the OMIP-Forcing is compared only with his COADS atlas.

Buoyancy fluxes are fluxes of potential energy. They reflect changes of density due to heat and fresh water fluxes. The buoyancy fluxes resemble each other, but the minimum at the equator is more pronounced in the OMIP-Forcing case. The mean friction velocity is used as an estimate of

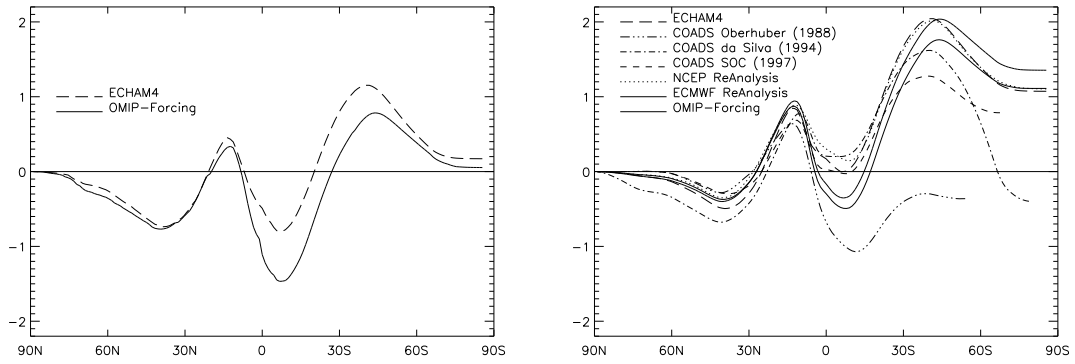

Figure 5.10:
The meridional freshwater transport, implied by the OMIP-Forcing and other climatologies. Left: with runoff. Right: without runoff. Units: Sv.

the turbulent kinetic energy input into the mixed layer. This quantity shows a similar feature as the implicit heat transport. In the Northern hemisphere the turbulent energy for the OMIP-Forcing is lower than that for the COADS climatology and in the Southern hemisphere it is reversed. The Newtonian cooling is an attempt to simplify the heat flux scheme, which is used more and more in ocean circulation models. The OMIP-forcing provides larger coupling coefficients than the COADS atlas of Oberhuber in the tropics and subtropics but lower ones in the Northern higher latitudes.

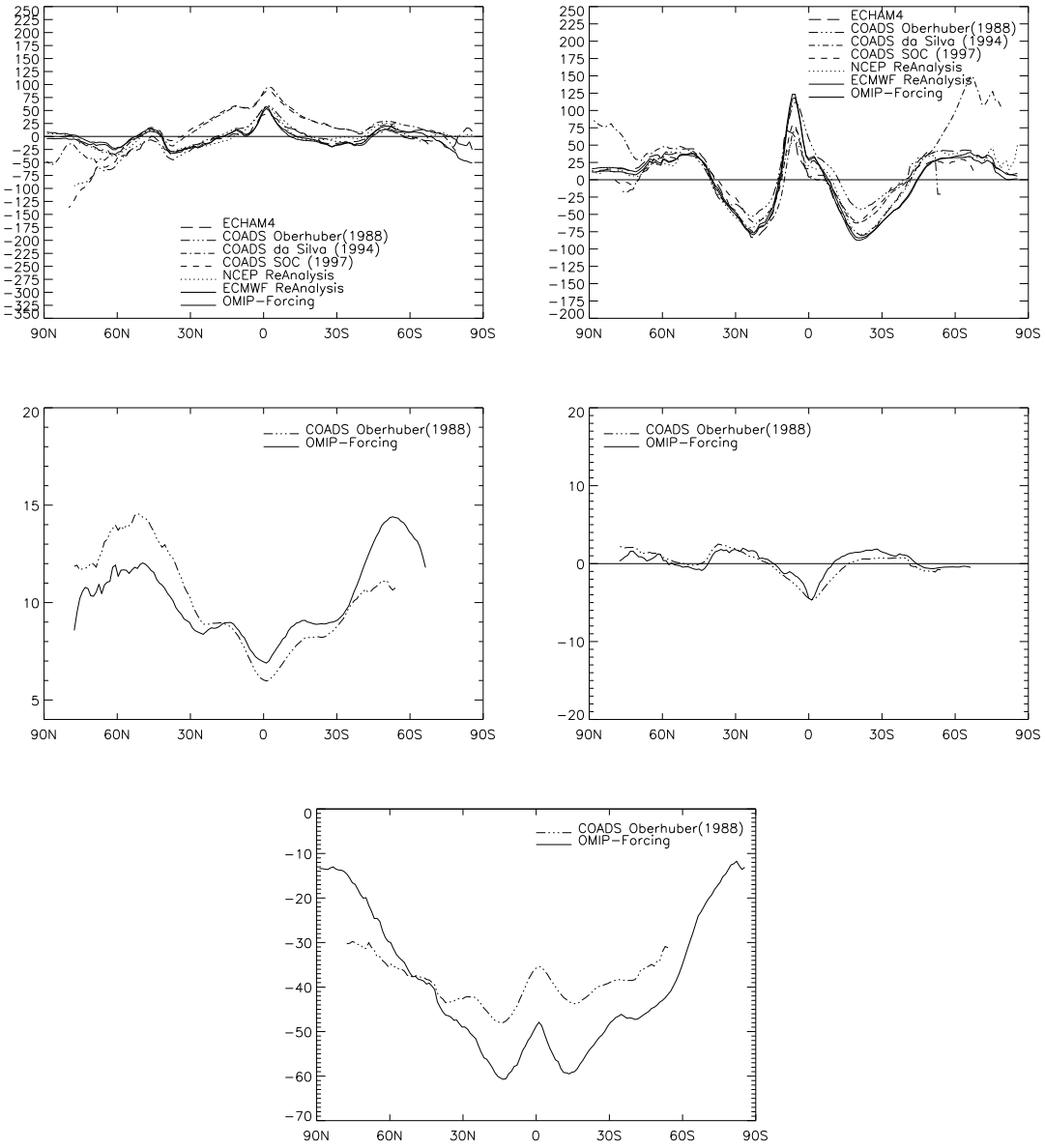

Figure 5.11:
Zonal mean of the fluxes of heat and freshwater (upper left and right panels, Units: $\mathrm{Wm}^{-2}, \mathrm{mm\ month}^{-1}$*), turbulent kinetic energy (middle left, Unit:* $\mathrm{mm\ s}^{-1}$*), surface buoyancy (middle right, Unit:* $10^{-8}\mathrm{m}^2\mathrm{s}^{-3}$*) and Newtonian cooling coefficient (lower panel, Unit:* $\mathrm{WK}^{-1}\mathrm{m}^{-2}$*).*

Chapter 6

Some preparatory control experiments

The physics implemented in the models are outlined in section 3. Here we described some experiments related but prior to the intercomparison experiment.

6.1 MOM2: forced by climatology

6.1.1 Description of experiments

Model differences are generally due to differences in the basic design (equations, numerics, grid), initial and boundary conditions, and parameterizations of subgrid scale processes. Differences not due to basic design can best be explored in the framework of a single model. Transport of tracers is perhaps the most important task in a coarse resolution model. Therefore, we present results from five experiments with different realizations of the tracer transport equations. The experiments are characterized by the advection-diffusion algorithm for tracers as follows:

- V1.1: horizontal Laplacian diffusion, vertical diffusion with a constant coefficient
- V1.2: FCT advection scheme, no additional (explicit) diffusion
- V1.3: FCT advection scheme and isoneutral diffusion
- V1.4: FCT advection scheme, isoneutral diffusion, Gent-McWilliams (GM) parameterization of eddy induced transports
- V1.5: as V1.4, however, with added explicit vertical diffusion where the diffusion coefficient increases with depth (Bryan and Lewis, 1979; see section 3.1)

These experiments were conducted using MOM under climatological forcing and without coupling the sea ice component. The forcing consists of monthly mean wind stress data from Hellerman and Rosenstein (1983), and monthly mean SST and surface salinity fields from Levitus et al. (1994). Predicted surface tracer fields were restored towards the prescribed reference fields with a time constant of 30 days. No continental run-off was considered.

The experiments were run for 500 years starting from rest and potential temperature and salinity distributions taken from annual mean climatological data (Levitus and Boyer, 1994; Levitus et al., 1994). This integration time allows adjustment of velocity and tracer fields in the areas of fast transports, i.e. the boundary currents including the Deep Western Boundary Current (DWBC) and the Antarctic Circumpolar Current (ACC). However, complete equilibrium is not achieved in the deep basins and other regions that depend on diffusive exchanges.

As additional diagnostic elements we introduced artificial tracers that have their origin at the surface in source regions of certain water masses. T3 is prescribed to have values of one at the surface north of 60° N, thus marking the dense water masses formed in the northern North Atlantic. T4 has surface values of one in the Mediterranean, while T5 has surface values of one south of 60° S. In all other regions, surface values of zero are prescribed. Initial values for these tracers are zero. Non-zero values of tracers T3-5 in the interior can be interpreted as the relative volume that has been replaced by water that was in contact with the surface in the respective source regions of the tracers since the start of the integration.

For model verification and to investigate the tracer uptake of the model at different stages of the experiments we use one species of freons (CFC 11). Initial values are set to zero and the CFC concentrations in the atmosphere are prescribed for a period of 50 years (Warner and Weiss, 1992), encompassing the history of increasing use of CFCs until recently. The exchange at the ocean surface is implemented following Dixon et al. (1996). There is no provision for sea ice cover at high latitudes. We therefore tend to estimate too high uptake rates. The initialization of CFCs at the start of an experiment is repeated after an integration time of 500 years and the model integrated for another 50 years. Comparison of the CFC distributions after 50 and 550 years for configurations V1.3 and V1.4 allows to evaluate the development in the tracer uptake rates of the model depending on the ocean state.

6.1.2 Influence of advection-diffusion schemes

Basin-averaged profiles of temperature and salinity give a first impression of the performance of the advection-diffusion schemes in the tracer equations (Figure 6.1). Experiment V1.1 consistently shows largest deviations from climatology among the experiments. Largest deviations occur at mid-depth while the surface values are tied to climatology by the surface restoring condition and the deep values had not enough time to move far from the initial conditions. All experiments have a too pronounced presence of Mediterranean Water while the observed minimum due to AAIW in the Atlantic is only resolved in V1.4 with the Gent-McWilliams parameterization enabled. V1.4 also reproduces the Pacific water mass structure relatively well although the profile is shifted towards lower temperatures and higher salinities below around 700 m. Experiments V1.2 and V1.3 show a salinity minimum that is too weak but low salinity waters occupy a large depth interval (500-3000 m). Isopycnal mixing enhances this effect.

Inspection of the temperature distribution at 100 m depth and its deviations from annual mean climatological conditions (not shown) reveals generally very strong fronts in all model versions, even with Laplacian mixing in V1.1 (Figure 6.2). The case without explicit diffusion, V1.2, exhibits unrealistically fine structure for the mean field. There are apparent deficiencies in the tropics in all model versions, both in the Atlantic and Pacific. The slope of the equatorial thermocline is not well reproduced; the eastern tropics are too warm in V1.1, too cold in all other versions except V1.5. V1.2 has the smallest problems here; additional isopycnal mixing in V1.3 reduces the temperatures too much. The GM parameterization in V1.4 re-establishes the thermocline tilt but is still too cold in the eastern tropics. In the subtropical north Atlantic we notice that the temperature gradients are too zonal in all versions. This problem and the tropical deficiencies might be connected because a Rossby wave characteristic is visible in all difference plots (not shown), involving latitudes up to 40° at eastern boundaries. This hints at problems at the eastern boundary - the wrong signal travels with the Rossby waves into the interior - or at problems with the damping of Rossby waves - too much damping arresting the signal too early on its way into the interior. In the Southern Ocean, we find too high temperatures except in V1.5. The seeming improvement is due to deep mixing bringing up relatively cold water. The mixing is inhibited in V1.4 where the eddy parameterization tends to flatten the slope of isopycnals. With additional diapycnal mixing the shallow pycnocline becomes susceptible to convection in V1.5.

At 1000 m (not shown) all version, except V1.4, are too warm because the permanent thermocline is too thick. There is a special problem in the Atlantic due to too much Mediterranean Water. However, the basic differences between Indian Ocean, Pacific, and Atlantic are rather well represented. Advective signatures like the spreading of NPIW are well represented at least in the

versions with low diffusivity (V1.2 and V1.3). The northern North Pacific is nevertheless too warm and consequently the contrast to the subtropics too small.

Besides problems with Mediterranean Water, the models also yield an acceptable salinity representation at 1000 m depth (Figure 6.3). Especially V1.2 and V1.3 reproduce the broad salinity structure in the Pacific. The experiments with GM show a very smooth salinity distribution without much structure at this depth. It is remarkable that V1.3 is the only version that captures the observed salinity minimum in the Southern Ocean that extends from the southern tip of Africa to South America. This seems important for the formation of Antarctic Intermediate Water (AAIW) with correct properties in the model. All versions lack a source of saline water in the northwestern Indian Ocean.

Sections through the Atlantic at 30°W (Figure 6.4 and Figure 6.5) show overall superior reproduction of the climatology with V1.5. Intermediate layers are still too warm and the Circumpolar Deep Water (CDW) is too cold and homogeneous. Also, the AAIW is too warm, although it is clearly present as a distinct water mass and occupies roughly the observed range of depths and latitudes. The spreading of AAIW is clearly visible in the salinity section of V1.5. However, V1.3 seems to contain a larger volume of AAIW on this section and here the comparison with climatology is clearly better. None of the model versions delivers a satisfactory salinity distribution in the Southern Ocean, which turns out too fresh and too stratified in the vertical.

The artificial tracers T3 and T5 (not shown) on this section (Figure 6.6) reveal the much more vigorous transport of NADW in the GM experiments V1.4 and V1.5. At the equator in 1500 m depth, almost half of the water has been replaced with water in contact with the surface north of 60°N within the integration. For comparison, in V1.3 this share is below 20%. Judged from the concentrations of T5, AABW and AAIW have a larger distribution on this section in V1.4 and V1.5 compared to V1.3. These differences are due to the additional eddy induced tracer transports that are present in the experiments with GM parameterization. GM enhances the strength of the effective (geostrophic plus eddy induced flow) NADW overturning cell and slows the Deacon cell in the Southern Ocean that partially blocks the spreading of AAIW and AABW.

Turning now to the streamfunction ψ for the vertically integrated flow as a first description of the circulation in the models, we note that subtropical and subpolar gyres are of similar strength and location in all model results (Figure 6.7). The experiments with minimal diapycnal diffusion, V1.2 and V1.3, contain some small scale features that are not present in the other cases. With the GM parameterization (V1.4 and V1.5) the subpolar gyre in the North Atlantic is weaker than in other cases, indicating a weaker forcing of the flow through the JEBAR. Striking differences, however, are present in the Southern Ocean where the flow through Drake Passage varies from 170 Sv (V1.3) to less than 60 Sv (V1.4 and V1.5). While the first estimate is on the high side of estimates for the strength of the ACC at Drake Passage (Whitworth et al., 1982, Saunders and Thompson, 1993, Rintoul et al. 2000), the latter is clearly too low to be realistic. Borowski et al. (2000) find that

$$f\boldsymbol{\nabla}\psi = \boldsymbol{\nabla}\chi + \frac{gH\rho_b}{\rho_0}\boldsymbol{\nabla}H \tag{6.1}$$

holds in good approximation for blocked geostrophic contours. Here,

$$\chi = \frac{g}{\rho_0}\int_{-H}^{0} z\rho dz \tag{6.2}$$

is the potential energy integral and ρ_b is the density at the bottom. The potential energy integral χ in the region of Drake Passage is compared for experiments V1.2 and V1.5 in Figure 6.8. We have subtracted a horizontal mean density profile before computing χ and show χ/f_0 with f_0 the Coriolis parameter for the central latitude 60°S. We find good coincidence between the streamfunction ψ and χ/f_0 in both cases. The shelf break near Antarctica is an exception because the topography

determines the spatial variability of χ there. The low transports in V1.4 and V1.5 are due to the special density distribution in the Southern Ocean, or more specifically the meridional gradient of the potential energy integral χ (Mertz and Wright, 1992; Gnanadesikan and Hallberg, 2000).

In general, we find that the GM parameterization leads to less available potential energy (APE). This is not surprising as the parameterization includes the release of APE due to the baroclinic instability process. However, the mean circulation and the Ekman pumping are apparently not sufficient to re-supply APE at the necessary rate to maintain the potential energy distribution for an ACC of observed strength. In the comparison experiment below we shall present streamfunction results with GM parameterization that contain a ACC that is more realistic, with a Drake Passage transport of 110 Sv (slightly stronger than the HOPE result where no GM parameterization was employed). Compared to the sensitivity studies in this section, this could be due to stronger Ekman pumping north of the ACC, or stronger differences in water mass characteristics north and south of the ACC. However, the higher transports could simply result from the shorter integration time, leaving the potential energy distribution closer to initial climatological values than in our 500 years integrations presented here.

Available potential energy can be increased by diapycnal mixing (Bryan and Lewis, 1979). The low ACC transport rates in V1.4 were the motivation for experiment V1.5, where we increased diapycnal mixing by including a depth dependent mixing coefficient. The results point in the right direction; however, the quantitative effect on the ACC was rather minor. Our results are consistent with those of Danabasoglu and McWilliams (1995) who found decreasing ACC transport with increasing diffusivity. With the same value for the diffusion coefficient, the transport in their model is always lower with GM isopycnal thickness mixing compared to horizontal mixing. The ACC transport decreases approximately with $A_I^{-1/3}$. Danabasoglu and McWilliams suggest increased vertical momentum flux that supports more drag with weaker flow in the ACC as a possible cause. In the light of recent studies by Gnanadesikan and Hallberg (2000) and Borowski et al. (2000) it seems more likely that the changes in density structure and the thermal wind are responsible.

6.1.3 Tracer uptake experiments

Freon inventories as a function of latitude show largest differences between V1.3 and V1.4 in the Southern Ocean while the differences north of 20°S are relatively minor (Figure 6.9, upper panels). Maxima in the inventories are located around 40°S, around 25°N, and at high northern latitudes. Only V1.4 contains high values at high southern latitudes. Horizontal maps of CFC11 concentration at 220 m depth (Figure 6.10) show enhanced communication with the surface in the Weddell and Ross seas with the GM parameterization. In fact, high concentrations of CFC down to large depths (see the distribution at 860 m in Figure 6.11) cause the large inventory in V1.4. south of 60°S. England and Hirst (1997) report excessive uptake of CFC in the Southern Ocean due to poor reproduction of the Southern Ocean water mass structure in different versions of their global model. Insufficient stratification and too buoyant deep water leads to extensive penetration of convective adjustment to great depth, thereby moving water rich in CFC to depth. They find these deficiencies remedied by the GM parameterization that also reduces the slopes of isopycnals in the ACC and thus the deep penetration of CFCs by isopycnal mixing. The large inventory in V1.3 further north, on the other hand, is due to deep penetration of waters high in CFC concentration in the ACC belt. Here, surface waters are pushed down in the northern branch of the Deacon cell. The Deacon cell is much reduced due to the eddy induced tracer transports of the GM scheme in V1.4.

The inventories of Figure 6.9 also show that the only other region, except for the Southern Ocean, where subsurface layers store significant amounts of CFCs are the mid latitudes of the northern hemisphere. The deep water formation areas in the northern North Atlantic occupy too small an area as to yield a large contribution to the total inventory. The downward transports due to Ekman pumping and the formation of subtropical mode waters, especially in the Pacific, are apparently much more effective processes in this respect.

At 200 m, both model versions behave similarly and the CFC concentration mainly follows

the large scale distribution of upwelling and downwelling. One exception is the Labrador Sea, where convection brings relatively high concentrations down to 200 m depth despite the subpolar upwelling. The western boundary currents of the subtropical gyres and their extensions are characterized by low CFC values. It was previously noted that the reduction of background diffusion that is possible with the GM scheme leads to reduced upwelling in the western boundary layers because the Veronis effect is curtailed (Böning et al., 1995). Here, we find little quantitative differences between the schemes. This could indicate relatively strong implicit mixing with the FCT scheme in the western boundary current region.

The southward transport of deep water in the model occurs at shallower depths than observed. The maps of CFC concentration at 860 m depths can therefore be compared with recent maps of CFC concentration in the upper LSW by Smethie et al. (2000). The observations show typical values of around 1 pmol/kg in the North American Basin and ten times smaller values in the DWBC off South America. Equatorial values are down to 0.02 pmol/kg. Model values (Figure 6.11) are far lower with around 0.02 pmol/l as maximum concentration in the northern North Atlantic (in the Labrador Sea). Further south, concentrations drop to 10^{-3} off the North American coast. No CFC has reached the equator within the 50 years integration. Relatively high concentrations in the eastern subtropical North Atlantic are due to the inflow of Mediterranean Water. Concentrations in the Labrador Sea are higher in V1.4, however, the southward spreading of CFCs is even weaker than without the GM parameterization. Compared to simulations by Goose et al. (1999), the inventory in our model results is high at all latitudes although the different surface boundary conditions for CFC exchange with the atmosphere favor uptake in the Goose et al. model. The differences in uptake rates are probably caused by the different treatment of sea ice (see model description above).

Because of the role of deep water formation and mode waters, tracer uptake will depend on the state of the ocean and with that on the integration time of a model. Initializing the CFC concentration after an integration time of 500 years and integrating the model for another 50 years yields the inventories shown in Figure 6.9 (lower panels). Overall, the model is not able to take up as much CFC as when starting from climatology. With V1.3 there are also pronounced differences in the vertical distribution of CFC11. Initializing after 500 years, the layers below 500 m and 1000 m become relatively more important. In V1.4 the opposite is the case. Here, almost all the tracer inventory is now above 500 m depth, a consequence of the shallower isopycnals after prolonged integration with the GM scheme. The total inventory, however, is very similar in both model versions.

After 500 years, the model has drifted so far that convection in the Labrador Sea is apparently no longer maintained. Contrary to the results after 50 years, the Labrador Sea no longer stands out with high CFC concentrations. In experiment V1.4, the Irminger Sea still exhibits enhanced concentrations compared to the mean values in the subpolar gyre.

The distributions at 860 m depth (Figure 6.12) show the increased uptake in V1.3 in all parts of the Southern Ocean, including the Weddell Sea. In V1.4, there is virtually no CFC in the Southern Ocean as deep as 860 m depth. The strong deep ventilation in the Ross and Weddell seas is now confined to the southernmost part of the Weddell Sea.

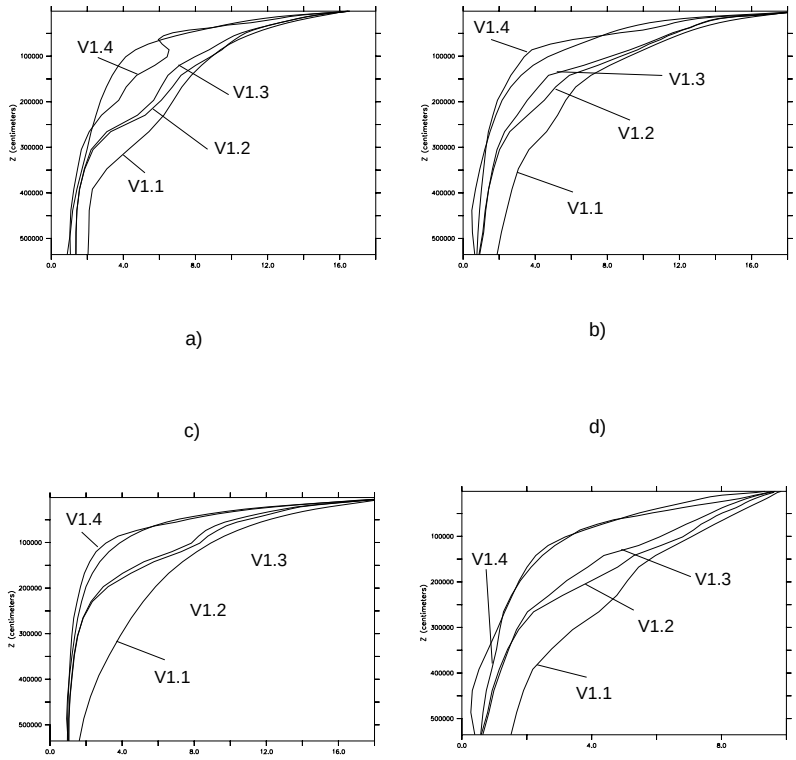

Figure 6.1: Horizontally averaged temperatures for the Atlantic Ocean a), Indian Ocean b), Pacific Ocean c), and Southern Ocean d). Panels e) through h) show corresponding salinity profiles. The unmarked line in each panel represents observed climatology.

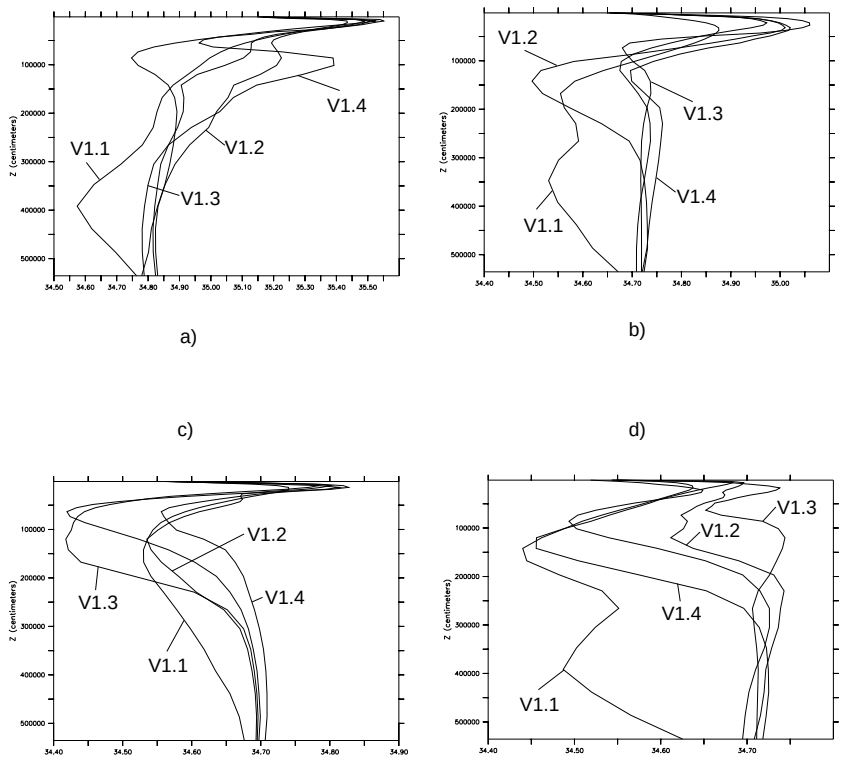

Figure 6.1: Continued.

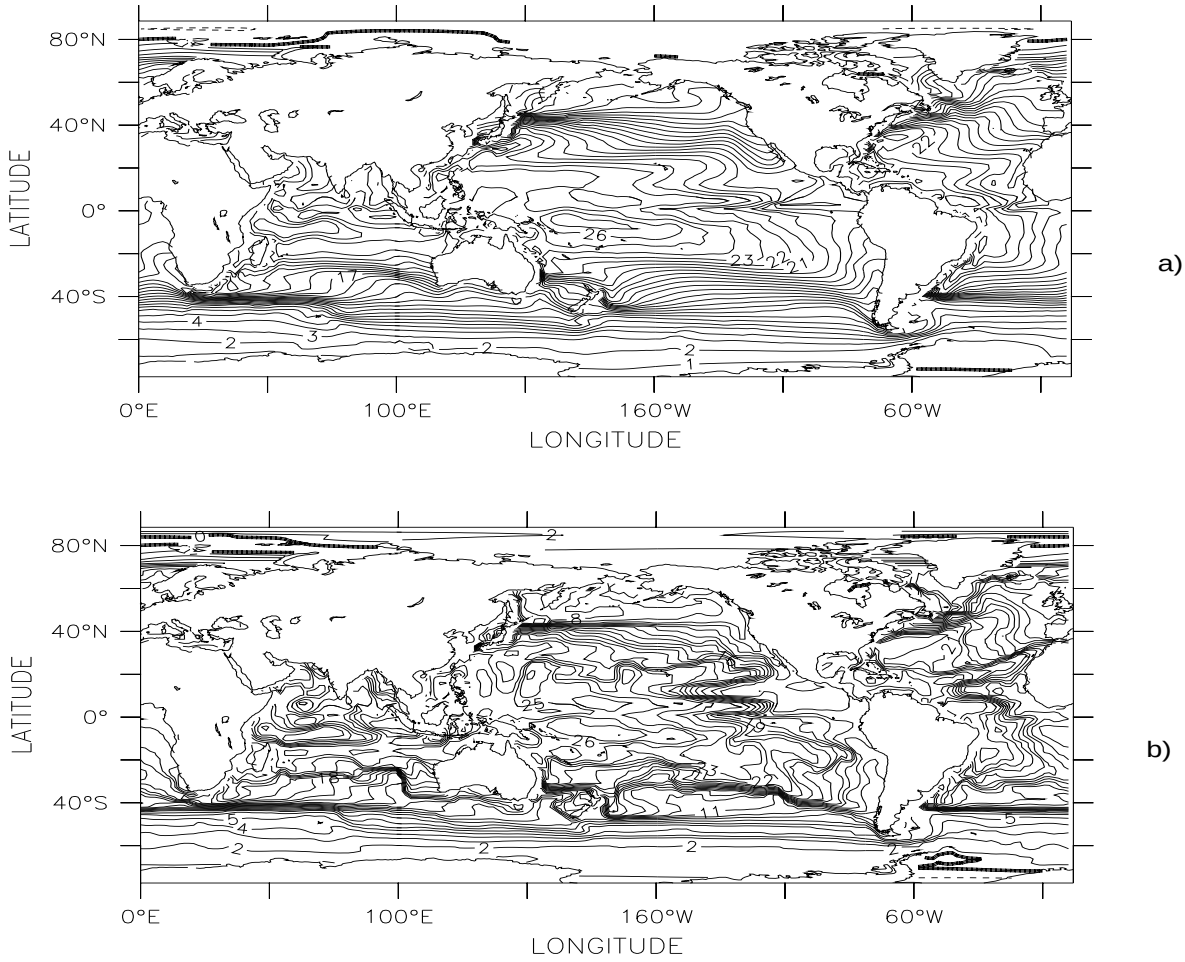

Figure 6.2: Potential temperature at 100 m depth for experiments V1.1 a), V1.2 b), V1.3 c), V1.4 d), V1.5 e). The corresponding climatological mean field is shown in f).

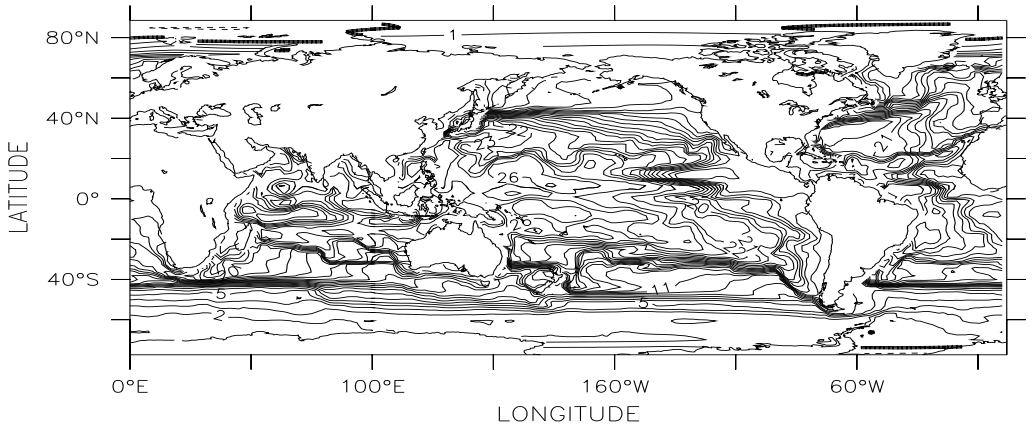

c)

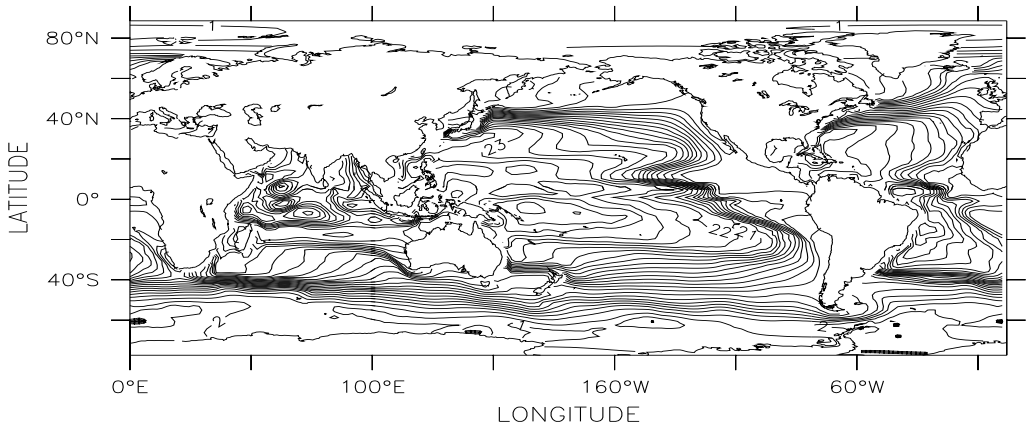

d)

Figure 6.2: Continued.

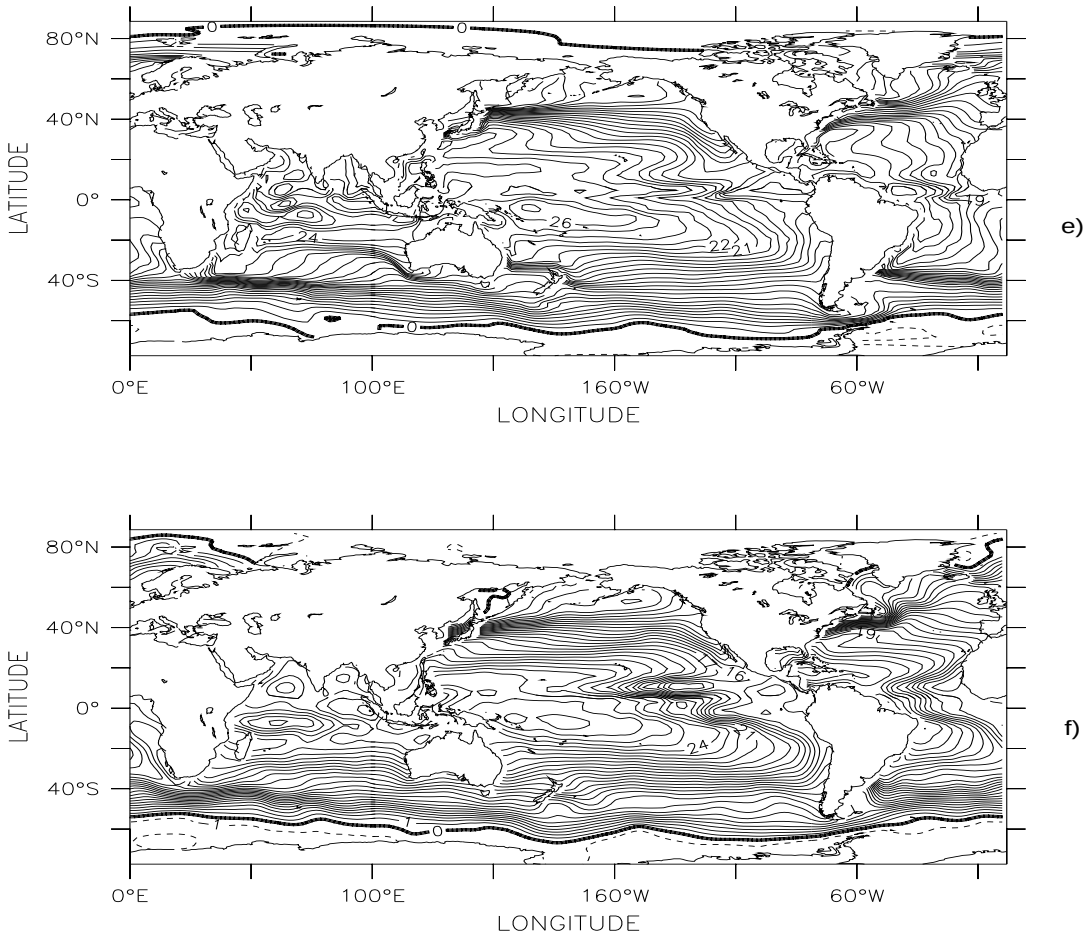

Figure 6.2: Continued.

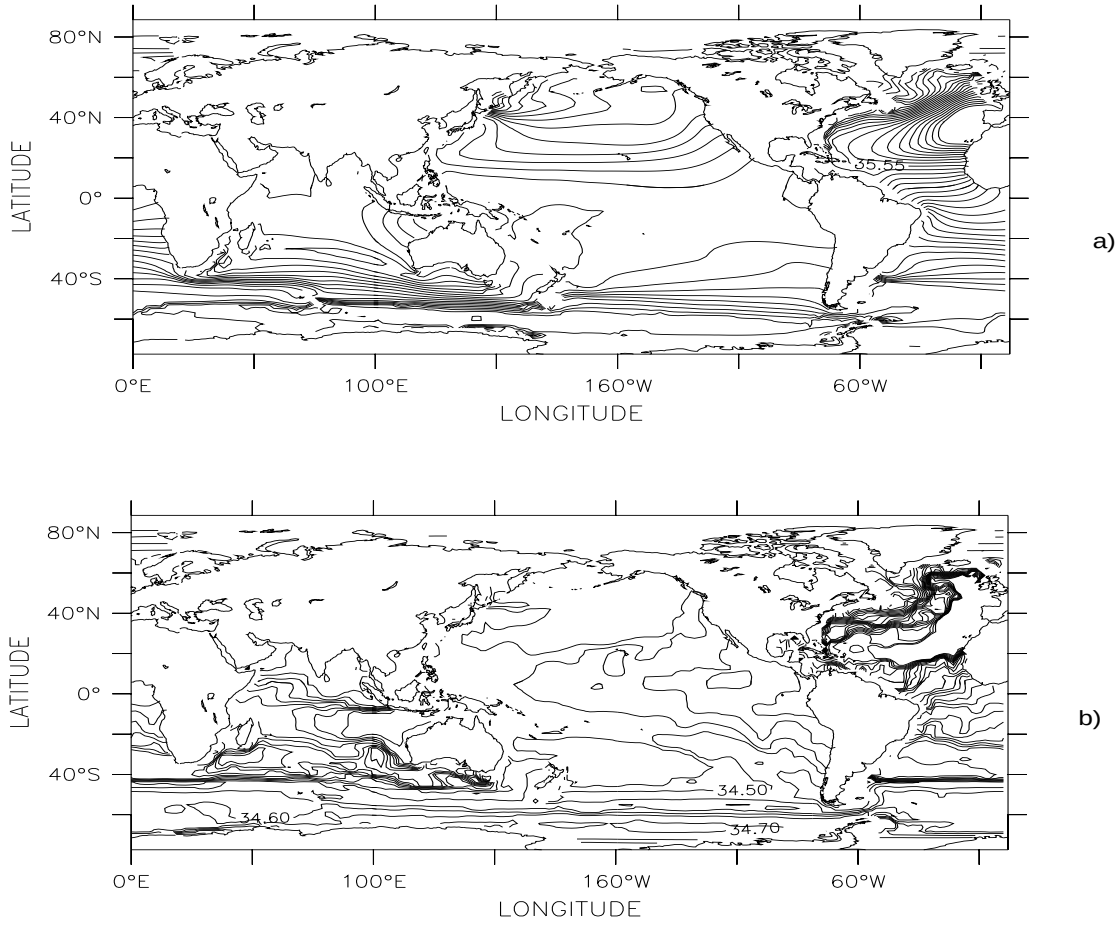

Figure 6.3: Salinity at 1000 m depth for experiments V1.1 a), V1.2 b), V1.3 c), V1.4 d), V1.5 e). The corresponding climatological mean field is shown in f).

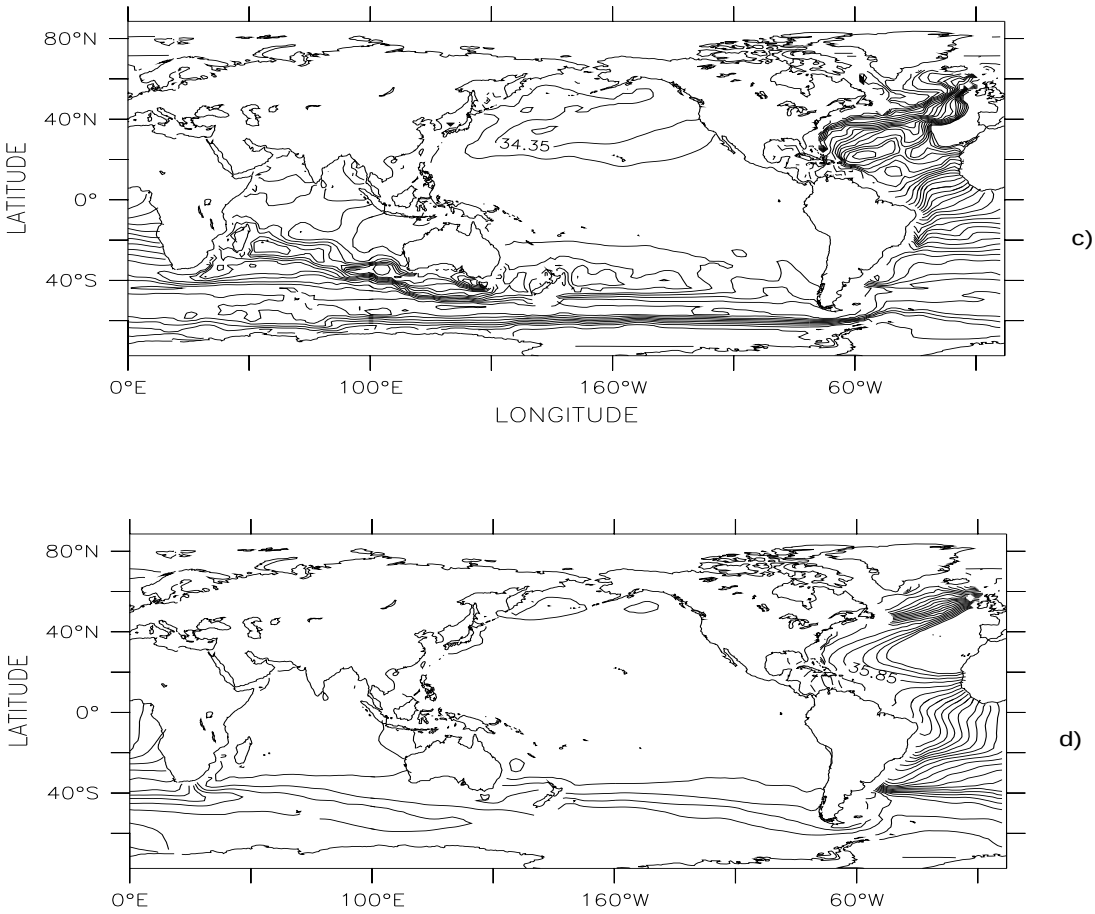

Figure 6.3: Continued.

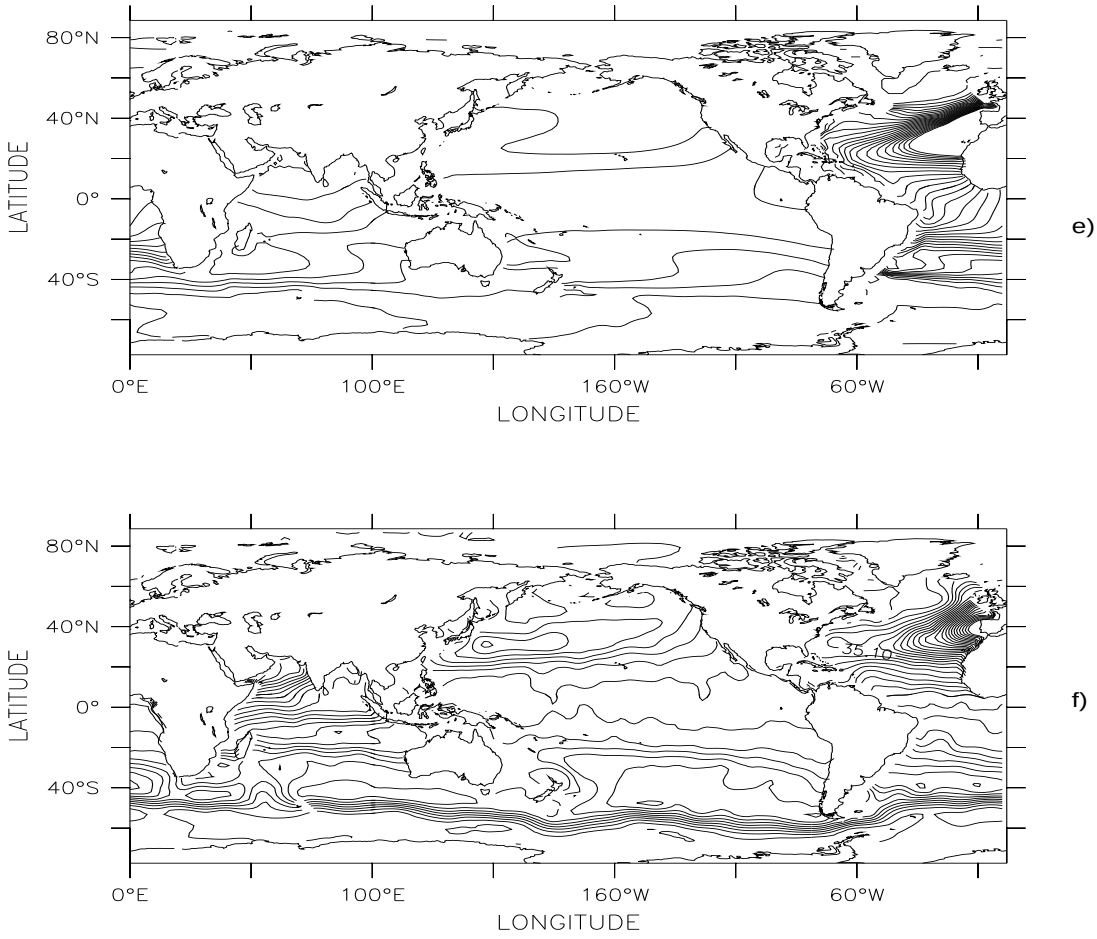

Figure 6.3: Continued.

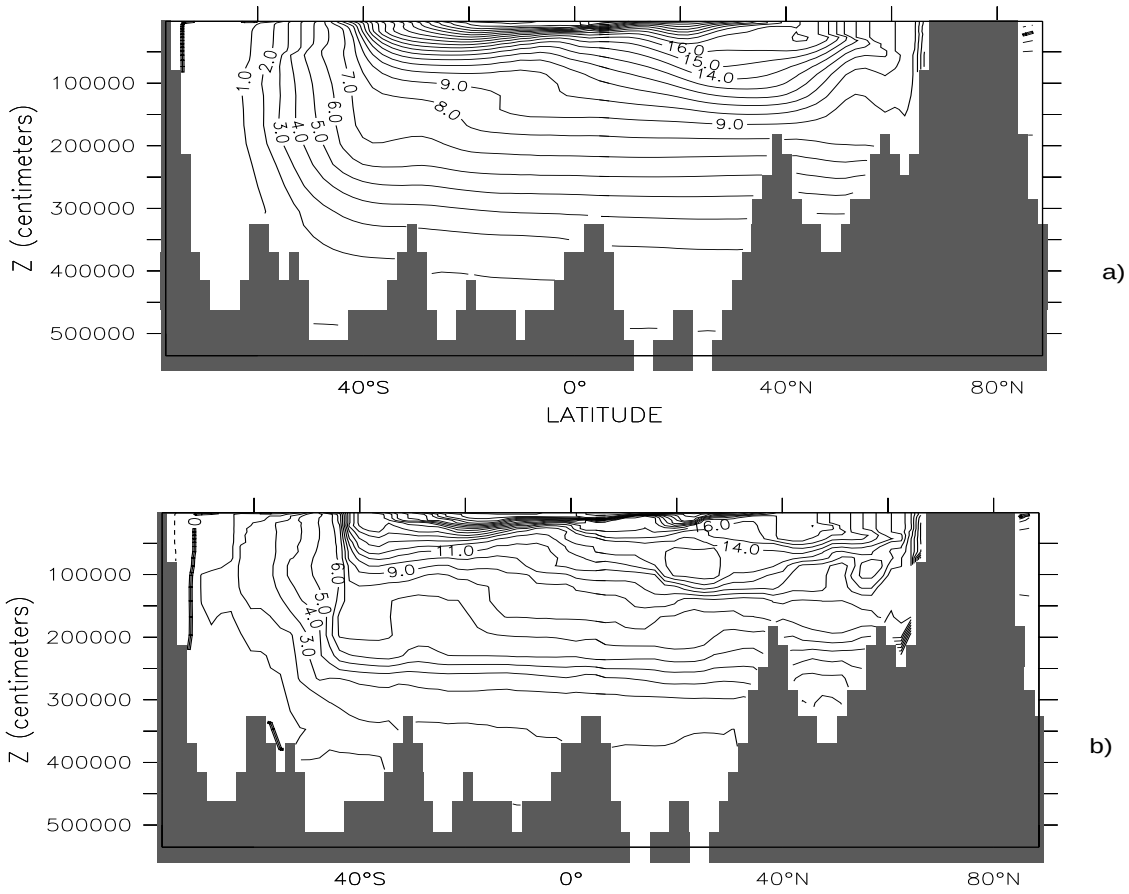

Figure 6.4: Potential temperature at 30°W for experiments V1.1 a), V1.2 b), V1.3 c), V1.4 d), V1.5 e). A corresponding section for climatological data is shown in f).

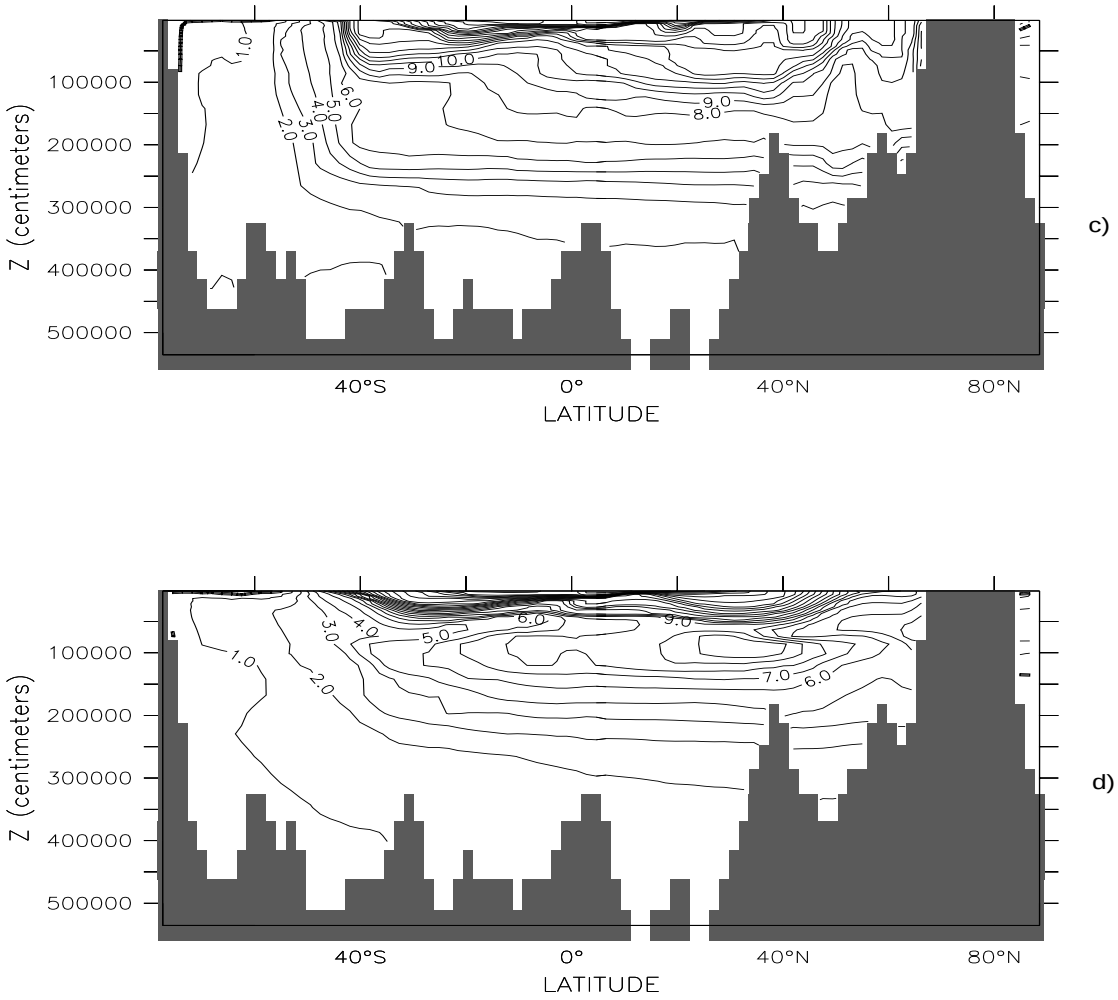

Figure 6.4: Continued.

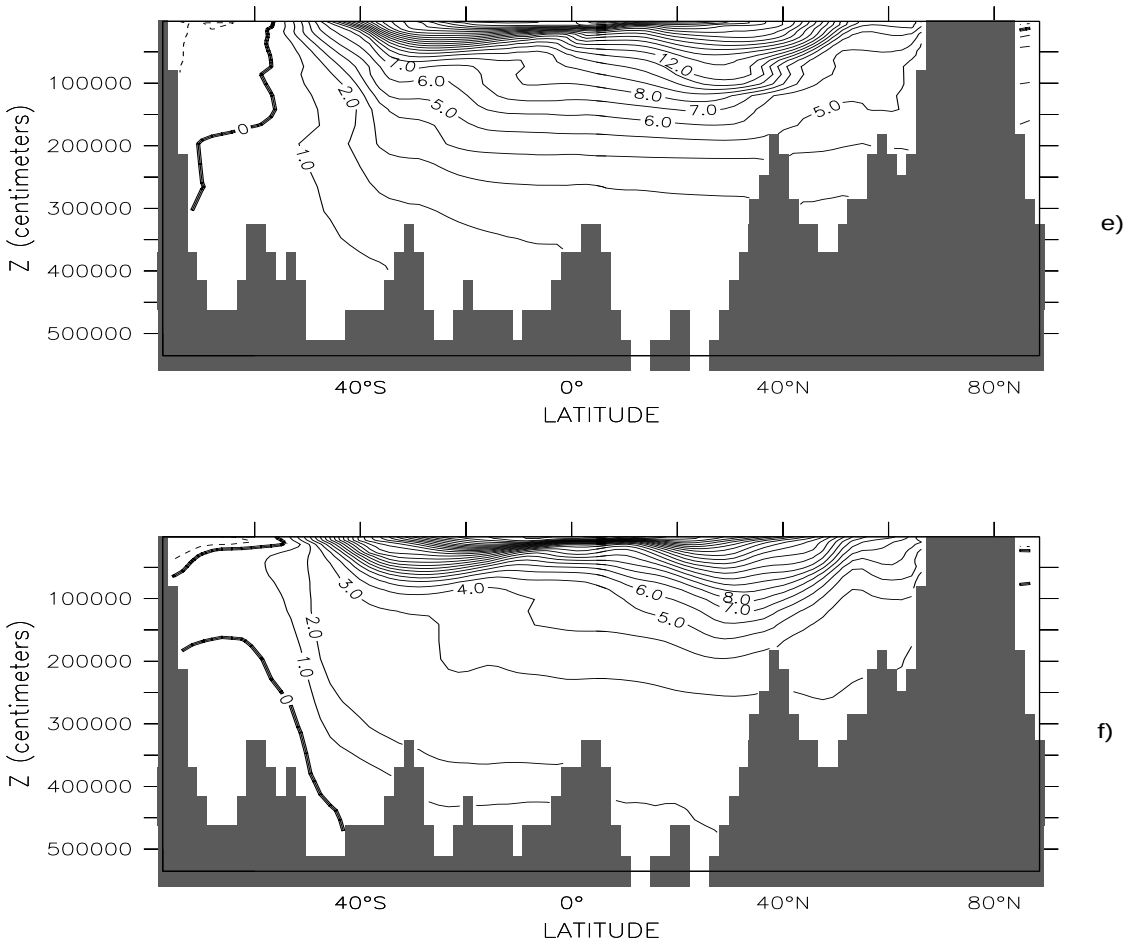

Figure 6.4: Continued.

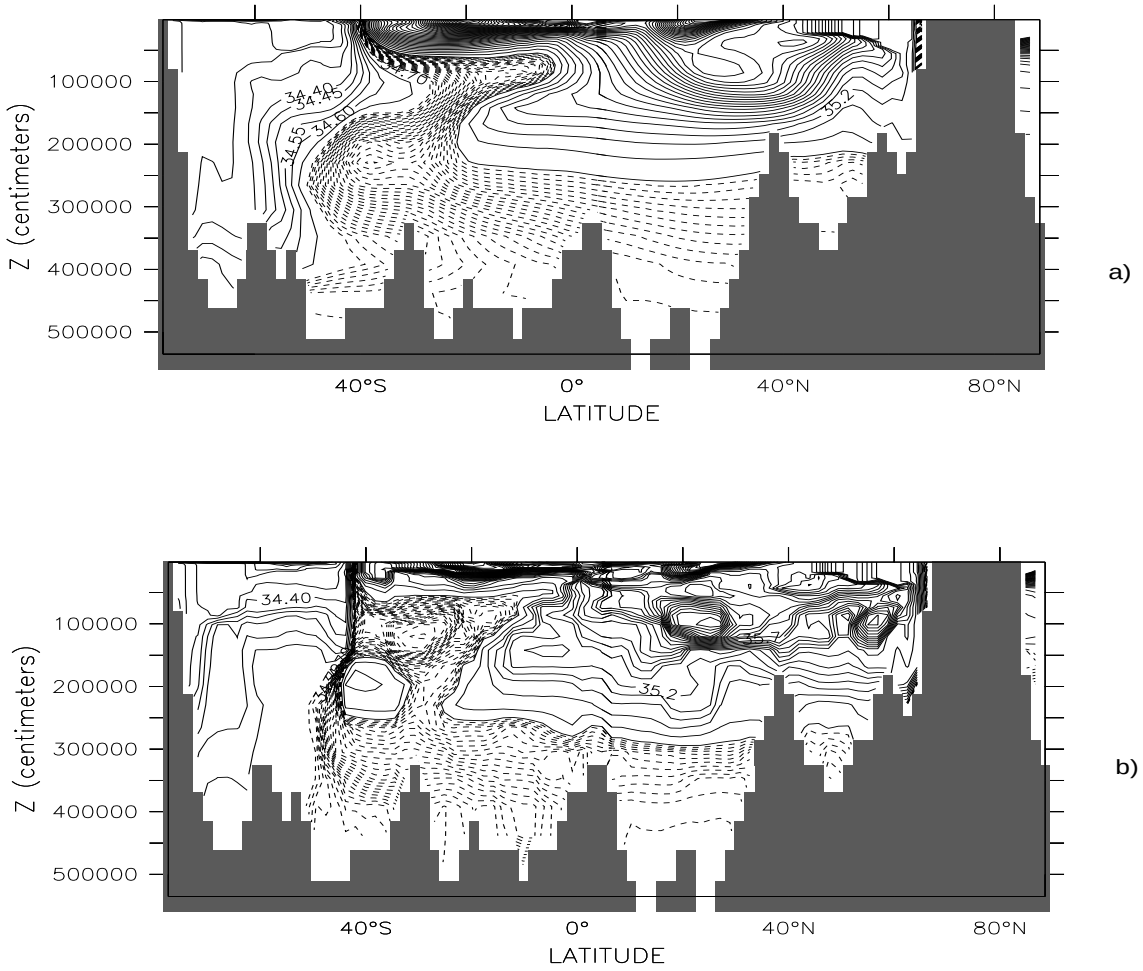

Figure 6.5: Salinity at 30°W for experiments V1.1 a), V1.2 b), V1.3 c), V1.4 d), V1.5 e). A corresponding section from climatological data is shown as f).

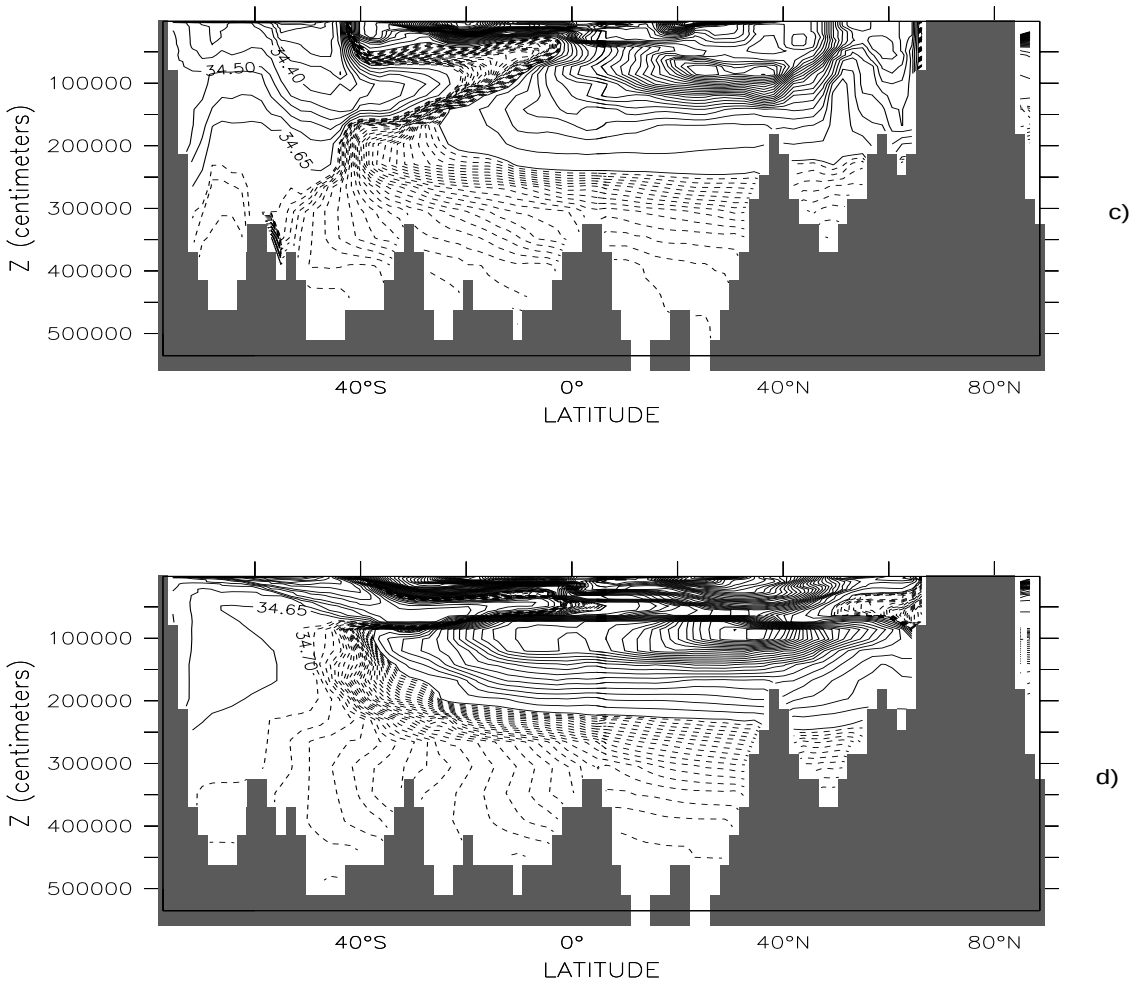

Figure 6.5: Continued.

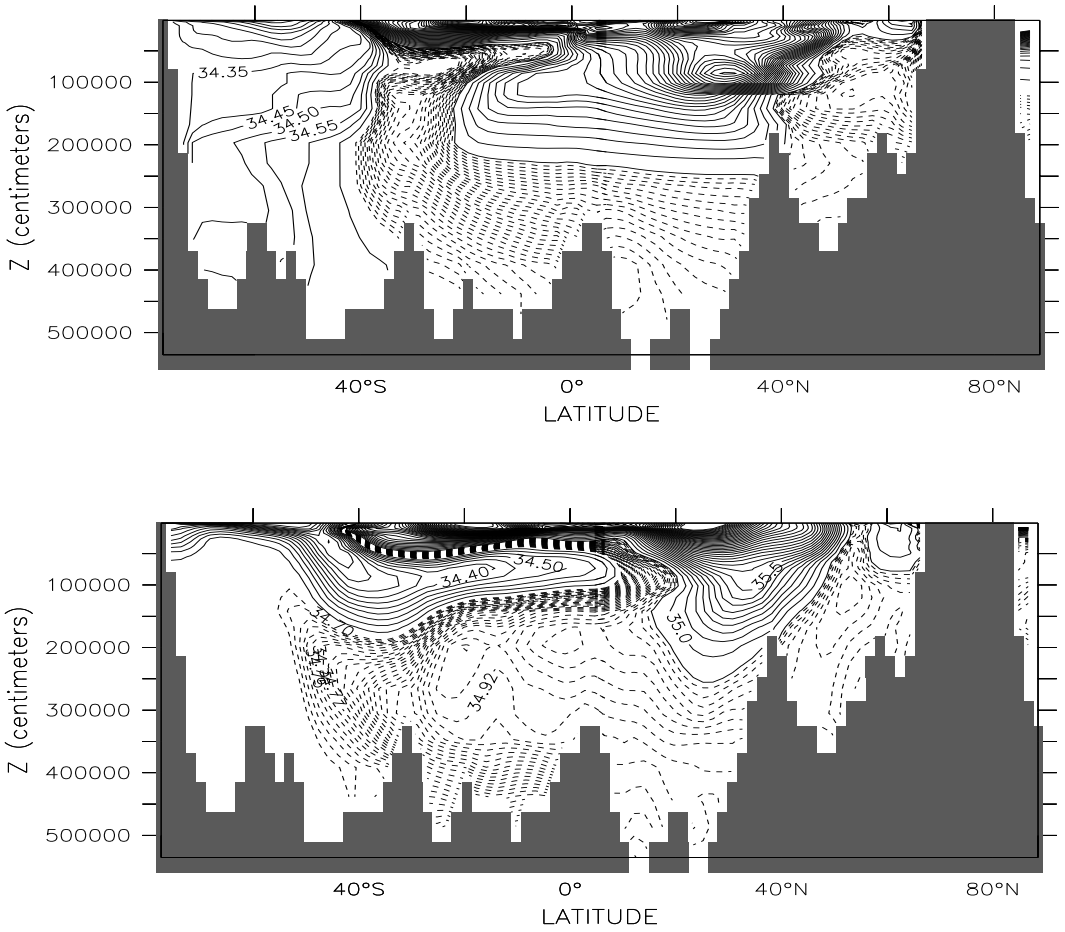

Figure 6.5: Continued.

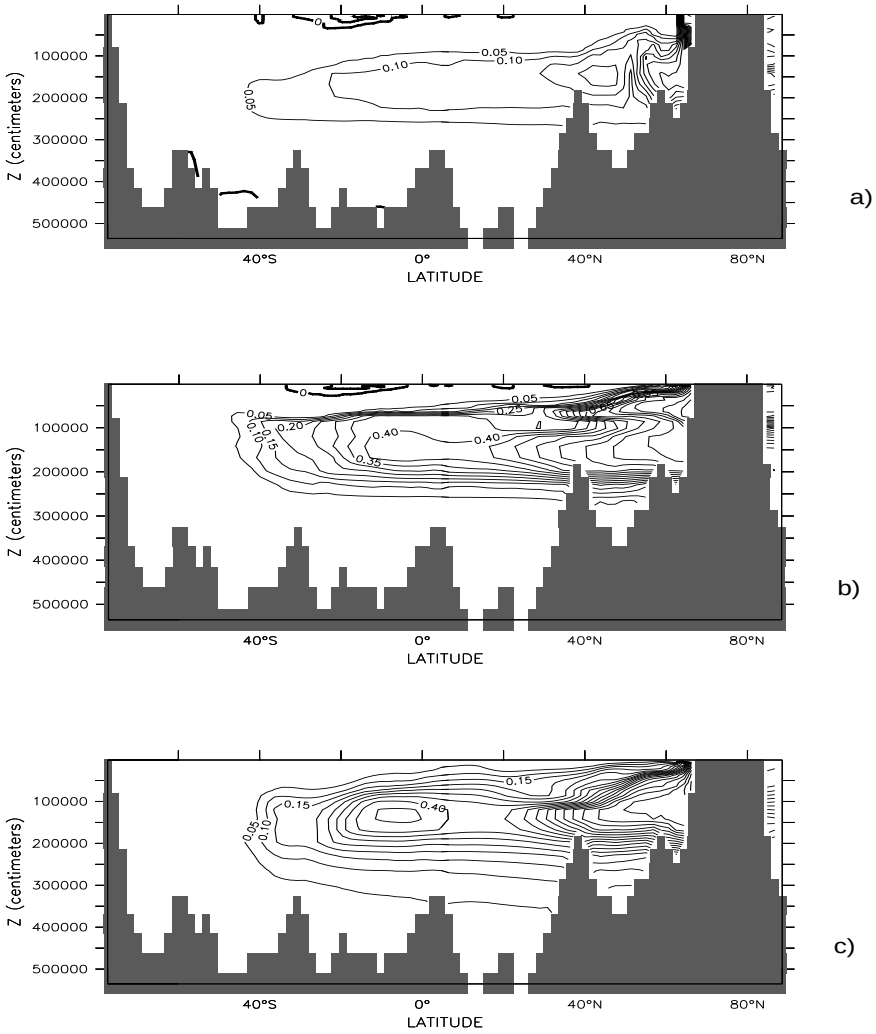

Figure 6.6: Concentration of artificial tracer T3 (source north of 60°N) along 30°W for experiments V1.3 a), V1.4 b), V1.5 c).

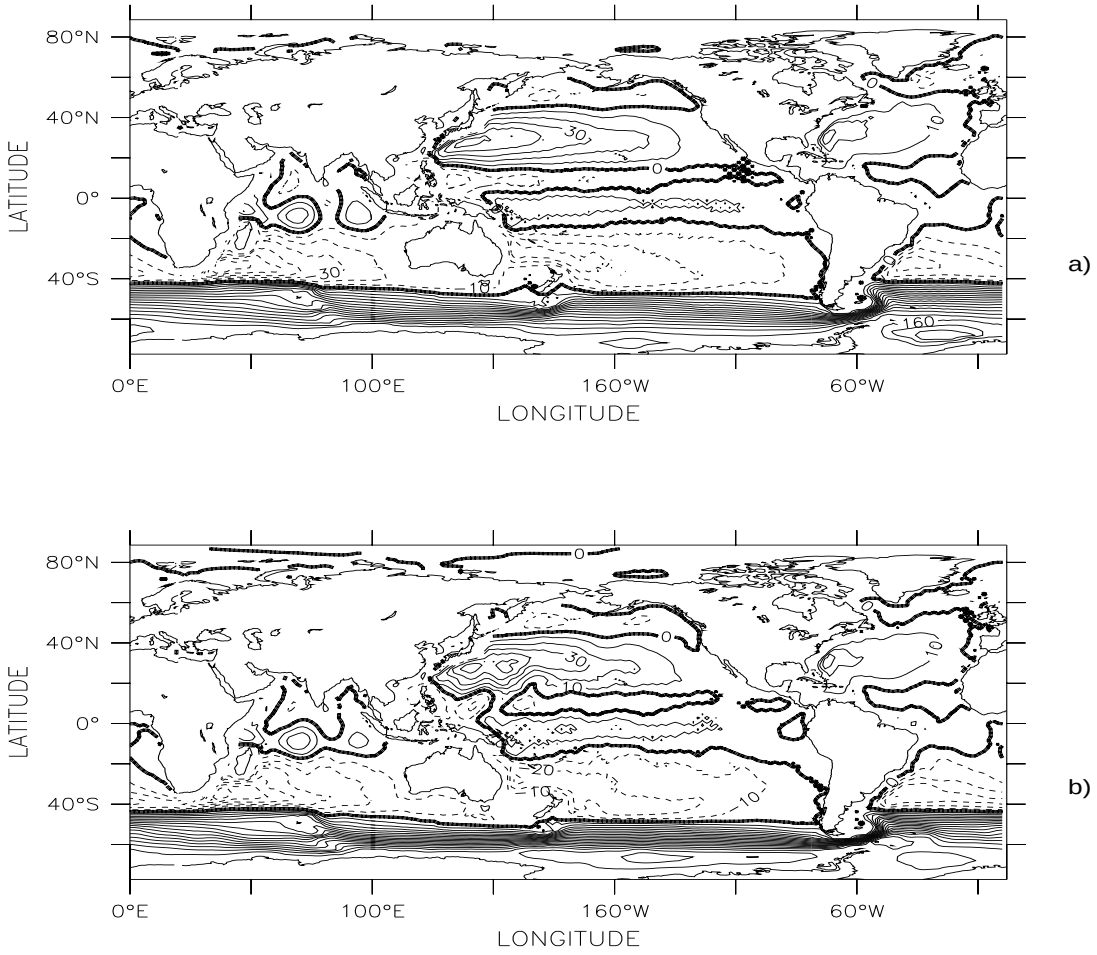

Figure 6.7: Streamfunction for the vertically integrated transport in experiments V1.1 a), V1.2 b), V1.3 c), V1.4 d), V1.5 e).

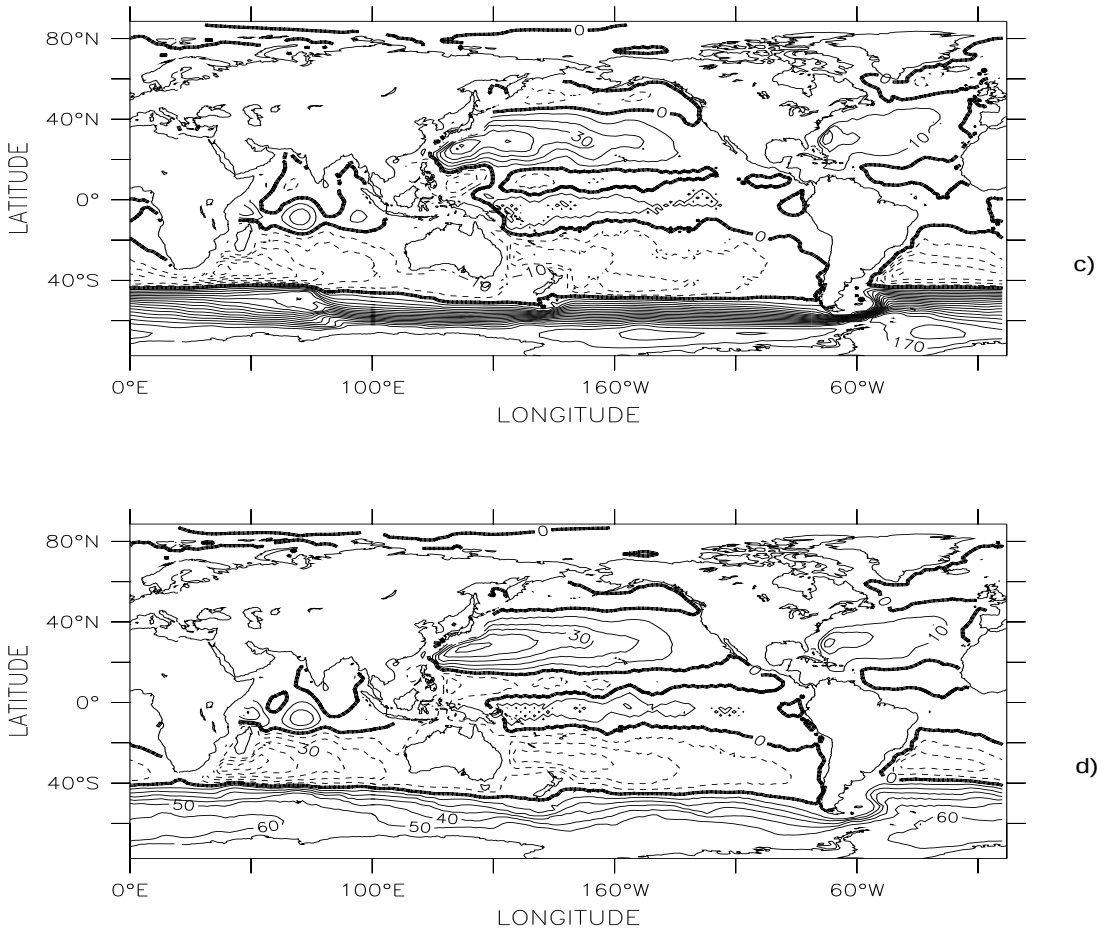

Figure 6.7: Continued.

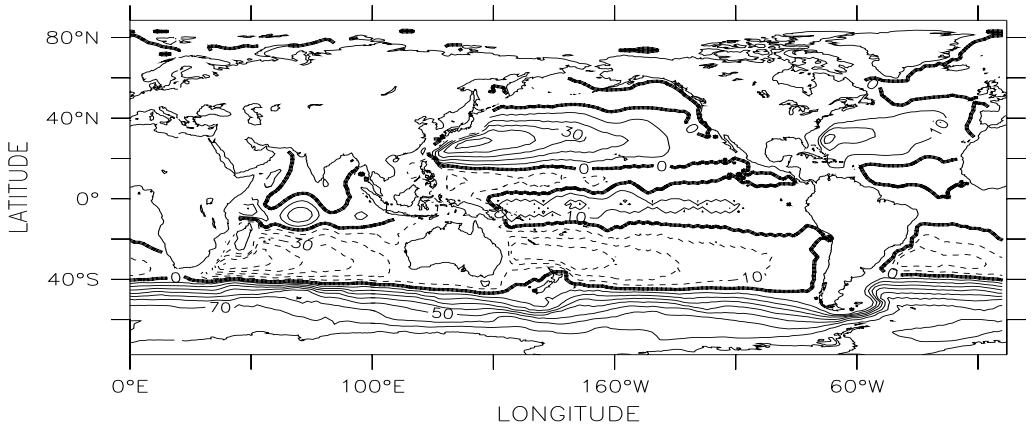

Figure 6.7: Continued.

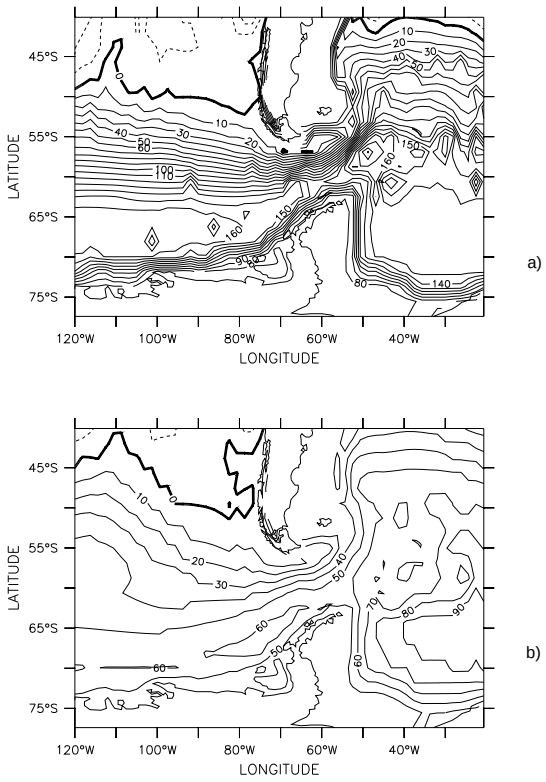

Figure 6.8: Potential energy integral weighted with $1/f(60^{\circ}\mathrm{S})$ (see text) for experiments V1.2 a) and V1.5 b). A dynamically irrelevant constant has been added to yield values comparable to the streamfunction of Figure 6.7.

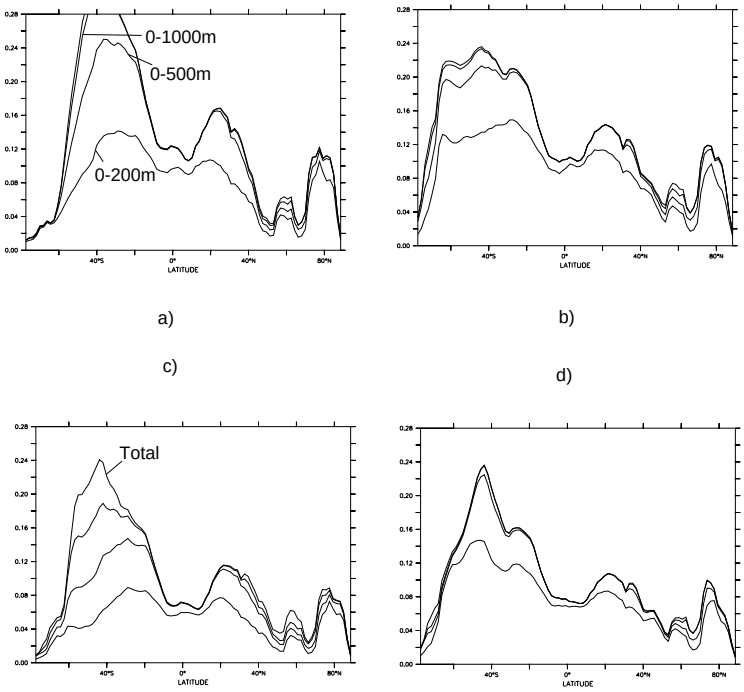

Figure 6.9: CFC-11 inventory after 50 years integration for climatological initial conditions in experiments V1.3 a) and V1.4 b). Panels c) and d) show corresponding results for initial conditions taken from a 500 year integration. Inventories are shown for different depth intervals as indicated in a) and c).

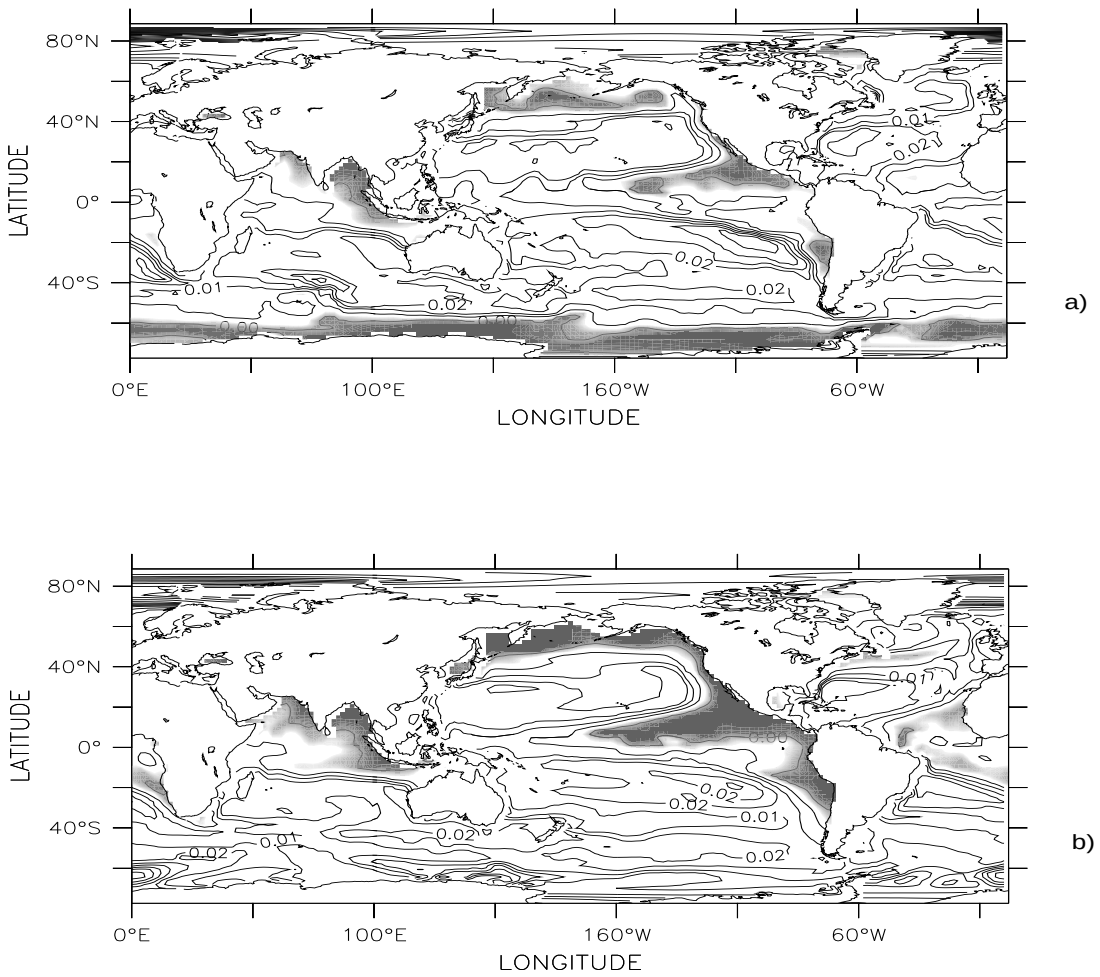

Figure 6.10: CFC-11 concentrations at 200 m depth for experiments V1.3 a) and V1.4 b). These results are obtained after 50 years integration starting from initial conditions. The contour interval is 0.005 pmol/l and values lower than 0.003 pmol/l are shaded.

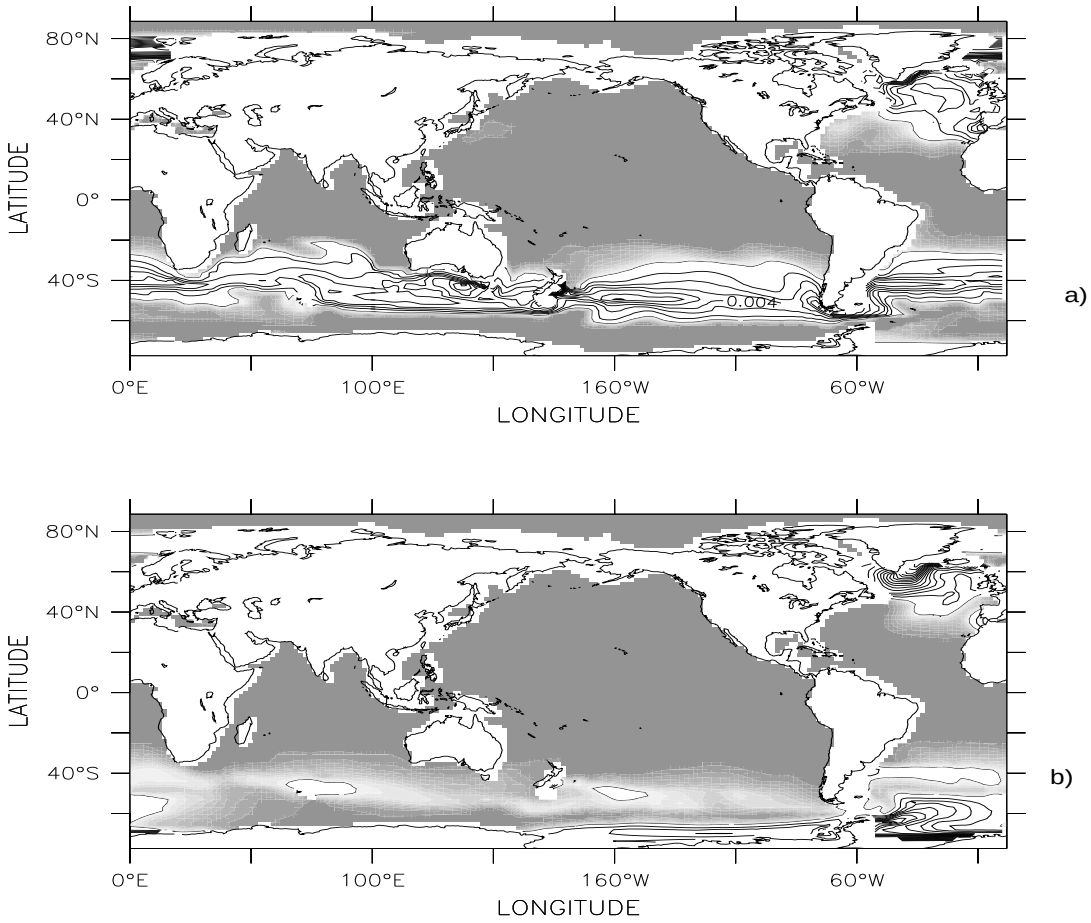

Figure 6.11: CFC-11 concentration at 860 m depth for experiments V1.3 a) and V1.4 b). These results are obtained after 50 years integration starting from initial conditions. The contour interval is 0.001 pmol/l and values lower than 0.001 pmol/l are shaded.

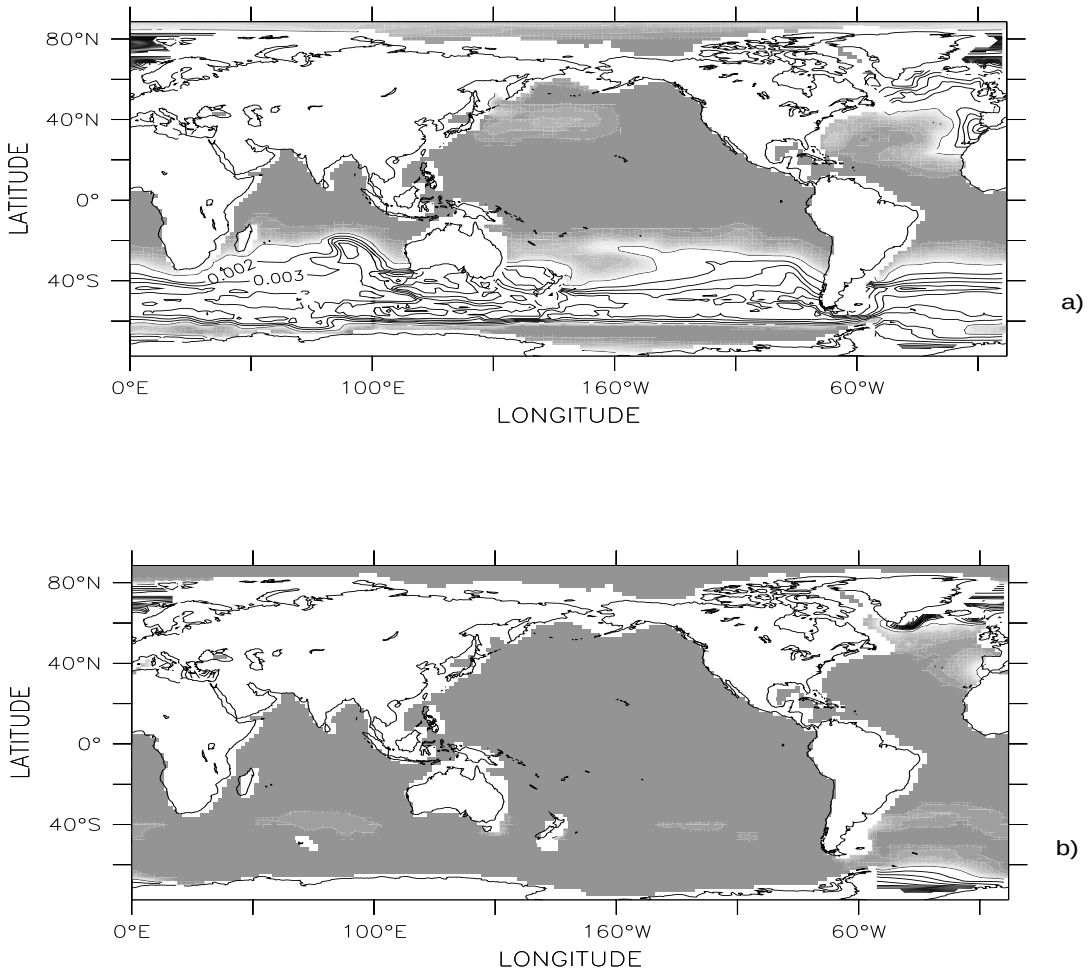

Figure 6.12: CFC-11 concentration at 860 m depth for experiments V1.3 a) and V1.4 b). These results are obtained after 50 years integration starting from the model state after 500 years. The contour interval is 0.001 pmol/l and values below 0.001 pmol/l are shaded.

6.2 HOPE: coupled to ECHAM4

The forcing for the developing phase of the HOPE model has been obtained from an integration of the ECHAM4 atmosphere general circulation model (AGCM). ECHAM4 is the latest version of the AGCM developed at the Max-Planck Institute for Meteorology in Hamburg. The model, which has been adapted originally from the ECMWF weather forecast model, has been extensively modified to adjust it to climate applications. The horizontal representation of the variables (except water components and trace substances) is by a series of spectral harmonics with triangular truncation at wavenumber 42. The vertical domain is resolved by 19 levels with a hybrid $\sigma - p$ coordinate system and extends to 10 hPa. The lowest level is about 30 m above the surface. Most of the parameterized physics is formulated on the associated Gaussian transform grid (T42) which has a grid-cell size of about 2.8° in both directions. Outside the low-latitude regions with refined ocean grid, the atmosphere land/sea mask is identical to the grid composed by the even lines of the ocean grid.

The ECHAM4 model and its climatology obtained with prescribed monthly mean AMIP SST and sea ice extent of the period 1979-1994 is described in Roeckner et al. (1996). ECHAM4 is able to reproduce realistically the observed seasonal mean climate and intraseasonal variability as represented by the ECMWF operational analyses and the Legates and Willmott (1990) precipitation climatology. The most apparent deficiencies concerning the surface fluxes are a warm bias of $2° - 3°$ in the lower troposphere over the Arctic, an easterly bias of the zonal winds in the tropics, particularly over the tropical Pacific, an underestimated summer monsoon, a lack of precipitation in the Mediterranean area, and underestimated westerlies over the Southern Ocean (Roeckner et al. 1996).

The radiation budget is investigated in more detail in Chen and Roeckner (1996). Overall, the model results are in good agreement with the observed budget as represented by the ERBE data. An overestimated short-wave radiative cloud forcing in summer over the tropical oceans is in accord with the underestimated summer monsoon. Over the eastern tropical ocean, the midlatitude oceans as well as over the Southern Ocean, Chen and Roeckner (1996) diagnose a lack of low-level clouds in summer.

The daily mean forcing data for the ocean model were obtained from a 15-year run with monthly AMIP SST of the period 1979-1988 specified at the lower boundary. The averaging period of one day corresponds to the exchange frequency of data between the ocean and atmosphere models in the CGCM. We therefore account already in the forced ocean spin-up experiment for a large part of the high frequency variability of fluxes that will force the ocean in the coupled experiments. Jumps of forcing data between the end and the start of the 15-year period were smoothed by locally applying a running- mean filter on the first and last 5 days of the data period. The data were cyclically repeated during the spin-up.

Chapter 7

The ocean circulation in MOM2 and HOPE

7.1 The comparison experiment

The objective of this study is the intercomparison of the MOM2 and HOPE models as a tool of simulating the mean state of the global ocean circulation, including the annual cycle. As outlined in the previous sections, the model concepts and equations are fairly similar. Differences appear mainly in the parameterization of subgrid processes and the numerics. The intercomparison experiment was set up with model configurations which are – as far as possible – identical. We attempted to use the same resolution, topography and forcing. Differences which still remain are due to differences in the numerical realization of the equations, the different handling of subgrid physics, and experiences and learning from the performance in previous experiments. We considered the difference in the models' setup as marginal.

The models were driven by the same forcing data (see section 5)and the same bulk formulae for the surface fluxes have been used. Before they have been built into the models, they have been adapted to close the heat and fresh water flux budgets. This has been done independent of the models by using the ERA sea surface temperatures.

In addition, the intercomparison setup has been considered in HOPE, which relates essentially to the surface conditions. The formulae, which were the result of the procedure of closing the heat and fresh water flux budgets, have been built into the model. These formulae need input parameters not used so far. Therefore, the reading routines had to be changed accordingly. The fresh water flux is now calculated from precipitation, which is read in, and from evaporation, which is calculated from the latent heat flux considering the ice conditions. In the ice-free part of the cell the heat of vaporization is used and in the ice-covered part the heat of sublimation. Instead of using the atmospheric surface temperature to define the ice edge, the ice concentration is used for this purpose. The mixed layer depth has been built in as a new diagnostic. Apart from these modifications the model parameters of the HOPE model version have not been changed.

The models were initialized from a state of rest using the Levitus climatology of the annual mean temperature and salinity. The integrations span a time of 100 years.

7.1.1 Model domain, resolution and topography

Both models are global. The staggered E-grid of the HOPE model is divided into two subgrids, one for the even rows and one for the odd rows. The position of the even grid lines is that of a Gaussian grid corresponding to a spectral resolution with triangular truncation at wave number 42 (T42). The grid cell size is 2.8125° in both directions. Therefore, a mean horizontal resolution can be specified for the direction from South-West to North-East with approx. $2.8125°/\sqrt{2} = 1.989°$. Also, for the intercomparison the vertical discretization of the HOPE model has been changed. It

has been enhanced from 20 to 25 levels (see Tabtab:listofdepths), whereby the levels remain to be concentrated in the upper ocean with 12 layers above 500 m.

The regular B-grid of the MOM2 model has a horizontal resolution of 1.875° in the North-South and East-West directions. The vertical is discretized by using 29 levels. The vertical discretization of the models is given in Table 7.1.

level	t-points	u-points	w-points		level	t-points	u-points	w-points	
	MOM2	HOPE	MOM2	HOPE		MOM2	HOPE	MOM2	HOPE
1	13	10	25	0	16	860	1224	937	1104
2	38	30	52	20	17	1014	1474	1107	1344
3	66	51	82	40	18	1200	1742	1310	1605
4	97	75	115	63	19	1420	2036	1548	1879
5	133	100	153	88	20	1676	2371	1822	2192
6	173	125	195	113	21	1968	2753	2131	2549
7	217	150	242	138	22	2295	3188	2476	2956
8	266	175	292	163	23	2657	3684	2853	3420
9	318	206	345	188	24	3050	4250	3261	3949
10	373	250	400	225	25	3472	4895	3695	4552
11	428	313	456	275	26	3918		4151	5239
12	485	420	519	350	27	4384		4624	
13	552	580	593	490	28	4864		5109	
14	634	774	684	670	29	5354		5600	
15	735	991	798	877					

Table 7.1: Vertical levels for tracer and velocity points in MOM2 and HOPE: w-points: vertical velocity. u-points: horizontal velocity. t-points: tracer (depths in m.)

Both models use a bottom topography which is slightly different for scalar and vector points, as can be inferred from Figure 7.1 and Figure 7.2. The HOPE topography was smoothed from the original bathymetry data ETOPO5. Starting from the ETOPO5 data set, a 5- or 9-point operator has been applied n-times. Thus, the topography in MOM2 appears more noisy, with strong – and in most cases more realistic – gradients from the deep sea towards the continental shelves and more resolution of most prominent features in the global ocean bathymetry. To handle cross sections of overflow and throughflow regions the bathymetry was corrected, including artificial widening of straits, as usual in coarse ocean models (see e.g. section 3.1 for MOM2).

7.1.2 Diagnostics

Besides the standard output – which includes the 3d velocity field, the hydrographic parameters, surface fluxes, sea ice parameters and streamfunctions – we have applied some simple diagnostic tools to elucidate some aspects of the models' behavior.

Mixed-layer depth

To judge the capability of the models to simulate the deep water mass formation in the higher latitudes a routine was established which calculates the mixed layer depth from the model output. We have followed the algorithm of Levitus (Johnson, priv. comm.). Given is potential temperature, salinity and pressure p_n at the depths z_n, $n = 1, \ldots N$, where N is the number of depths at a specific grid point. The depths z_n are discretized in the models as

$$z_n = \sum_{i=1}^{n} d_i$$

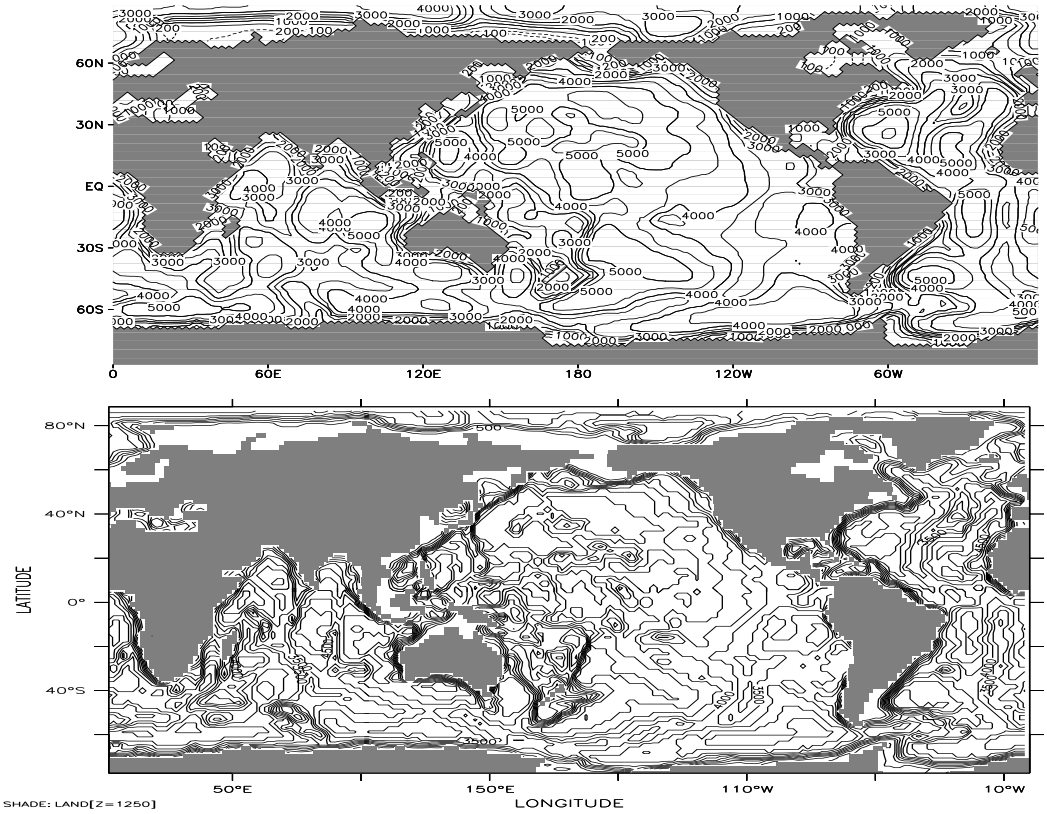

Figure 7.1: Topography of scalar points for HOPE (upper panel) and MOM2 (lower panel).

with d_i being the thickness of layer i. The pressure p_n is calculated from the depth z_n according to p_n[in bar] $= 0.1026 \cdot z_n$ [in meter]. Potential temperature is transformed into in-situ temperature by accounting for the pressure effect after Bryden (1973). In-situ density ρ_n is calculated from in-situ temperature by using the Standard UNESCO formula (Gill, 1982).

Starting at the top layer and going downward, those in-situ densities ρ_{k-1} and ρ_k, $(1 \leq k \leq N)$ are determined for which the following conditions are valid:

$$\rho_{k-1} \leq \rho_{mld} \leq \rho_k \text{ with } \rho_{mld} = \rho_1 + \rho_{crit},$$

using a critical value $\rho_{crit} = 0.125$ kg/m^3. For the mixed layer depth z_{mld}, similar conditions as for ρ_{mld} in (7.1) are valid,

$$z_{k-1} \leq z_{mld} \leq z_k$$

where z_{mld} is calculated by linear interpolation,

$$z_{mld} = z_{k-1} + (z_k - z_{k-1}) \cdot \frac{\rho_{mld} - \rho_{k-1}}{\rho_k - \rho_{k-1}}.$$

Sverdrup transport

An important aspect of the models' behavior is the simulation of the water transport, represented by the barotropic streamfunction. This quantity can be compared locally with observations in

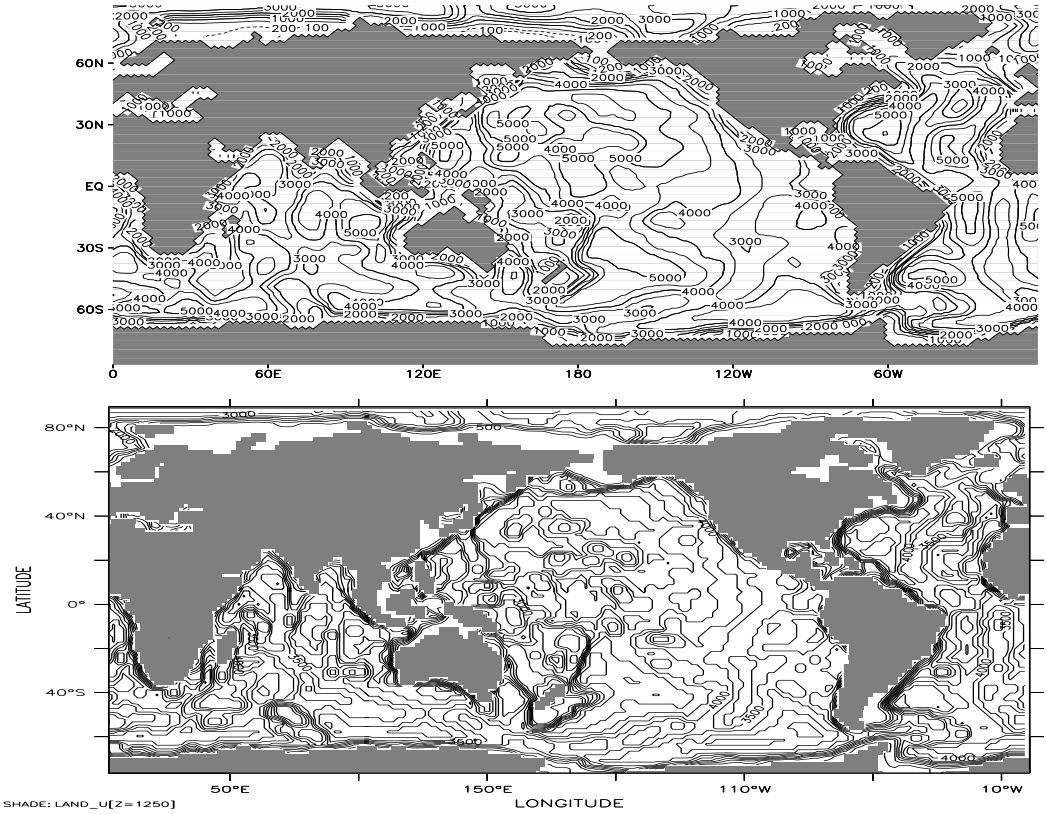

Figure 7.2: Topography of vector points for HOPE (upper panel) and MOM2 (lower panel).

selected oceanic regions, e.g. in the western boundary currents. For a comparison on the global scale, the steady-state response of the ocean to the wind stress $\boldsymbol{\tau}$ is calculated by using Sverdrup's equation. A stream function ψ_{Sver} is obtained by integrating the curl of $\boldsymbol{\tau}$ westward from the eastern boundary (Gill, 1982):

$$\psi_{Sver}(\lambda,\phi) = \int_{\text{eastern boundary}}^{\lambda} \frac{\boldsymbol{k}\cdot\boldsymbol{\nabla}\times\boldsymbol{\tau}(\lambda',\phi)}{R\rho_0\beta}d\lambda' \tag{7.1}$$

with $\beta = 2\Omega\cos\phi/R, \Omega = 7.292\cdot10^{-5}s^{-1}, R = 6.371\cdot10^6$ m, and $\rho_0 = 1025$ kg/m^3. The Sverdrup stream function is thus not defined where eastern boundaries are absent, in particular in the circumpolar region around Antarctica.

7.2 The barotropic circulation

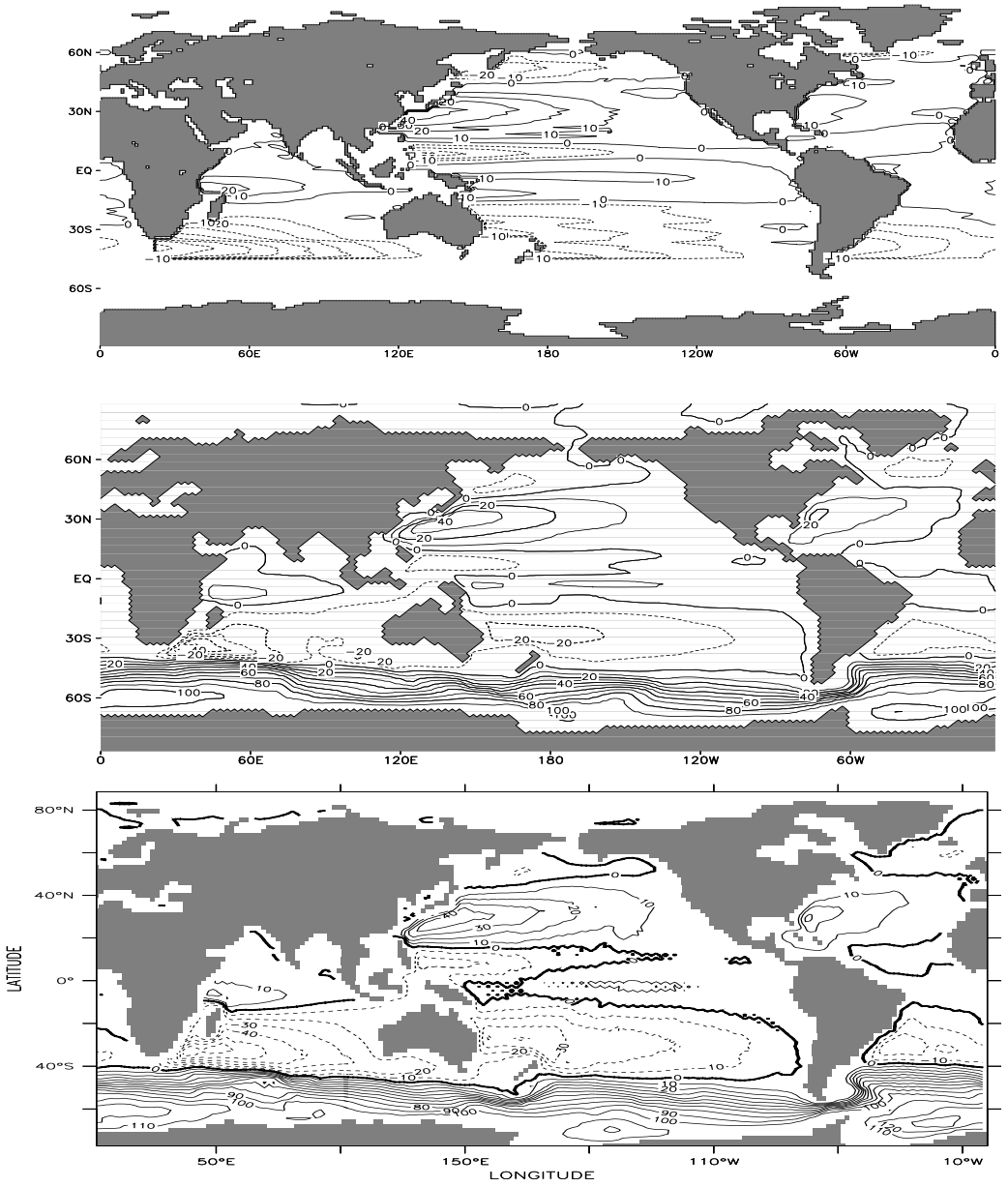

Figure 7.3: Barotropic streamfunction flat bottom Sverdrup transport (upper panel), barotropic streamfunction of HOPE (middle panel) and MOM2 (lower panel) Units Sv.

7.3 Major current systems, transports

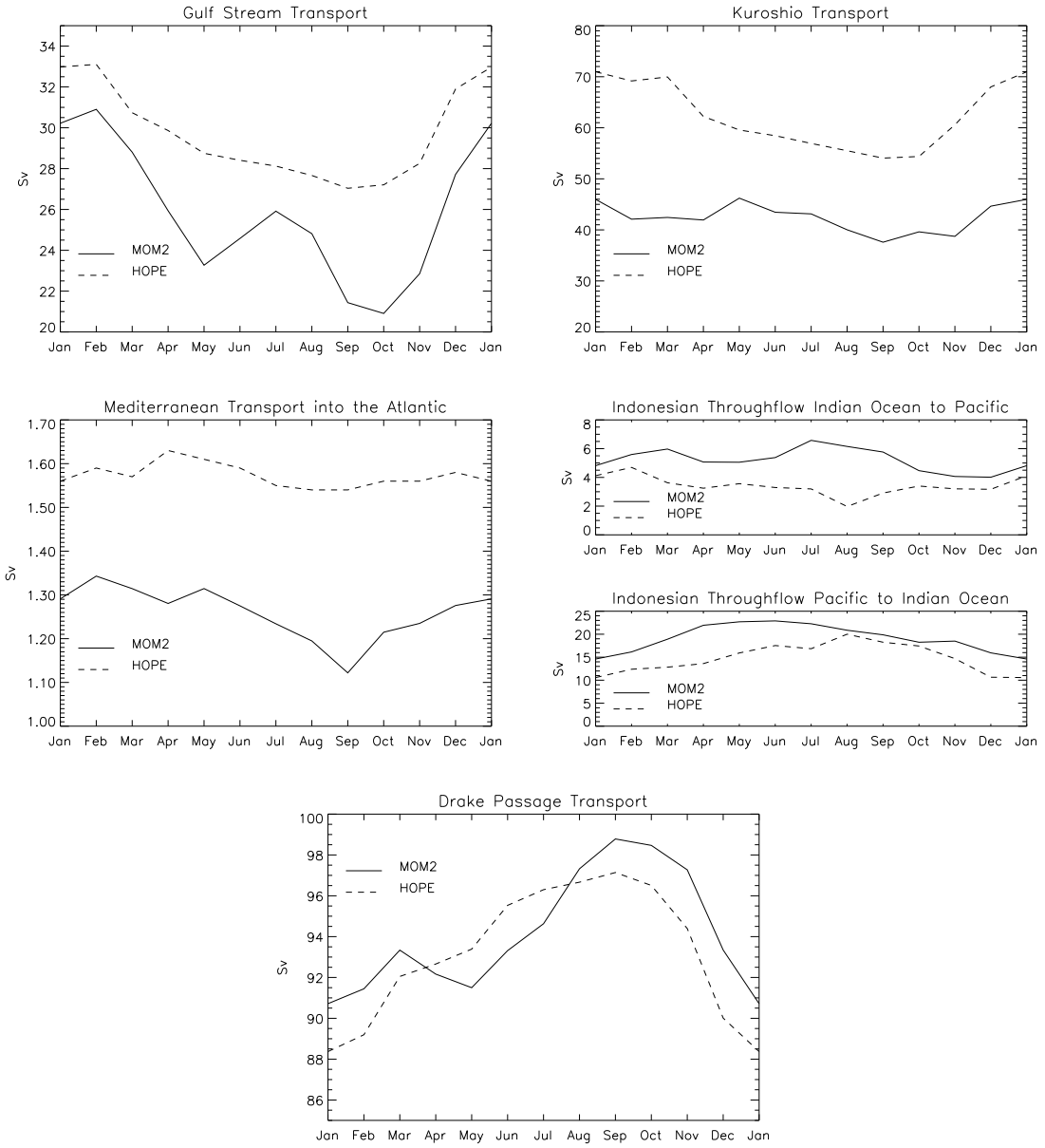

Figure 7.4:
Transports of Gulf stream, Kuroshio, Mediterranean into Atlantic, Indonesian throughflow and Drake passage.

Region	Volume transports (Sv)	References
Florida Current	30.5	Molinari et al. 1985
	31.7 ± 3.0	Leaman et al. 1987
	30.5 ± 3.0	Schott et al. 1988
Kuroshio Current	57-72	Taft 1978
	57	Niiler et al. 1985
	81	Teague et al. 1994
	62	Ichikawa et al. 1998
Drake Passage	127 ± 14	Fandry and Pillsbury 1979
	118-146	Whitworth 1983
	123 ± 10.5	Whitworth and Peterson 1984
Mediterranean Outflow	0.4-0.7	Baringer and Price 1997
	0.84 ± 0.3	Hopkins 1999
Indonesian Throughflow	10	Macdonald 1993
	9.8, [0.5 (I->P)-18.1 (P->I)]	Inoue and Welsh 1993
	18.6 ± 7 (P->I)	Fieux et al. 1994
	1.5 - 20	Murray and Arief 1988
	6 (I->P), 20 (P->I)	Muneyama et al. 1994
Frame strait ice export	0.159 [0.09-0.19]	Vinje and Finnekasa 1986
	0.177	Koerner 1973
	0.165	Ostlund and Hut 1984

Table 7.2: Volume transports of major ocean current systems, according to observations.

7.4 The meridional overturning

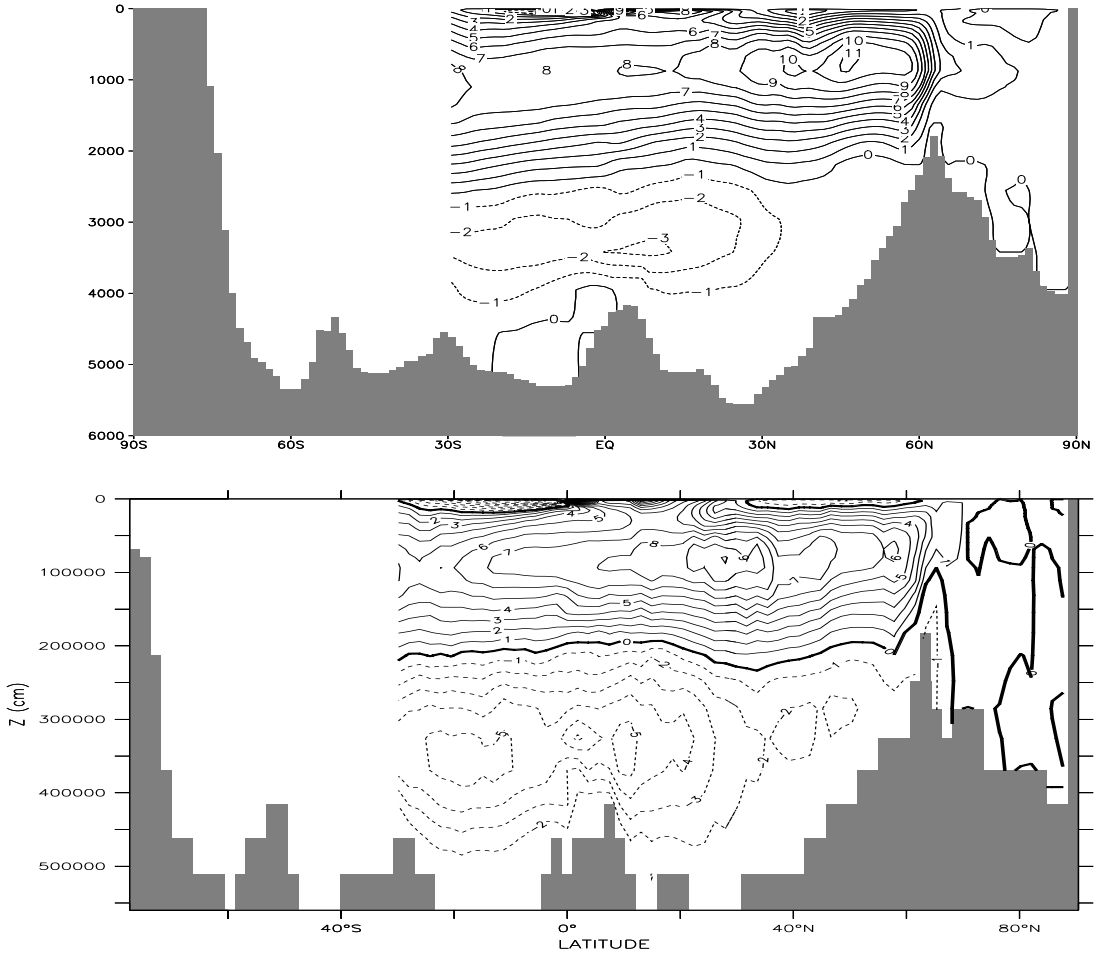

Figure 7.5: Streamfunction of the meridional overturning in the Atlantic for HOPE (upper panel) and MOM2 (lower panel) Units Sv.

7.5 Surface fluxes and upper ocean properties

Data set	All O.	Arc.	Atl.	N.A.	S.A.	Pac.	N.P.	S.P.	Ind.	N.I.	S.I.
ECH4	-0.4	-13.4	4.5	-8.2	16.7	-1.0	-6.0	2.8	-2.3	11.5	-5.4
CO88	2.9	-67.1	0.7	-11.5	19.5	2.3	-4.5	10.3	11.0	45.2	-0.3
CO94	28.2	-33.4	27.9	17.4	38.0	29.0	25.3	31.9	37.4	83.1	27.3
CO97	30.0	-70.3	28.0	20.8	35.6	32.4	33.8	31.4	29.7	68.9	20.3
NRA	3.4	-11.8	3.6	-11.4	18.0	6.2	1.0	10.3	-1.8	9.5	-4.3
ERA	0.7	-11.6	-1.5	-14.0	10.4	4.3	3.1	5.1	-4.0	15.9	-8.4
OMIP	-0.1	-5.0	-2.2	-15.1	10.2	2.2	0.2	3.6	-3.2	27.6	-10.0
MOM2	0.4	-10.9	1.5	-4.4	6.8	2.3	3.7	1.3	-8.5	28.6	-15.6
HOPE	1.2	-7.8	1.6	-3.7	7.1	4.8	0.5	8.0	-7.6	12.6	-12.0

Table 7.3: Net downward heat flux (Units Wm^{-2}).

Data set	All O.	Arc.	Atl.	N.A.	S.A.	Pac.	N.P.	S.P.	Ind.	N.I.	S.I.
ECH4	-7.6	17.1	-19.6	-19.0	-20.2	-0.4	7.6	-6.6	-14.5	-23.5	-12.5
CO88	3.4	11.3	-25.0	-17.2	-37.1	24.3	31.0	16.2	-16.5	5.4	-23.8
CO94	2.8	55.4	-13.6	-20.9	-6.5	5.0	0.0	8.9	10.9	-15.0	16.6
CO97	-6.2	8.1	-21.7	-14.6	-29.3	6.1	13.8	-0.2	-19.3	-36.4	-15.2
NRA	-7.9	9.6	-21.3	-22.7	-20.0	0.6	5.4	-3.1	-15.1	-17.5	-14.5
ERA	-8.0	11.5	-24.7	-20.4	-28.9	4.7	21.7	-8.3	-22.5	-9.9	-25.3
OMIP	-9.7	16.1	-25.8	-22.6	-28.8	1.8	17.8	-10.5	-23.4	-9.3	-26.5

Table 7.4: Net downward fresh water flux (Units mm/month).

Data set	All O.	Arc.	Atl.	N.A.	S.A.	Pac.	N.P.	S.P.	Ind.	N.I.	S.I.
ECH4	-1.2	36.4	-7.1	-1.1	-12.9	3.1	13.5	-5.0	-11.3	-15.1	-10.5
OMIP	-0.3	54.8	-8.1	2.1	-17.9	5.9	24.0	-8.1	-17.1	12.5	-23.6
MOM2	-0.6	-5.6	-7.5	0.3	-14.5	3.6	10.9	-2.1	-7.1	3.9	-9.2
HOPE	-1.4	6.8	-7.5	-1.7	-13.4	3.3	10.4	-2.2	-7.5	7.1	-10.6

Table 7.5: Net downward fresh water flux with runoff (Units mm/month). Ocean models also with effects of salinity relaxation and ice growth.

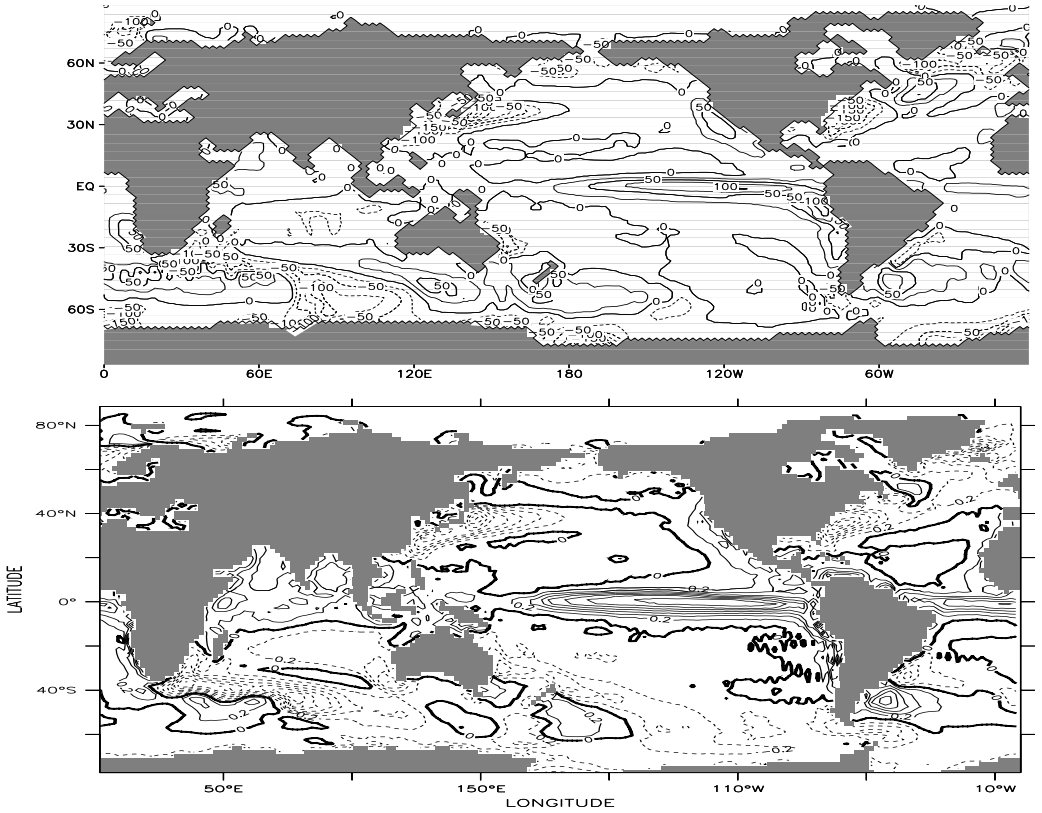

Figure 7.6: Net downward heat flux for HOPE (upper panel) and MOM2 (lower panel). Units Wm^{-2}.

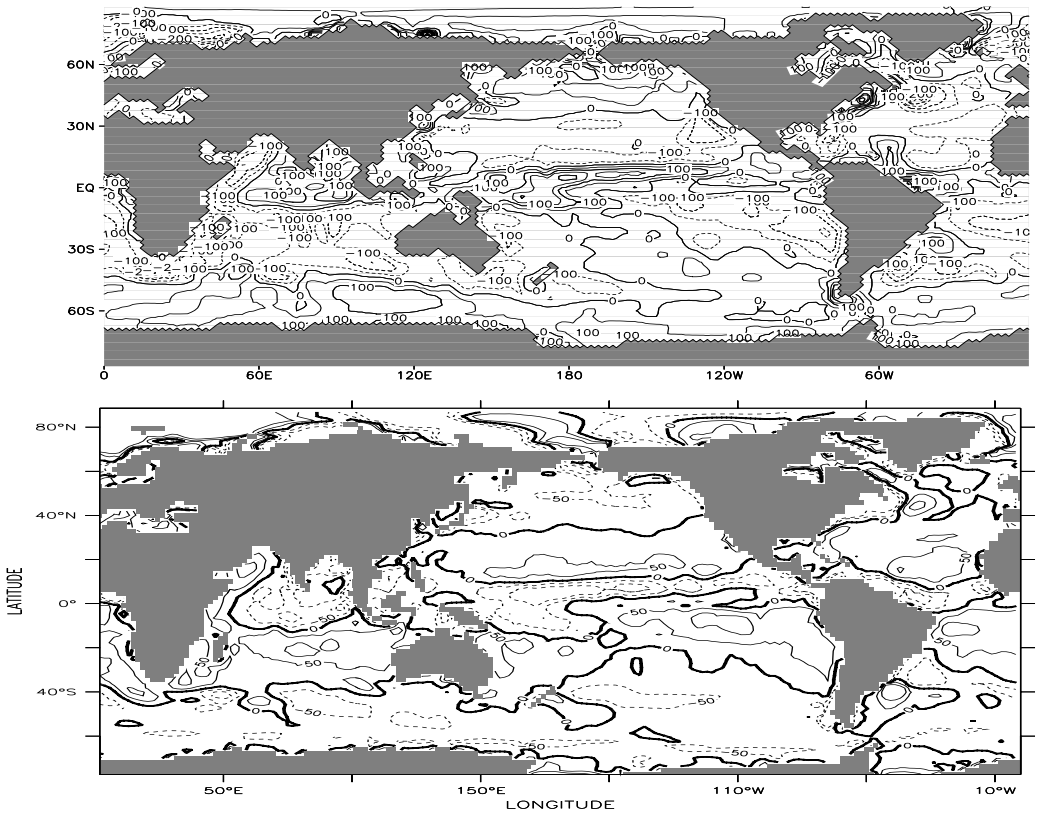

Figure 7.7: Net fresh water flux for HOPE (upper panel) and MOM2 (lower panel). Units mm/month.

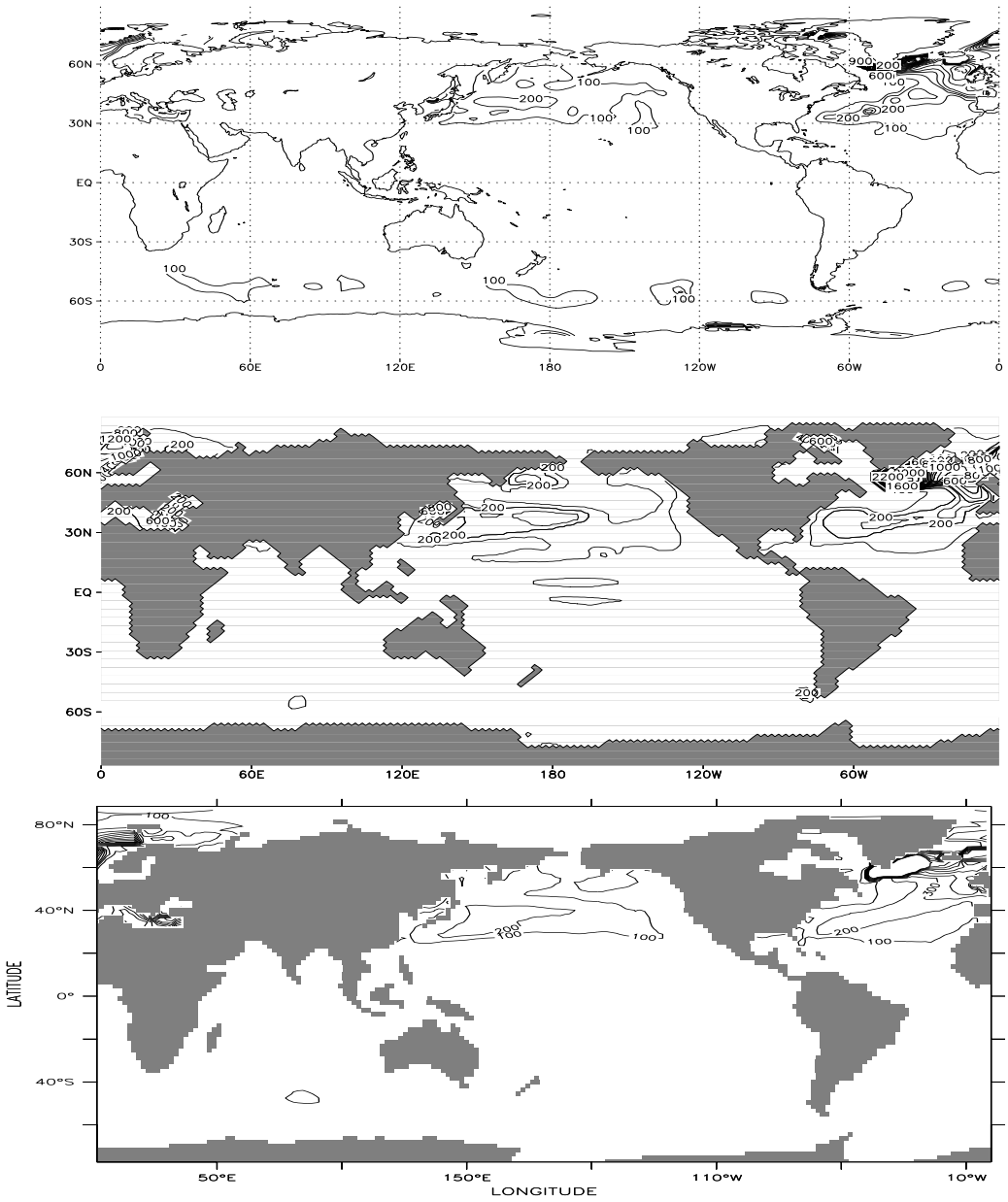

Figure 7.8: Mixed layer depth in March from Levitus (upper panel), for HOPE (middle panel) and MOM2 (lower panel). Units m.

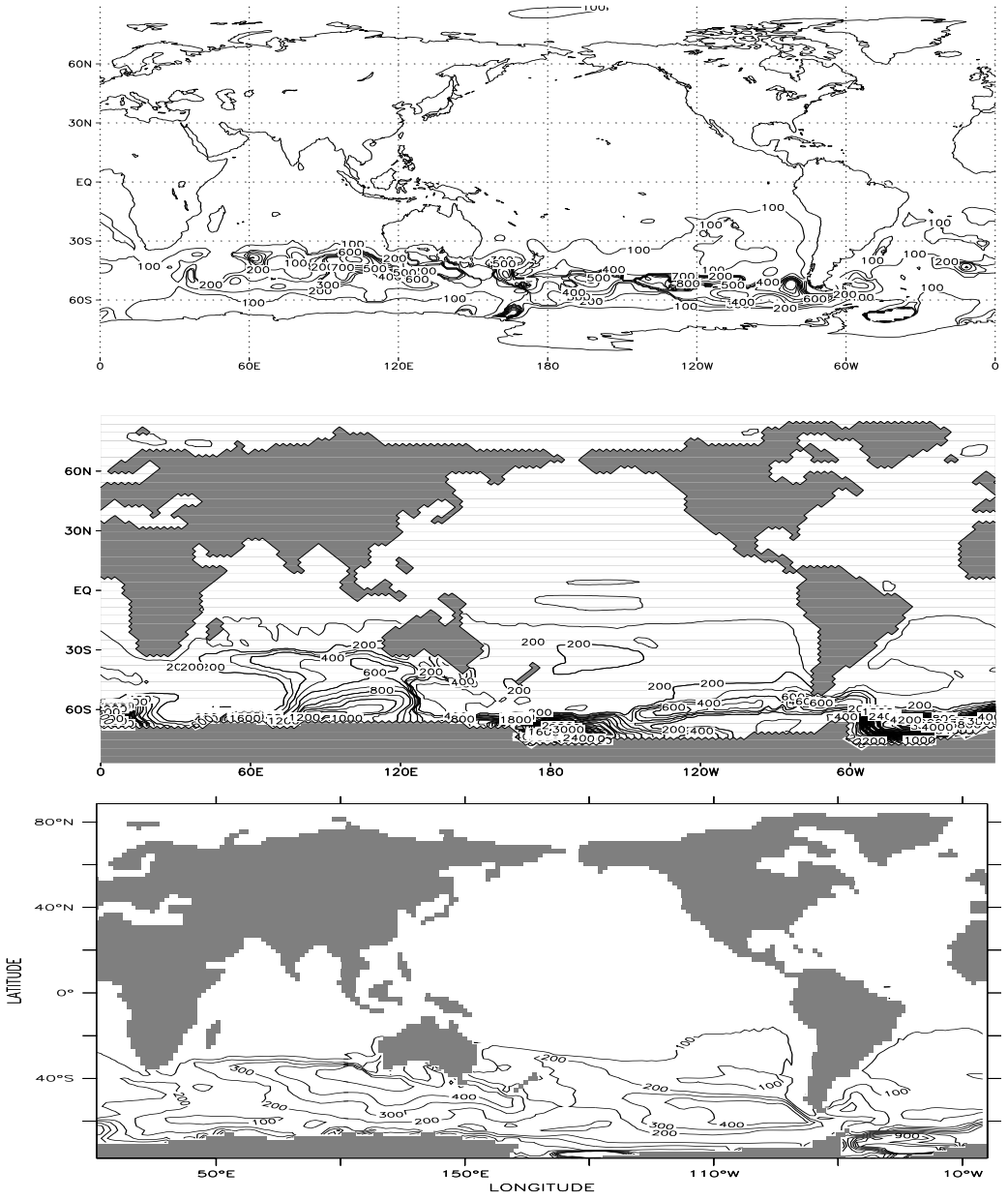

Figure 7.9: Mixed layer depth in September from Levitus (upper panel), for HOPE (middle panel) and MOM2 (lower panel). Units m.

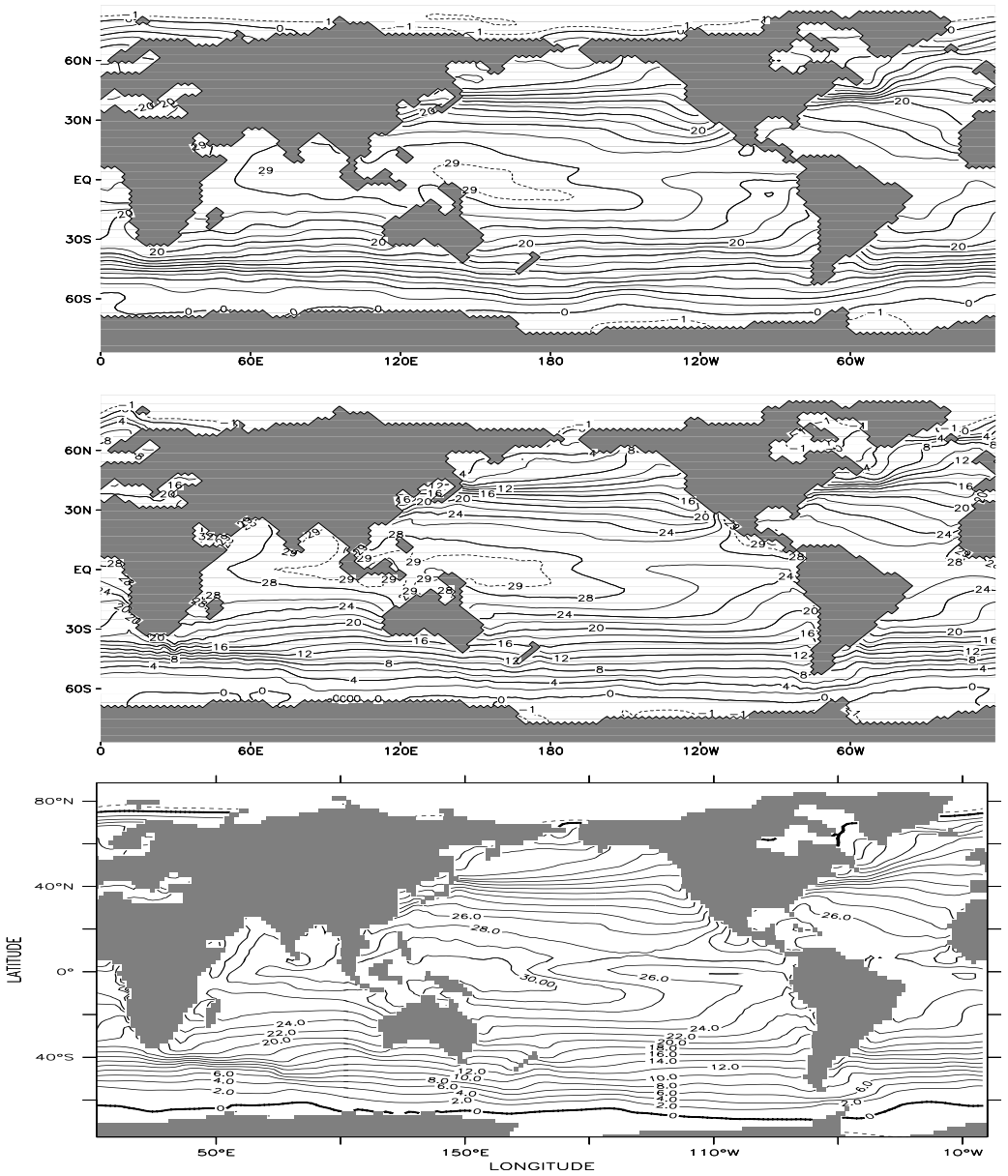

Figure 7.10: Temperature of top layer for Levitus (upper panel), HOPE (middle panel) and MOM2 (lower panel). Units $^{\circ}C$.

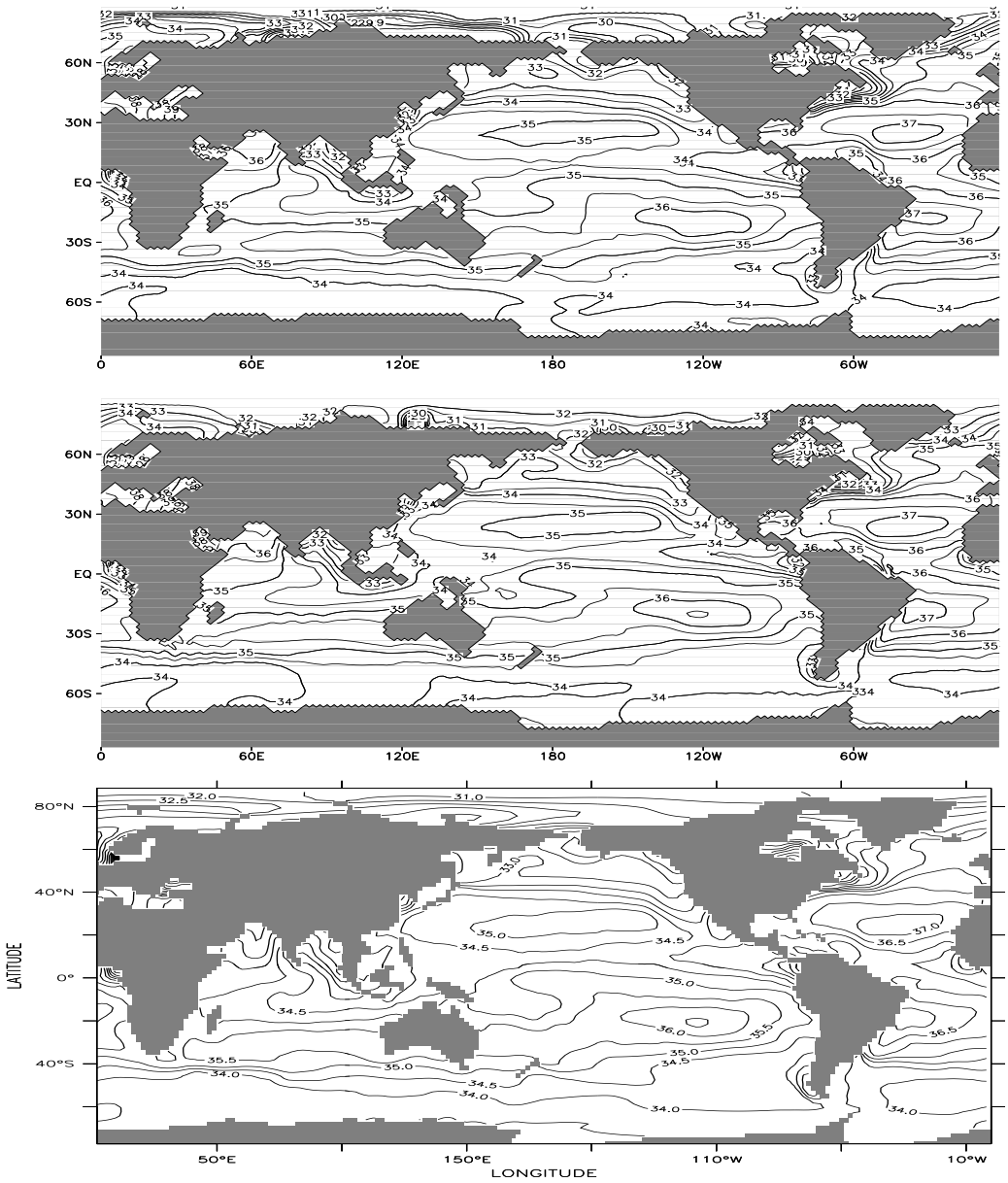

Figure 7.11: Salinity of top layer for Levitus (upper panel) HOPE (middle panel) and MOM2 (lower panel). Units psu.

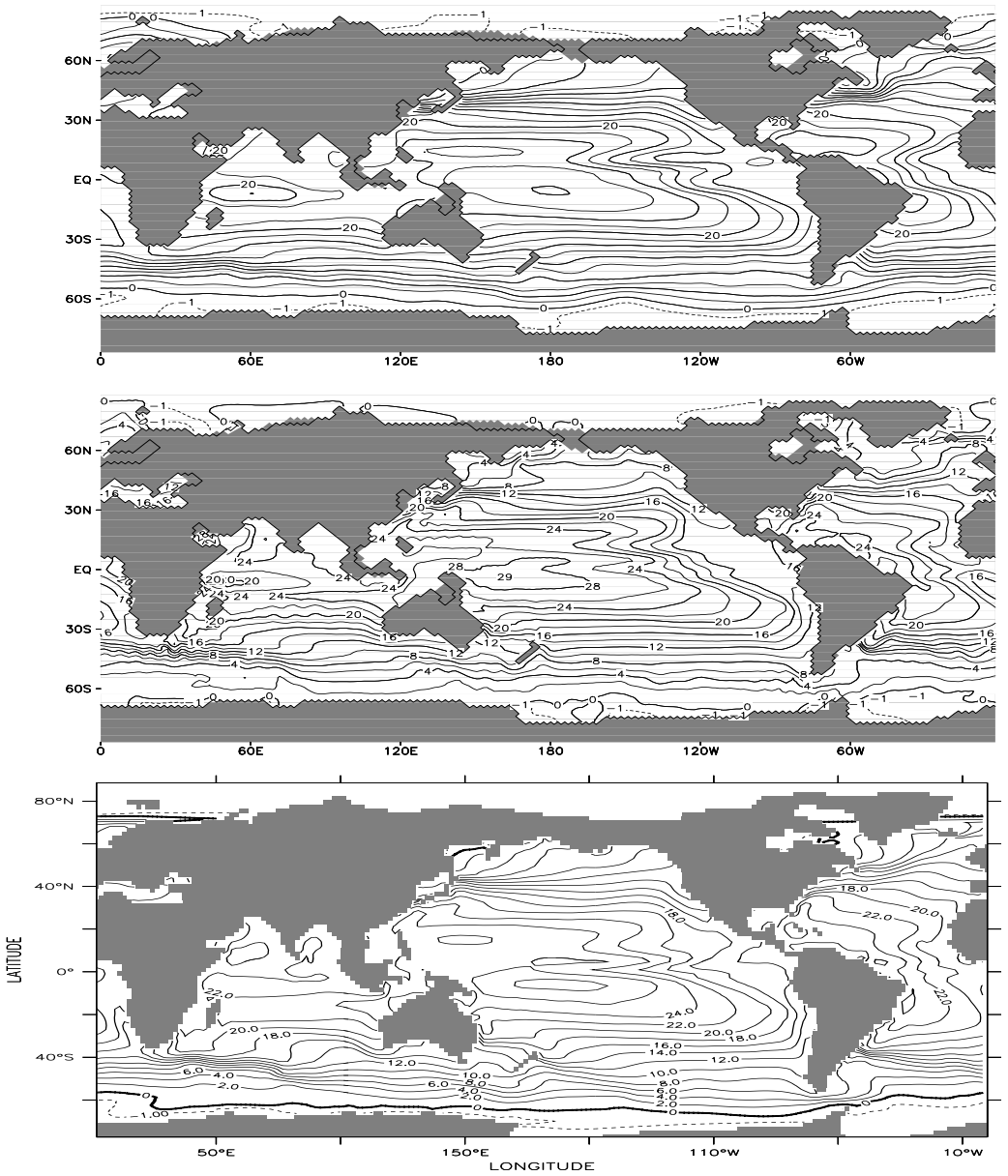

Figure 7.12: Temperature at 100m depth for Levitus (upper panel), HOPE (middle panel) and MOM2 (lower panel). Units $^{\circ}C$.

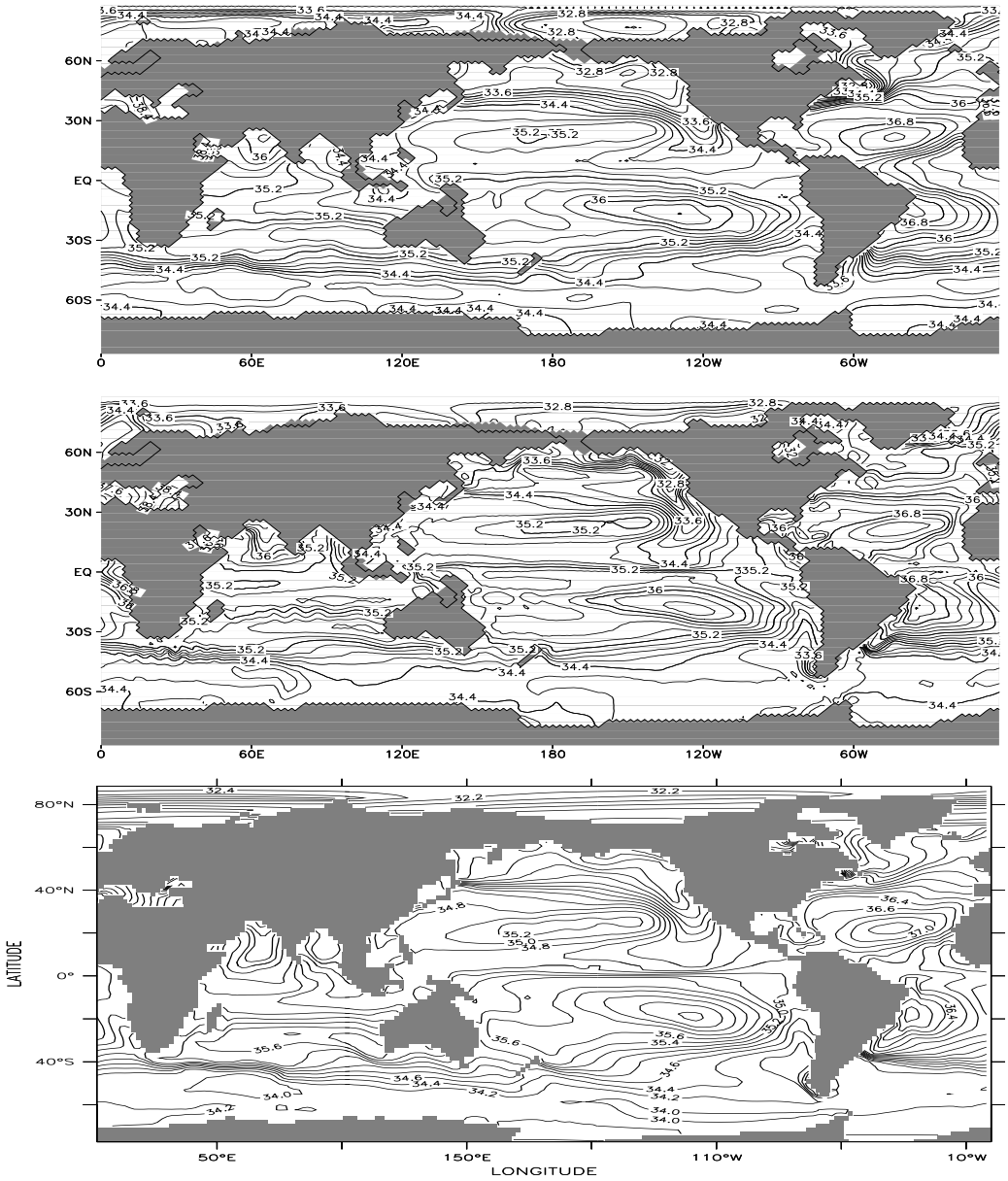

Figure 7.13: Salinity at 100m depth for Levitus (upper panel), HOPE (middle panel) and MOM2 (lower panel). Units psu.

7.6 The global mean stratification

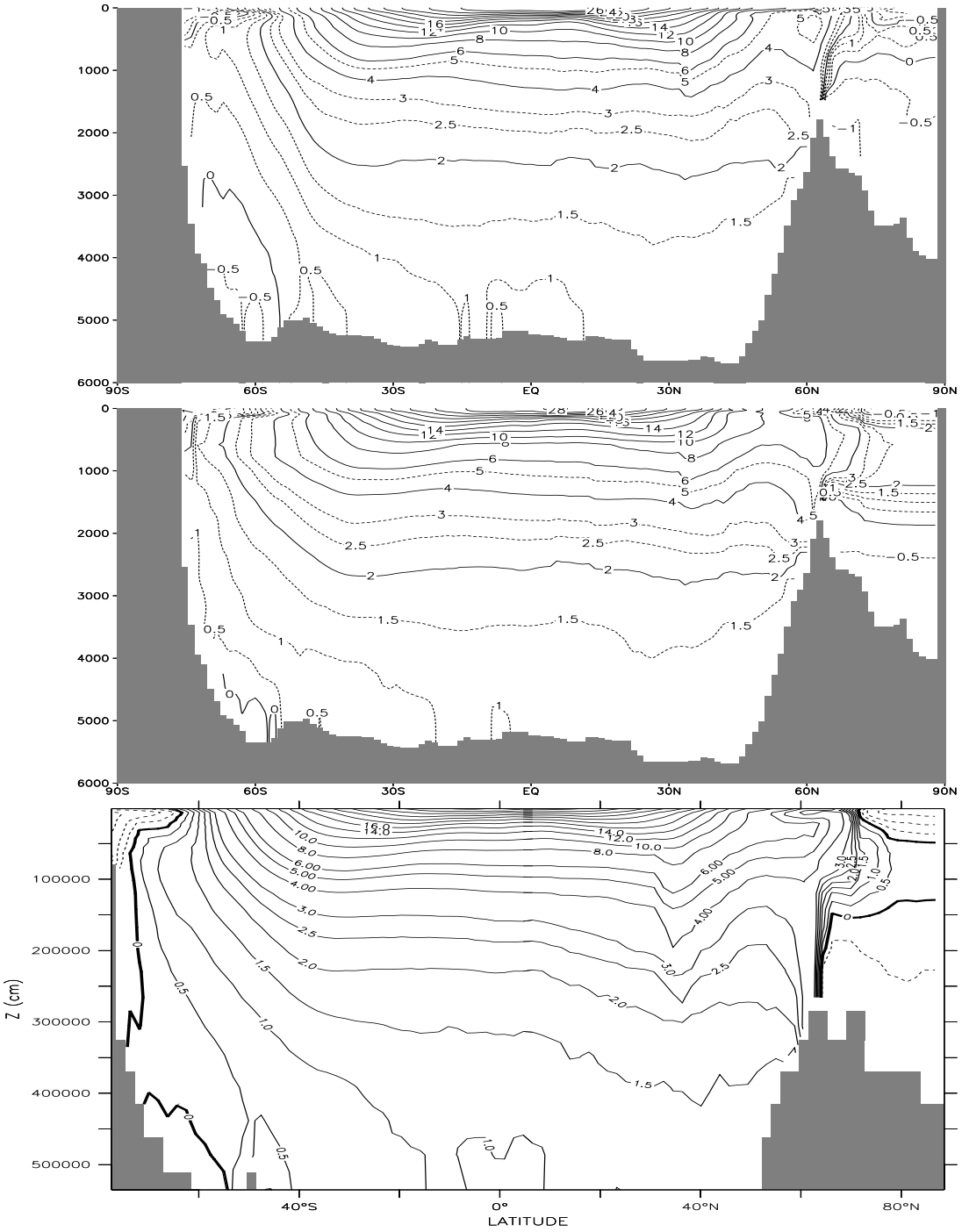

Figure 7.14: Zonally averaged temperature for all oceans for Levitus (upper panel), HOPE (middle panel) and MOM2 (lower panel). Units $^{\circ}C$.

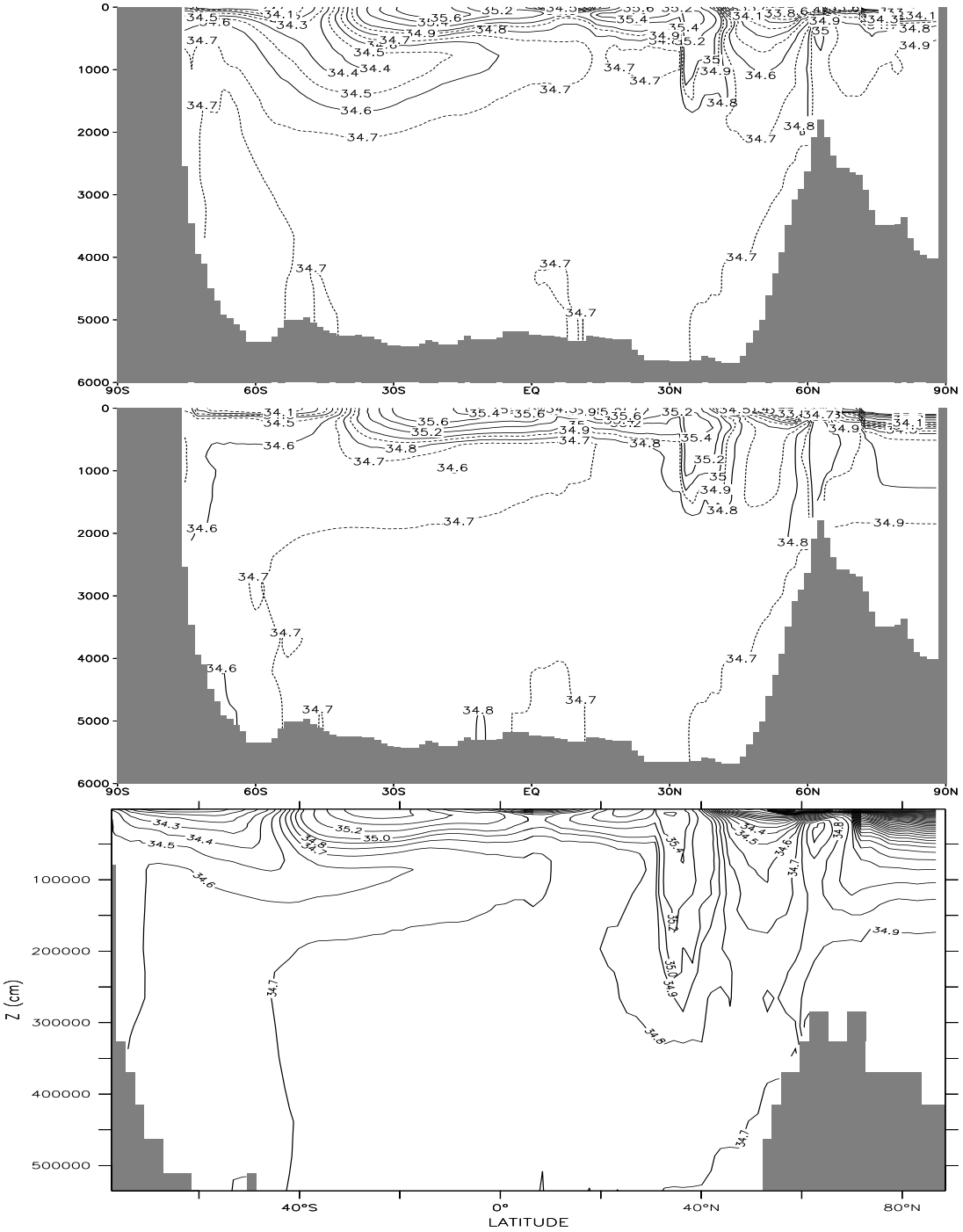

Figure 7.15: Zonally averaged salinity for all oceans for Levitus (upper panel), HOPE (middle panel) and MOM2 (lower panel). Units psu.

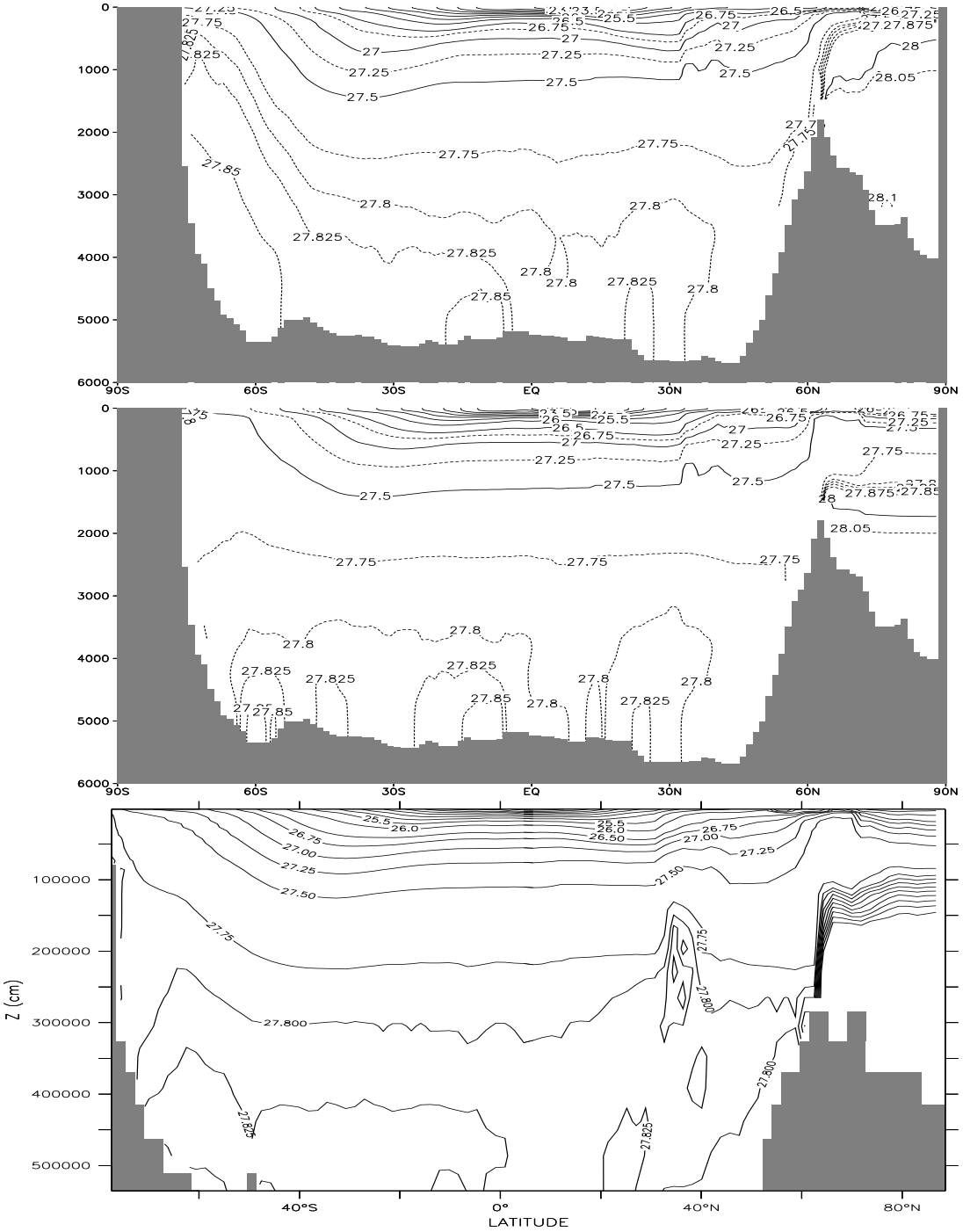

Figure 7.16: Zonally averaged density for all oceans for Levitus (upper panel), HOPE (middle panel) and MOM2 (lower panel). Units kgm^{-3} (-1000).

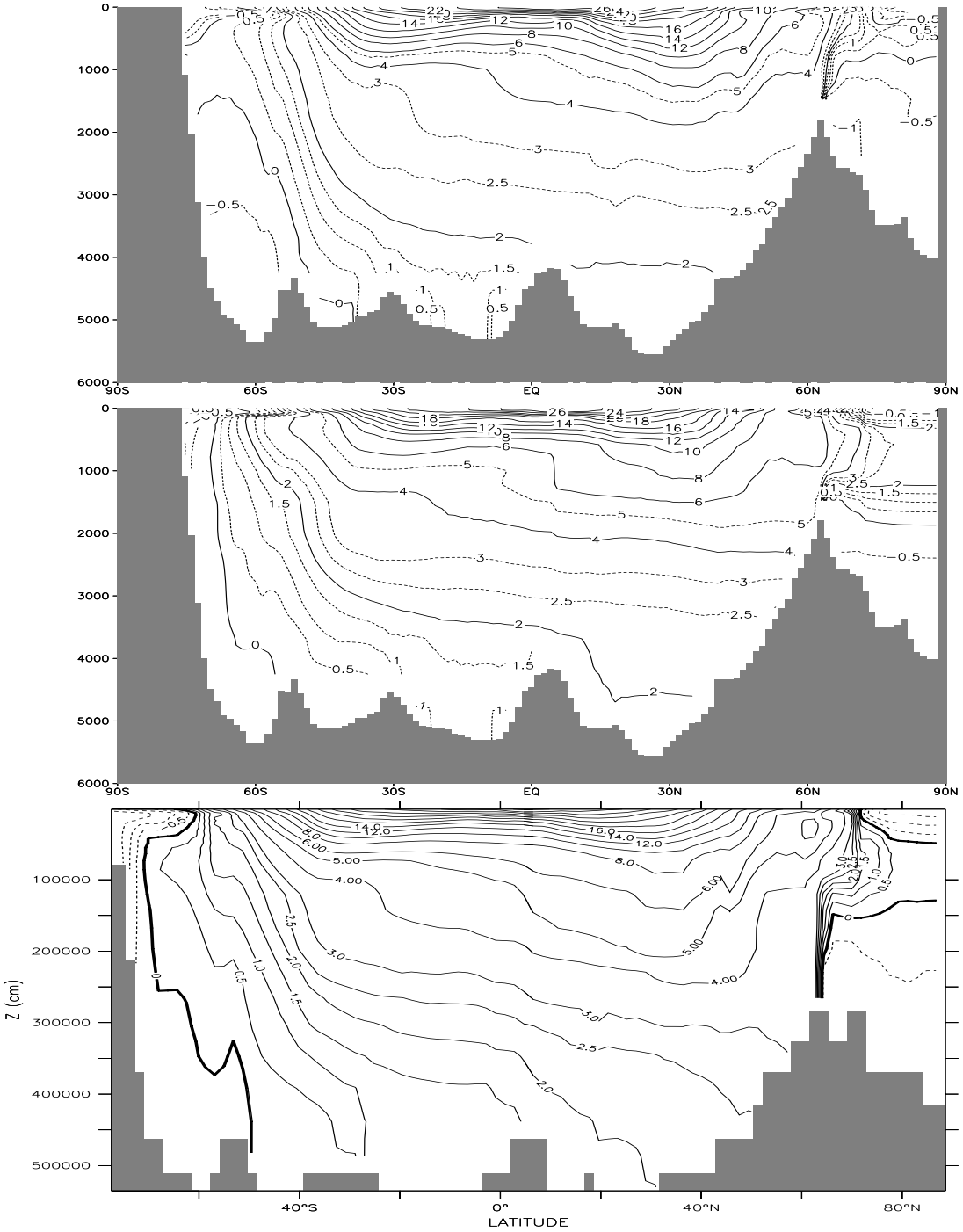

Figure 7.17: Zonally averaged temperature for the Atlantic for Levitus (upper panel), HOPE (middle panel) and MOM2 (lower panel). Units $^{\circ}C$.

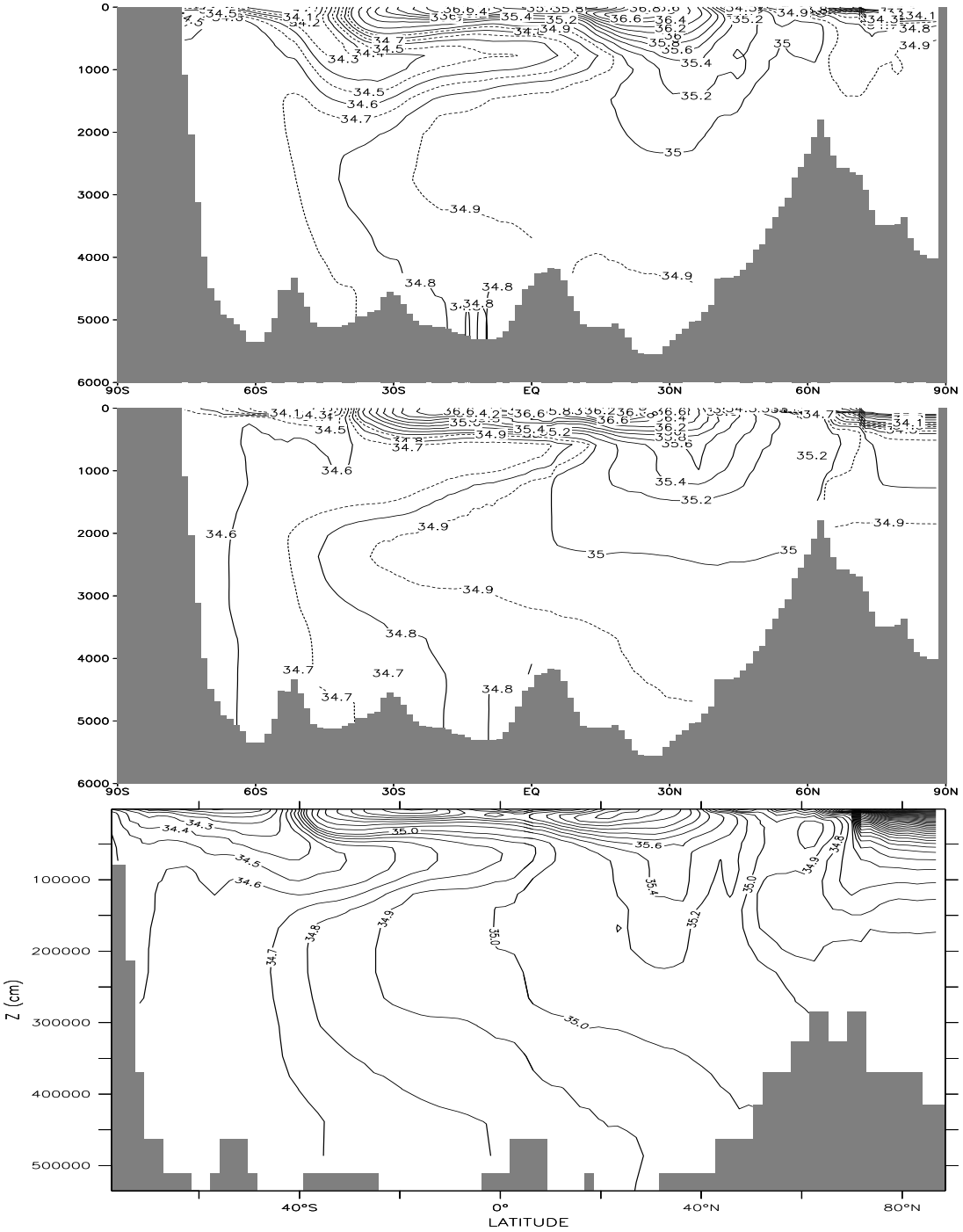

Figure 7.18: Zonally averaged salinity for the Atlantic for Levitus (upper panel), HOPE (middle panel) and MOM2 (lower panel). Units psu.

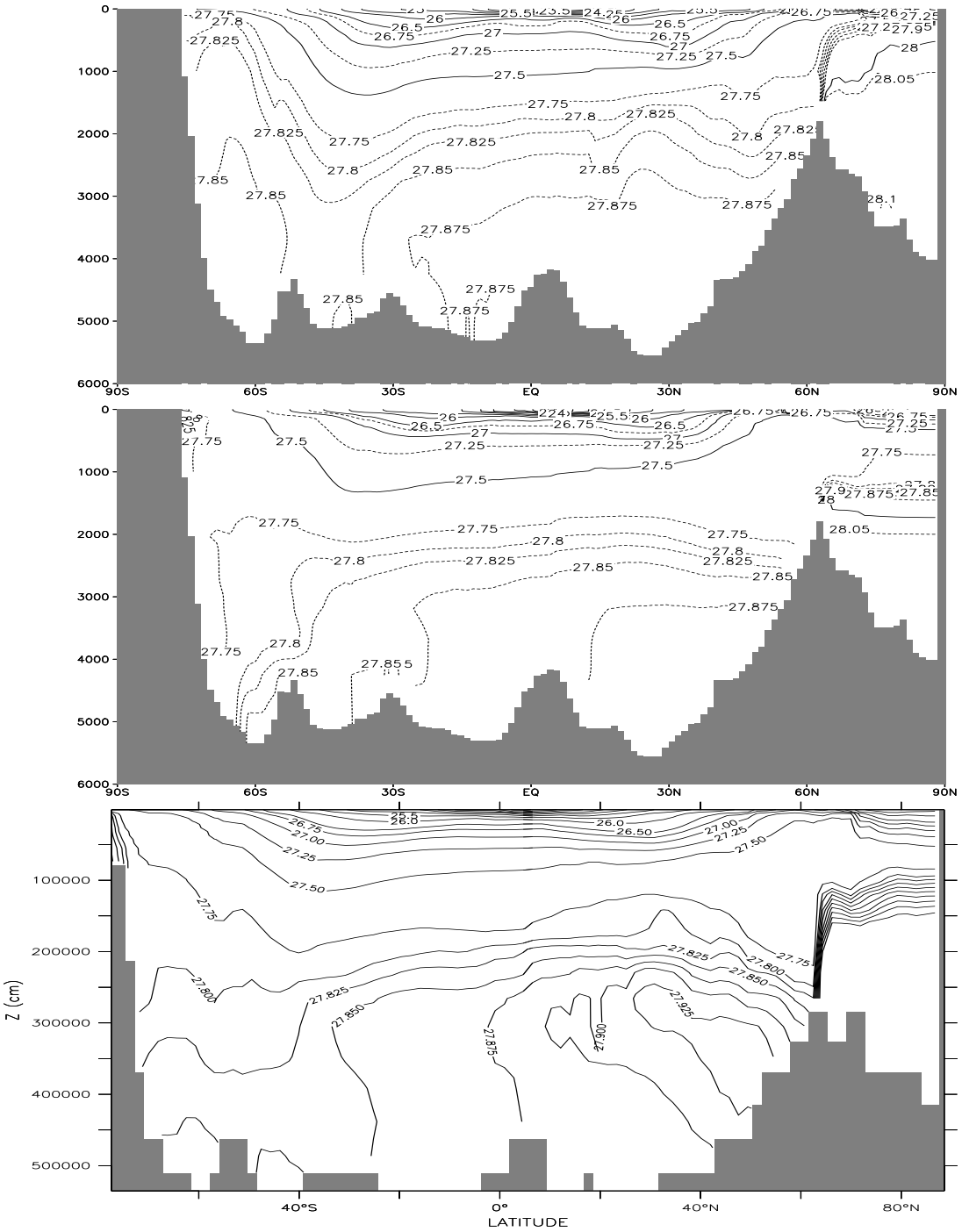

Figure 7.19: Zonally averaged density for the Atlantic for Levitus (upper panel), HOPE (middle panel) and MOM2 (lower panel). Units kgm^{-3} (-1000).

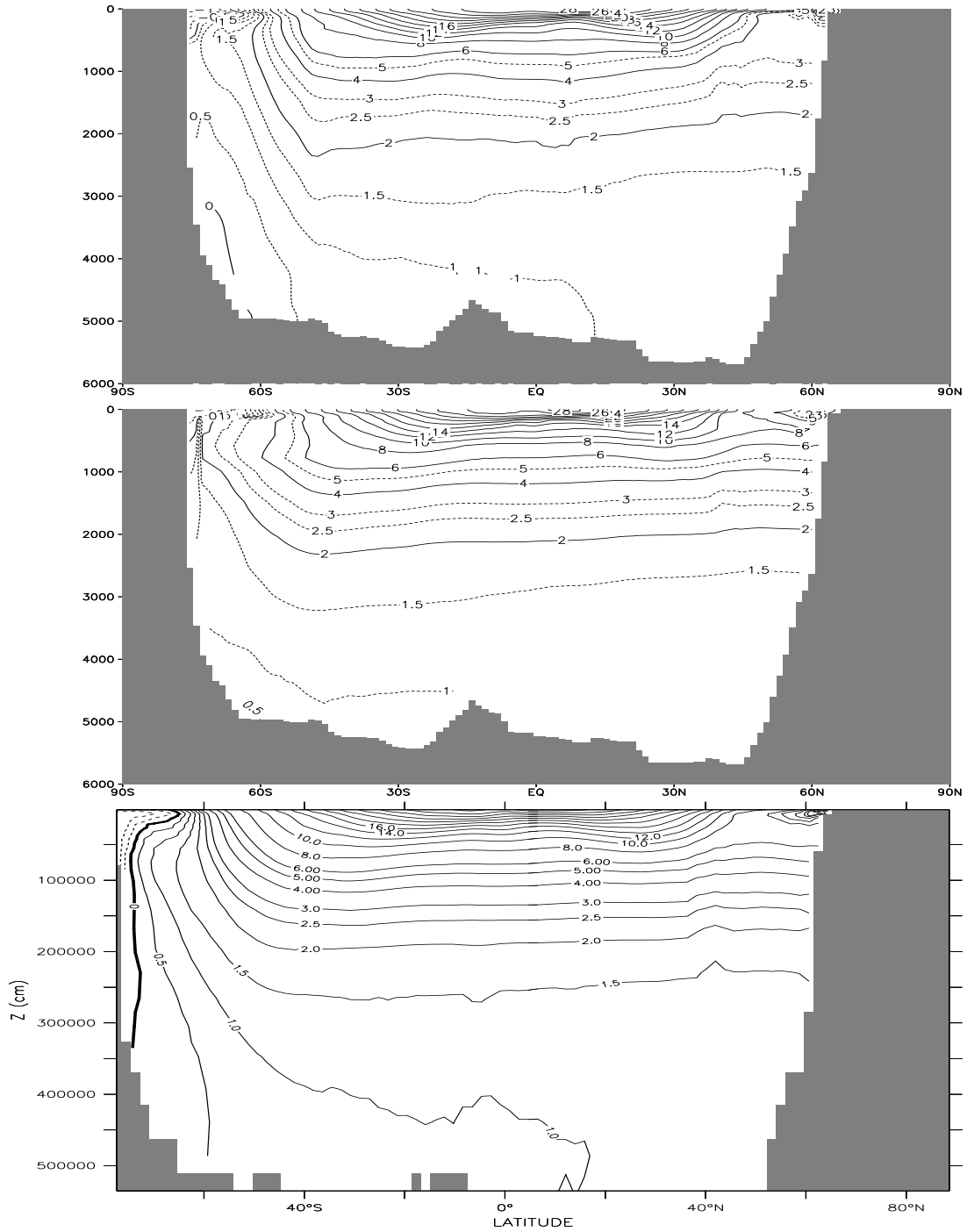

Figure 7.20: Zonally averaged temperature for the Pacific for Levitus (upper panel), HOPE (middle panel) and MOM2 (lower panel). Units $^{\circ}C$.

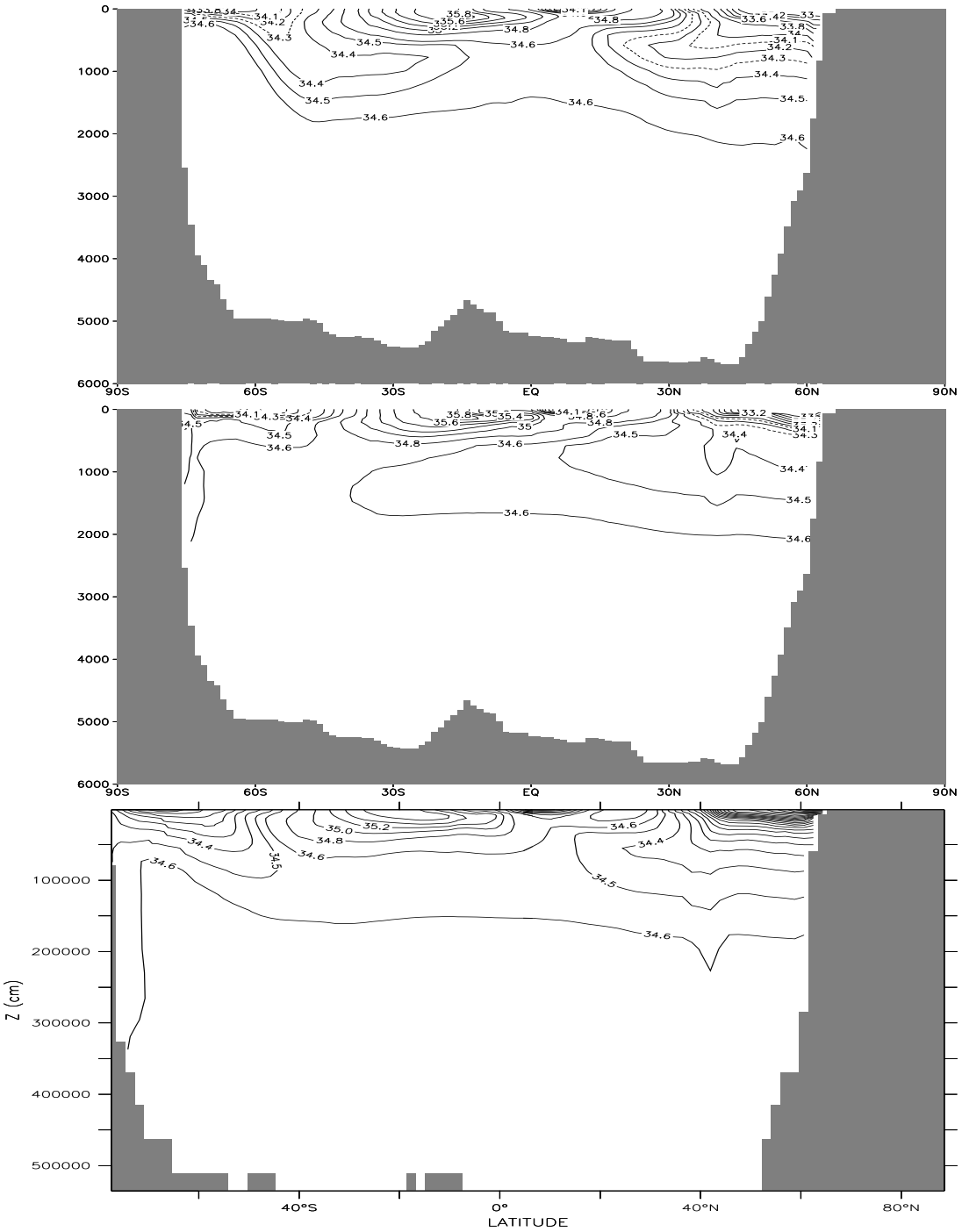

Figure 7.21: Zonally averaged salinity for the Pacific for Levitus (upper panel), HOPE (middle panel) and MOM2 (lower panel). Units psu.

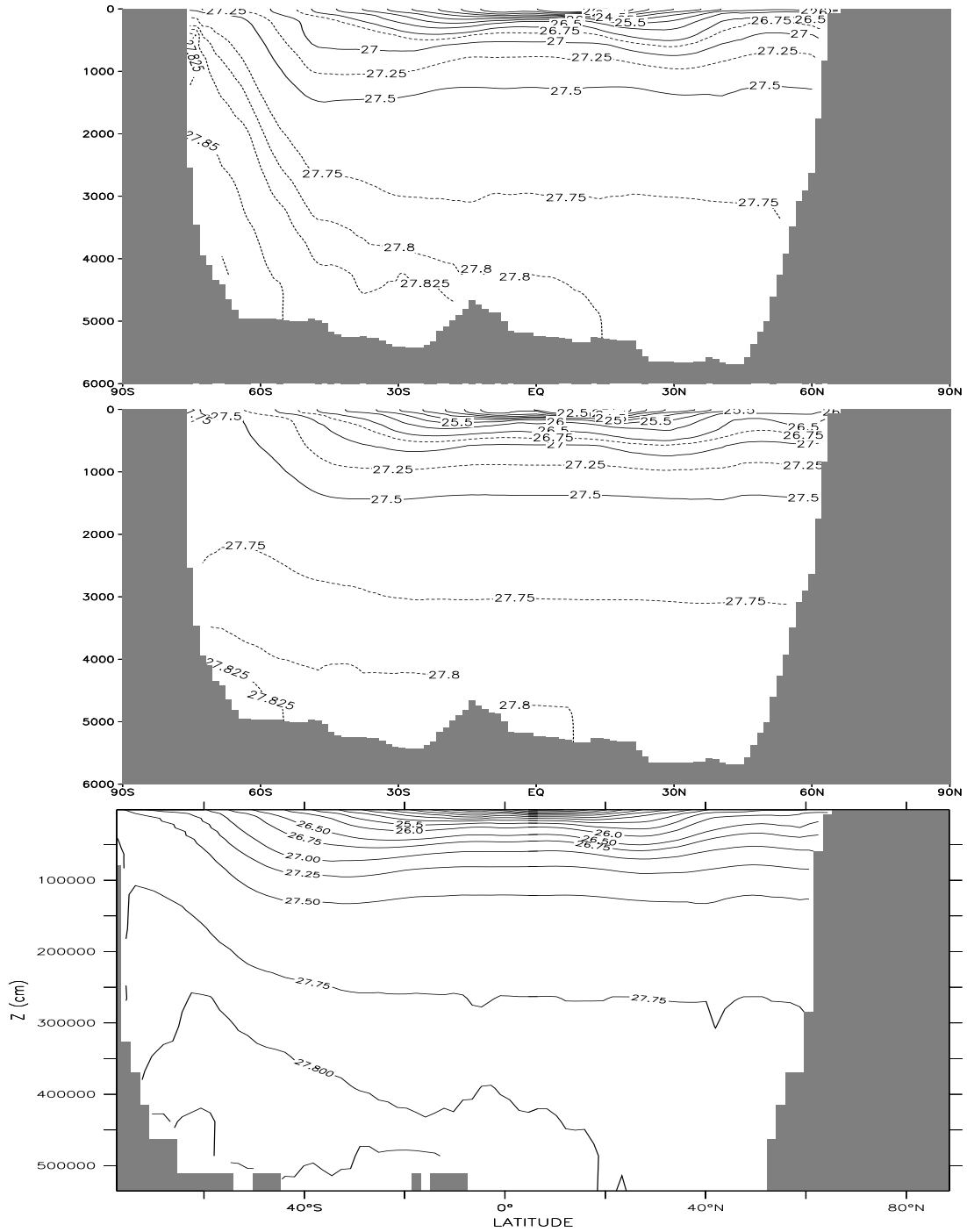

Figure 7.22: Zonally averaged density for the Pacific for Levitus (upper panel), HOPE (middle panel) and MOM2 (lower panel). Units kgm^{-3} (-1000).

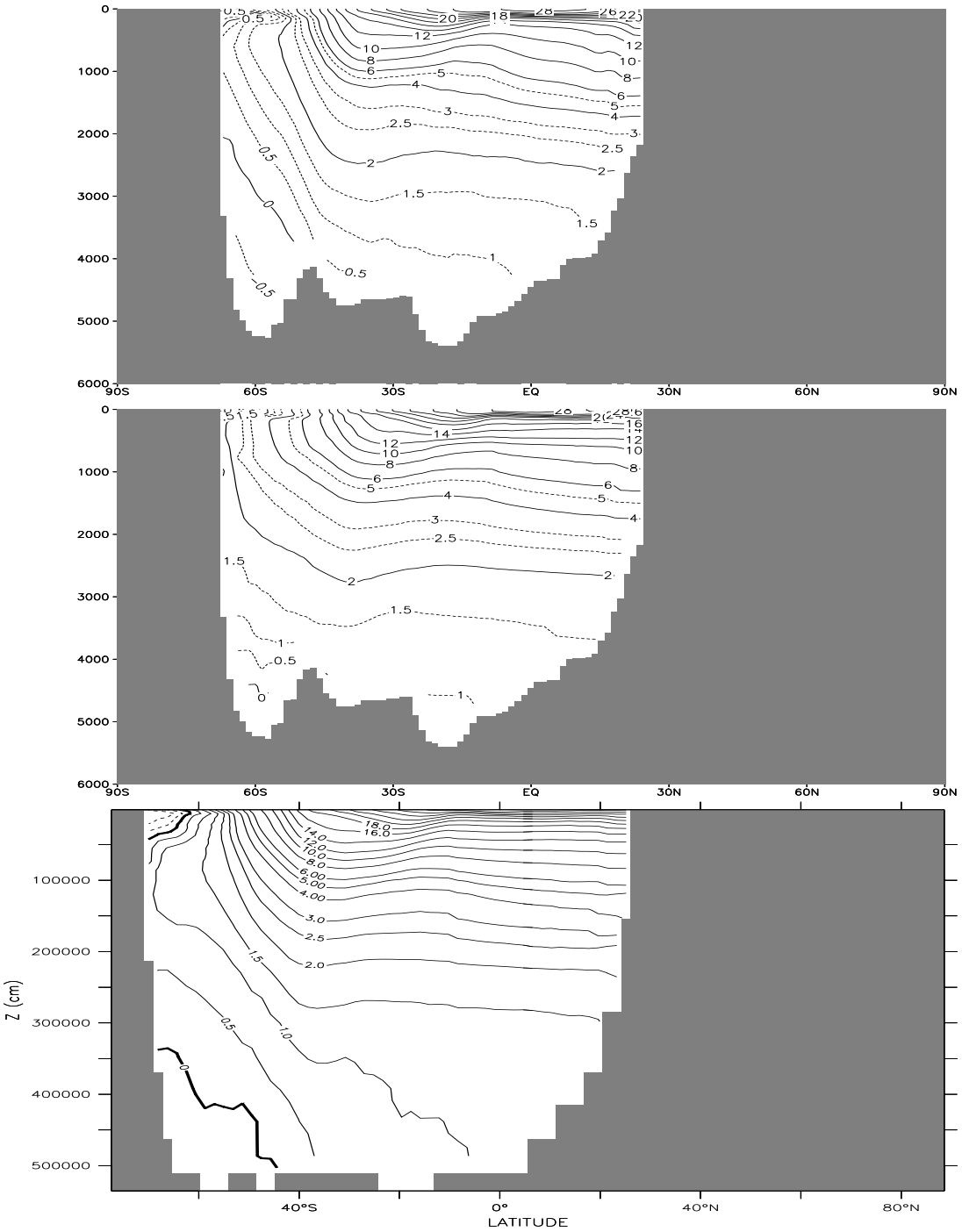

Figure 7.23: Zonally averaged temperature for the Indian Ocean for Levitus (upper panel), HOPE (middle panel) and MOM2 (lower panel). Units $^{\circ}C$.

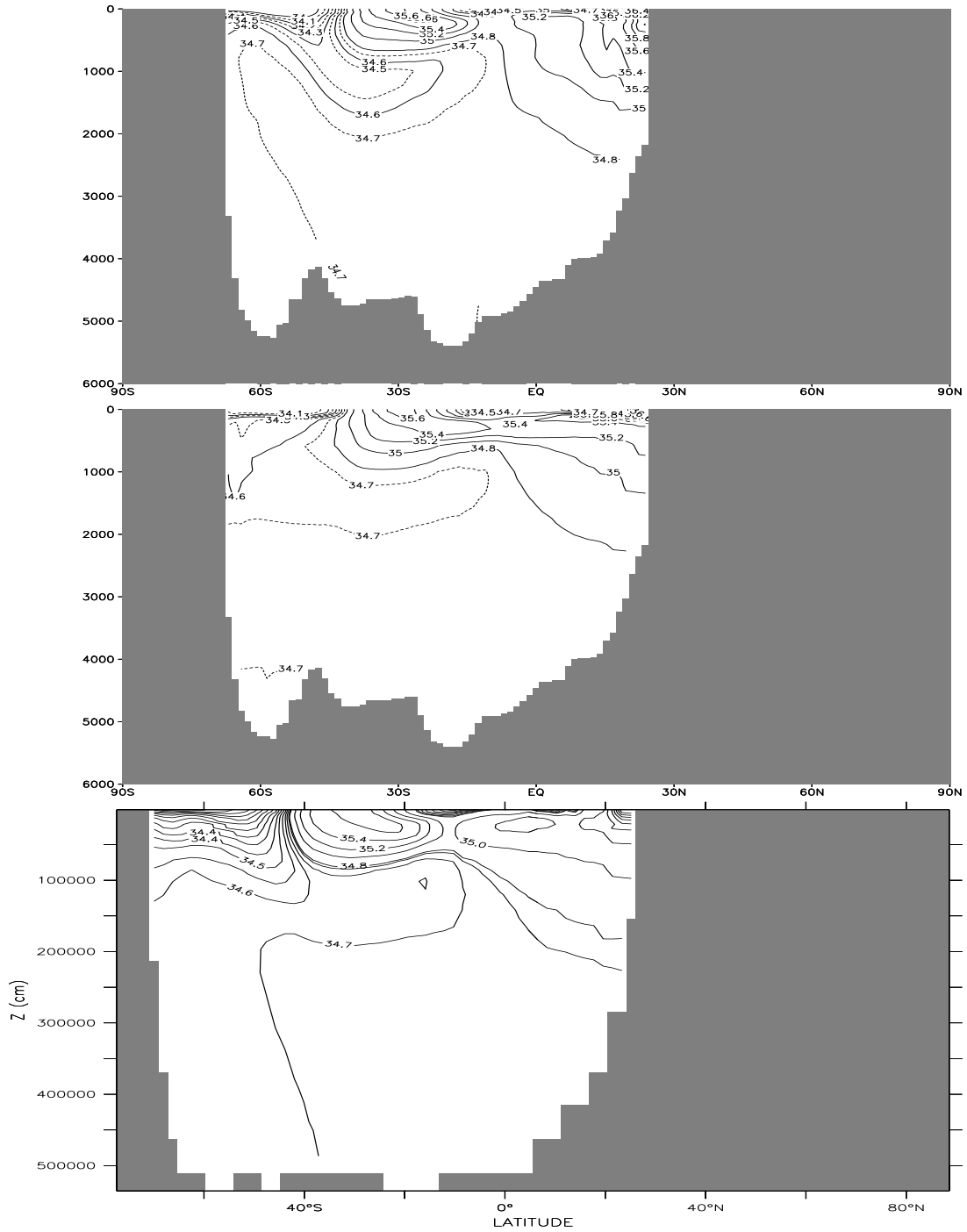

Figure 7.24: Zonally averaged salinity for the Indian Ocean for Levitus (upper panel), HOPE (middle panel) and MOM2 (lower panel). Units psu.

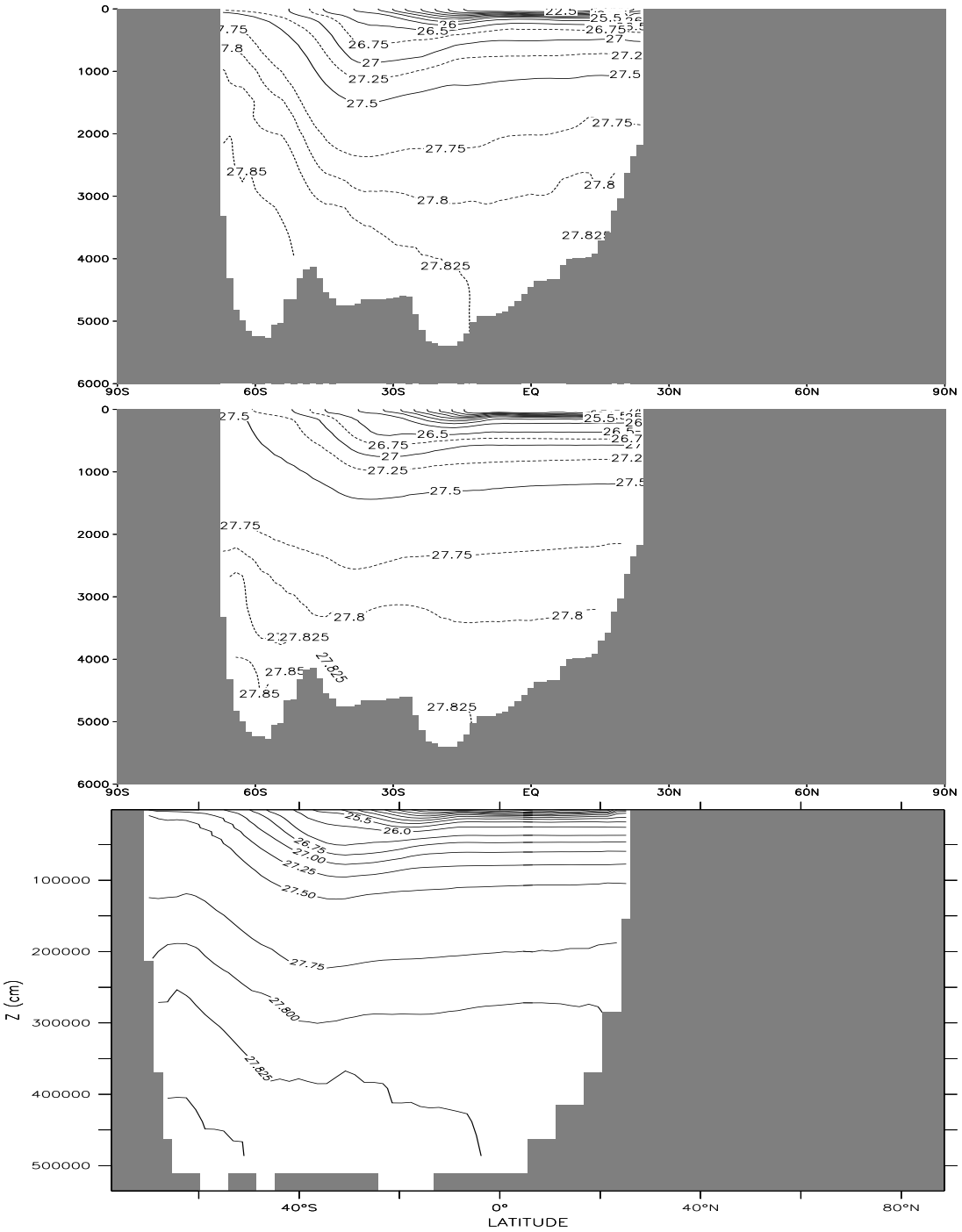

Figure 7.25: Zonally averaged density for the Indian Ocean for Levitus (upper panel), HOPE (middle panel) and MOM2 (lower panel). Units kgm^{-3} (-1000).

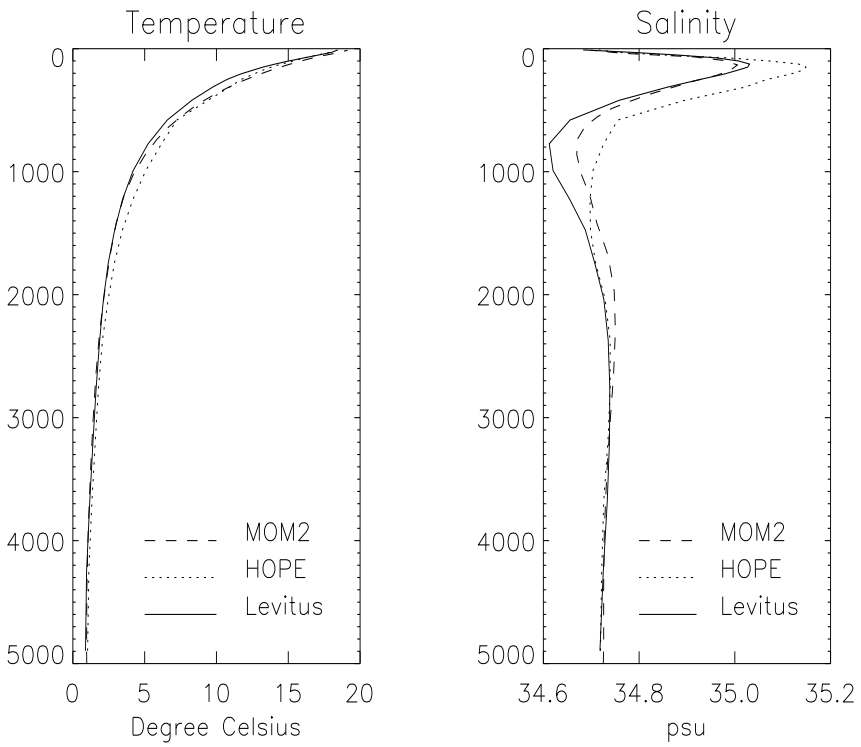

Figure 7.26: Mean profiles of temperature and salinity for Levitus, HOPE and MOM2.

7.7 The near surface circulation

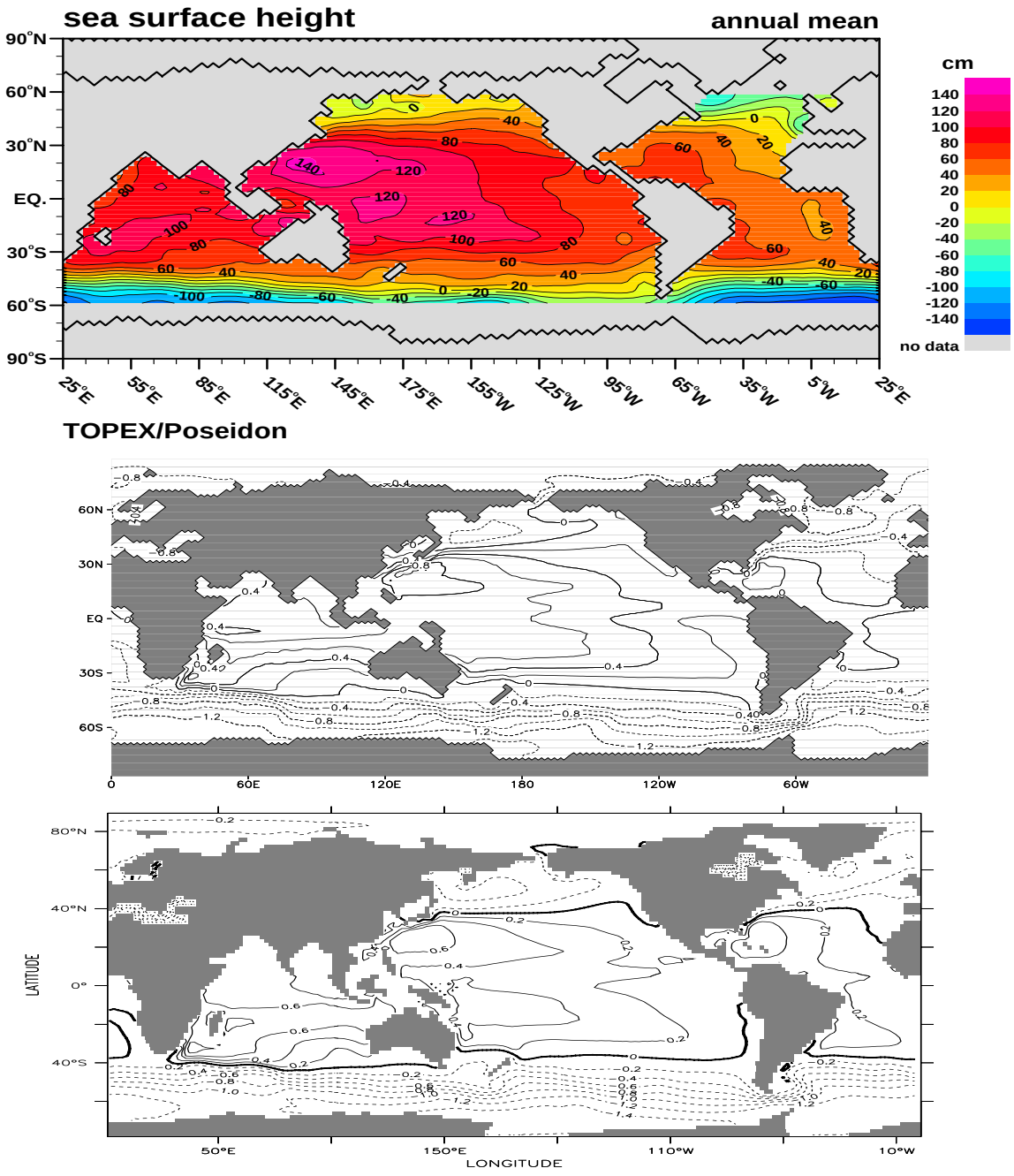

Figure 7.27: Sea surface elevation from TOPEX-POSEIDON and for HOPE (upper panel) and MOM2 (lower panel). Units cm and m, respectively.

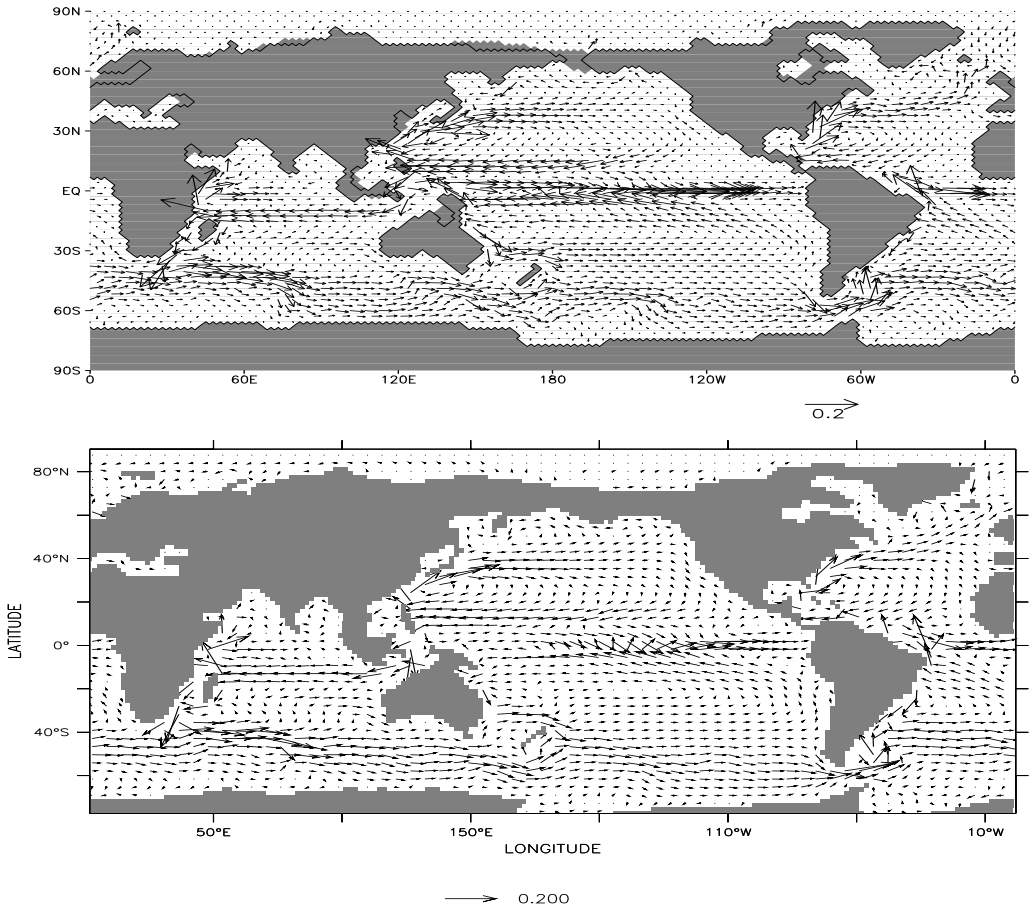

Figure 7.28: Horizontal velocity at 100 m depth for HOPE (upper panel) and MOM2 (lower panel). The arrows are 0.2 m/s.

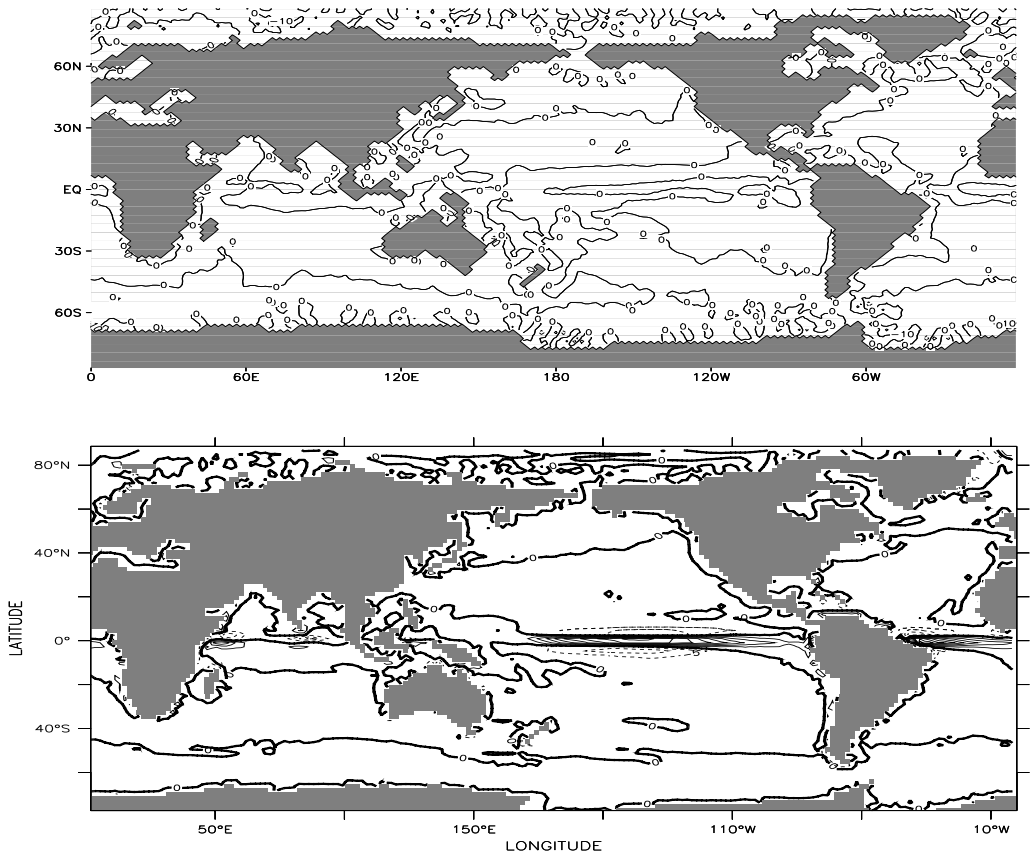

Figure 7.29: Vertical velocity at top for HOPE (upper panel) and MOM2 (lower panel). Units are $10^{-6}\mathrm{ms}^{-1}$.

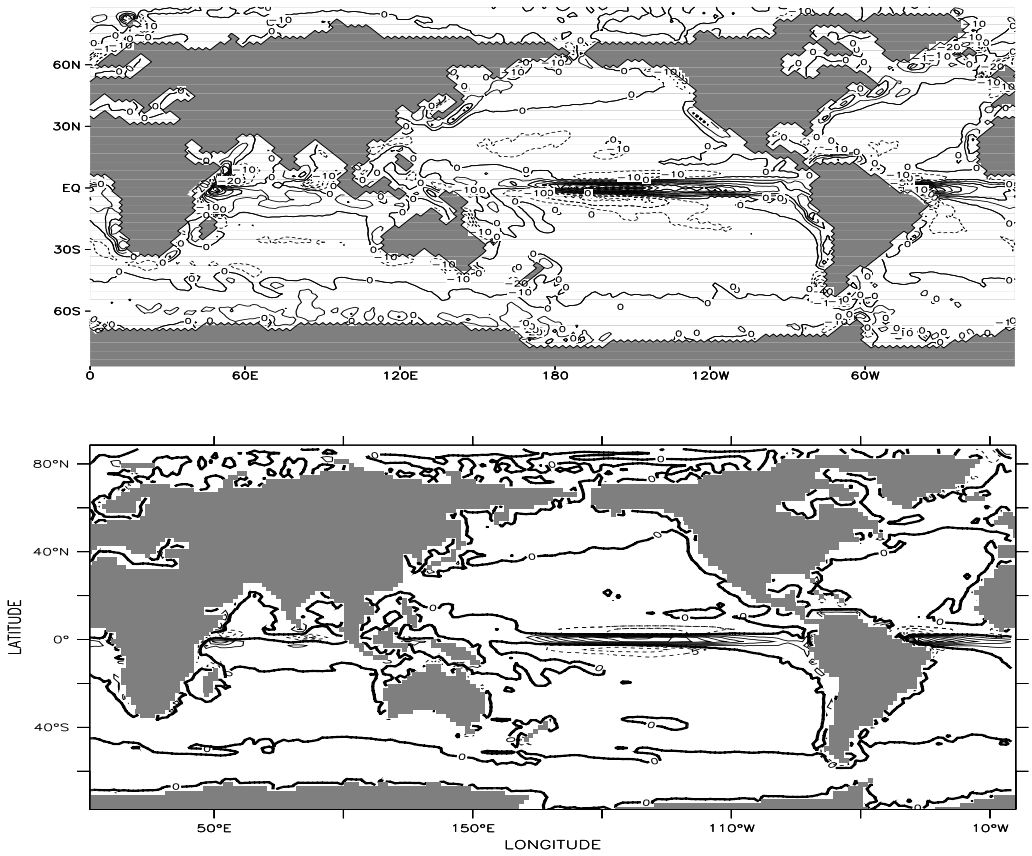

Figure 7.30: Vertical velocity at 20 m for HOPE (upper panel) and at 25 m for MOM2 (lower panel). Units are 10^{-6}ms^{-1}.

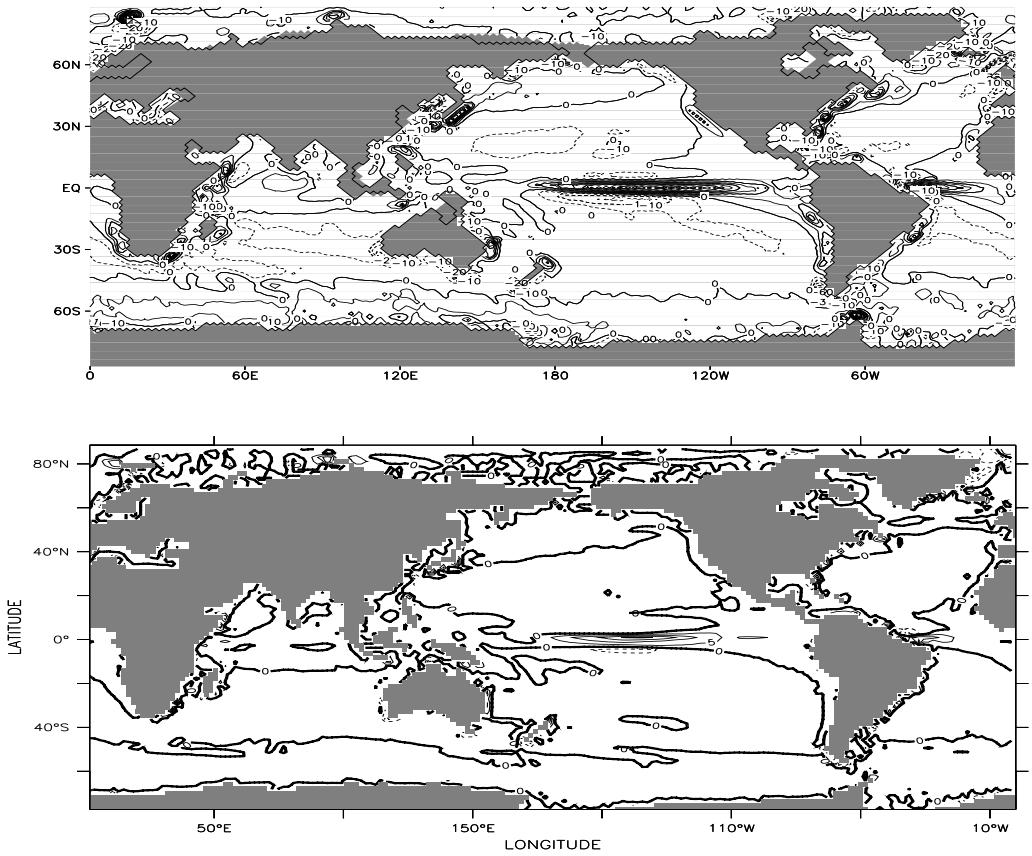

Figure 7.31: Vertical velocity at 82 m for HOPE (upper panel) and at 88 m for MOM2 (lower panel). Units are 10^{-6}ms^{-1}.

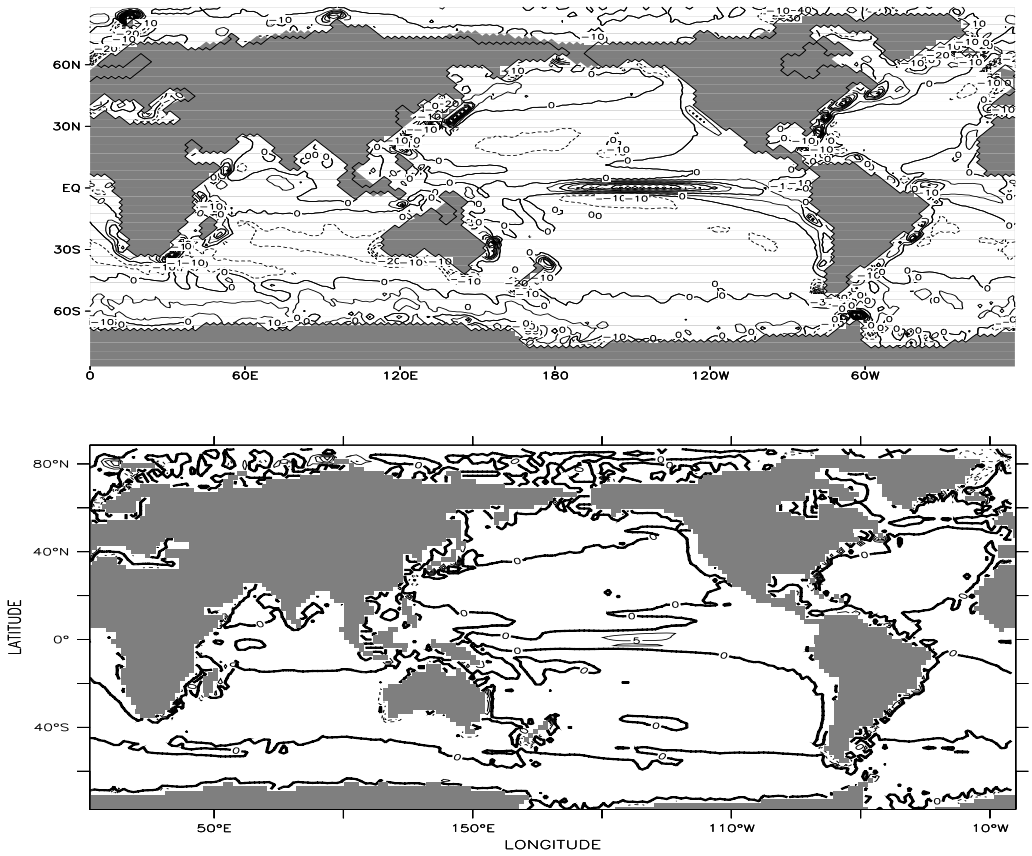

Figure 7.32: Vertical velocity at 115 m for HOPE (upper panel) and at 113 m for MOM2 (lower panel). Units are 10^{-6}ms^{-1}.

7.8 The deep circulation

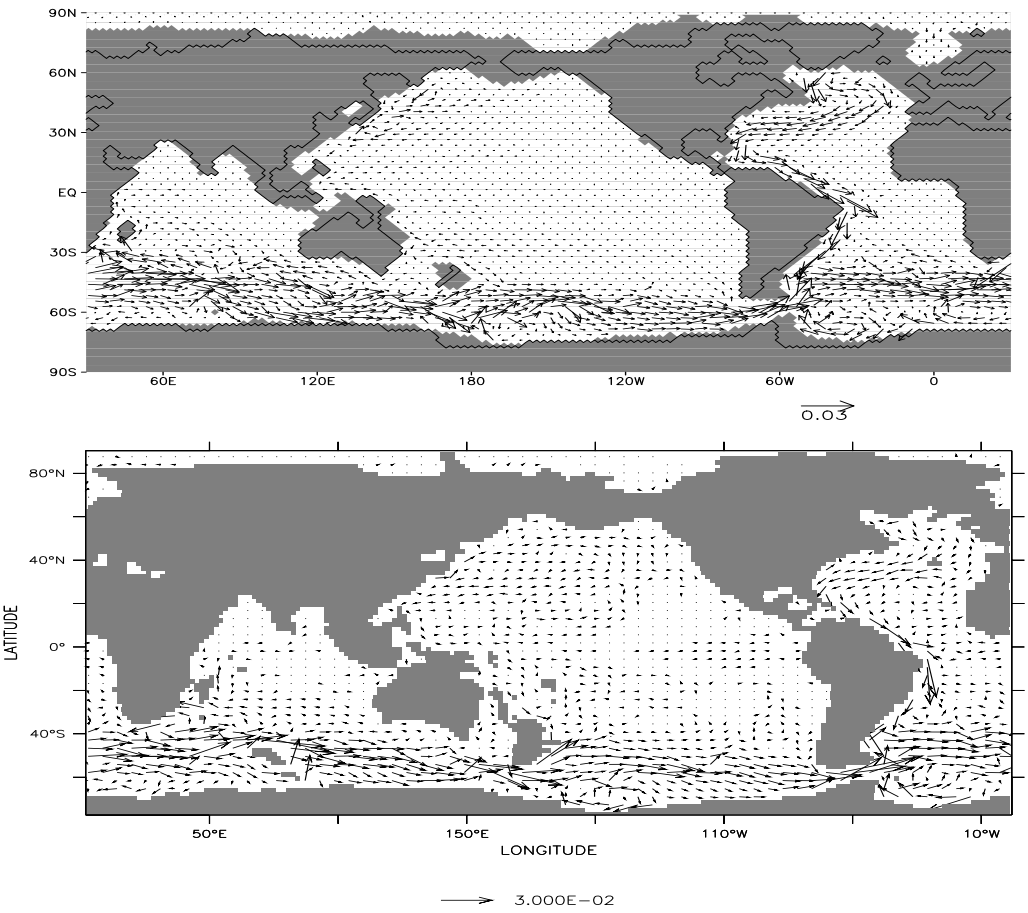

Figure 7.33: Horizontal velocity at 2000 m depth for HOPE (upper panel) and MOM2 (lower panel). The arrows are 0.03 m/s.

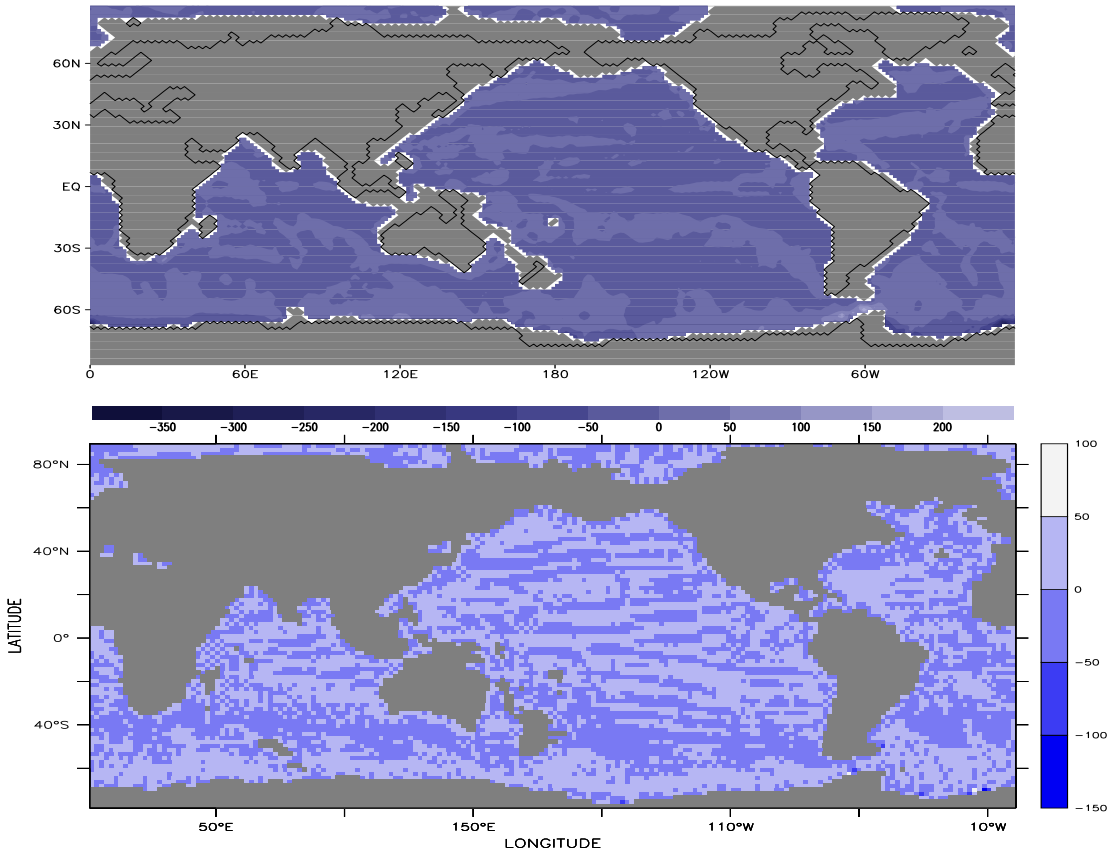

Figure 7.34: Vertical velocity at 2000 m depth for HOPE (upper panel) and MOM2 (lower panel). The gray shading indicates the the sign of w.

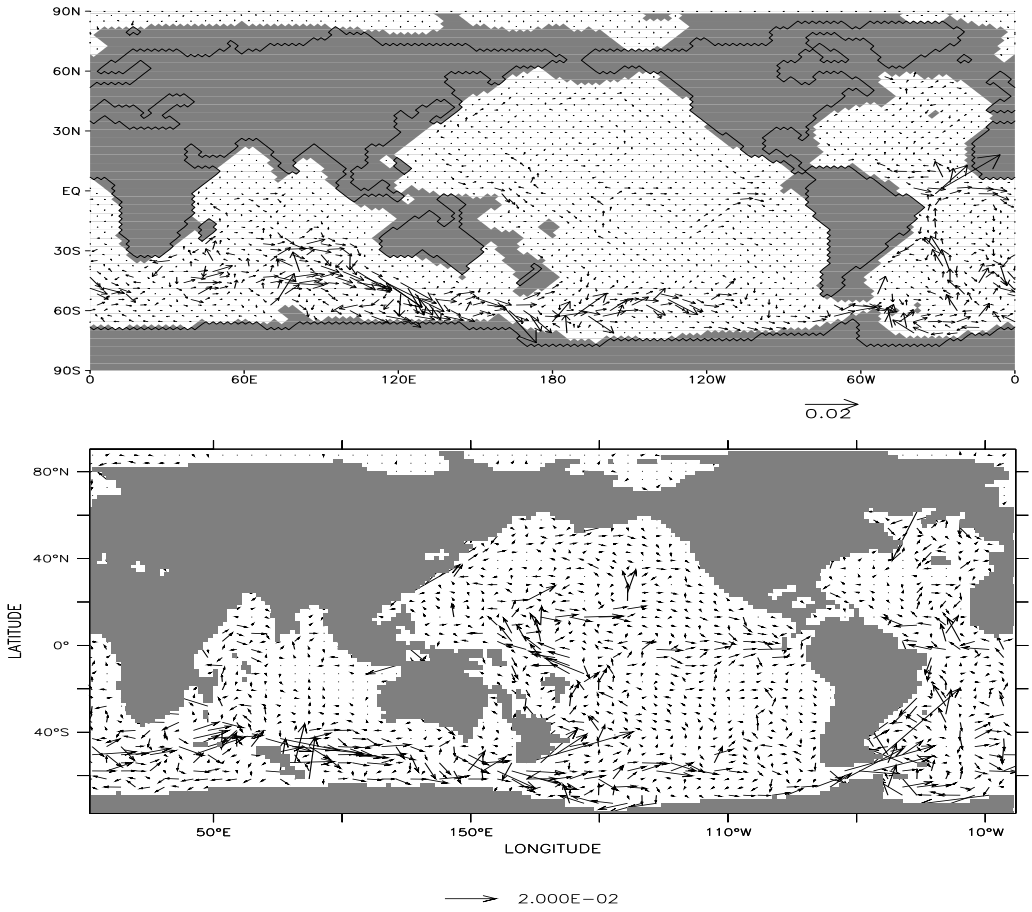

Figure 7.35: Horizontal velocity at the bottom for HOPE (upper panel) and MOM2 (lower panel). The arrows are 0.02 m/s.

7.9 Sea ice

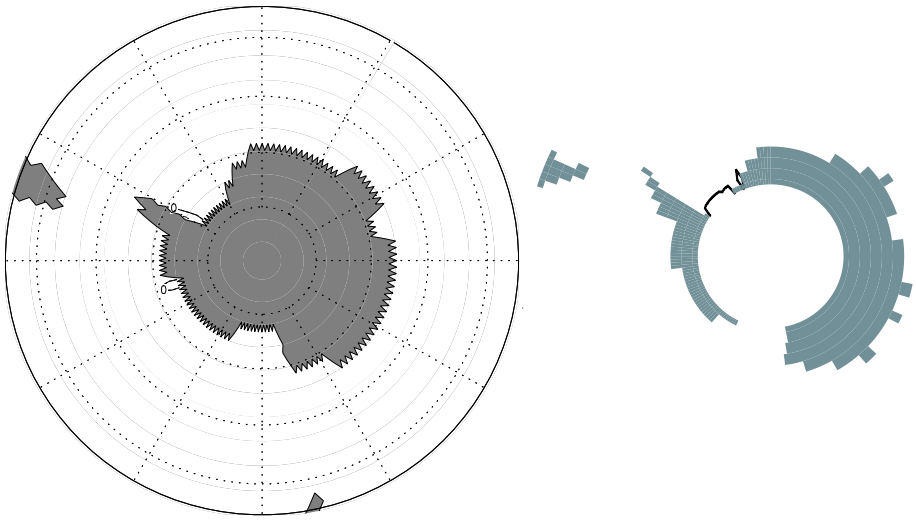

Figure 7.36: March ice concentration for HOPE (left panel) and MOM2 (right panel).

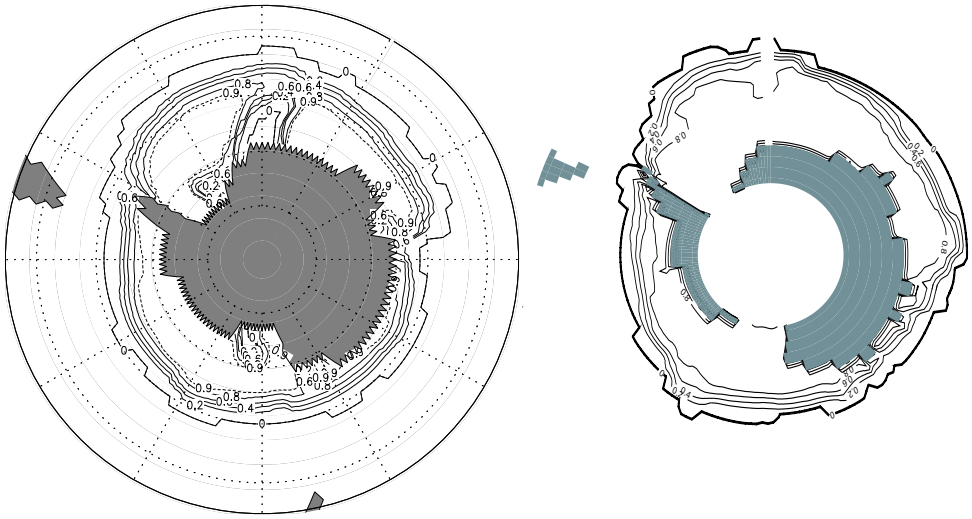

Figure 7.37: September ice concentration for HOPE (left panel) and MOM2 (right panel).

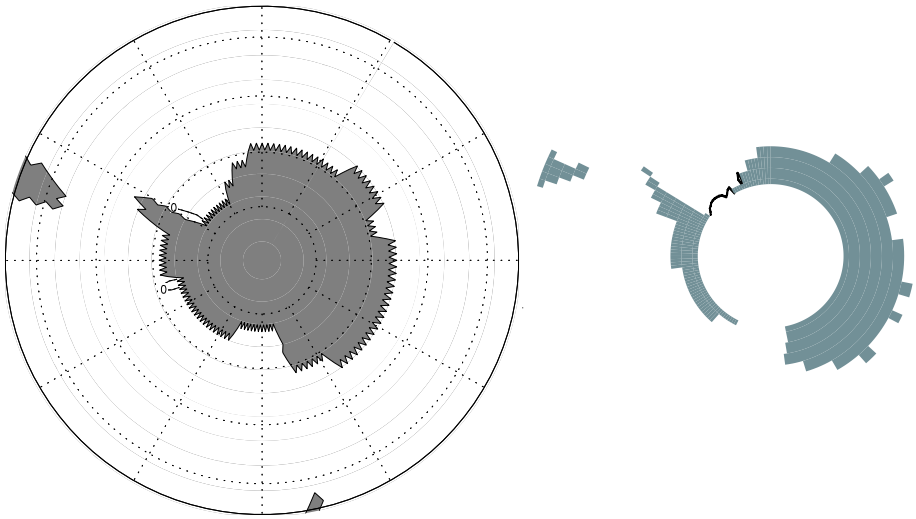

Figure 7.38: March ice thickness for HOPE (left panel) and MOM2 (right panel). Units m.

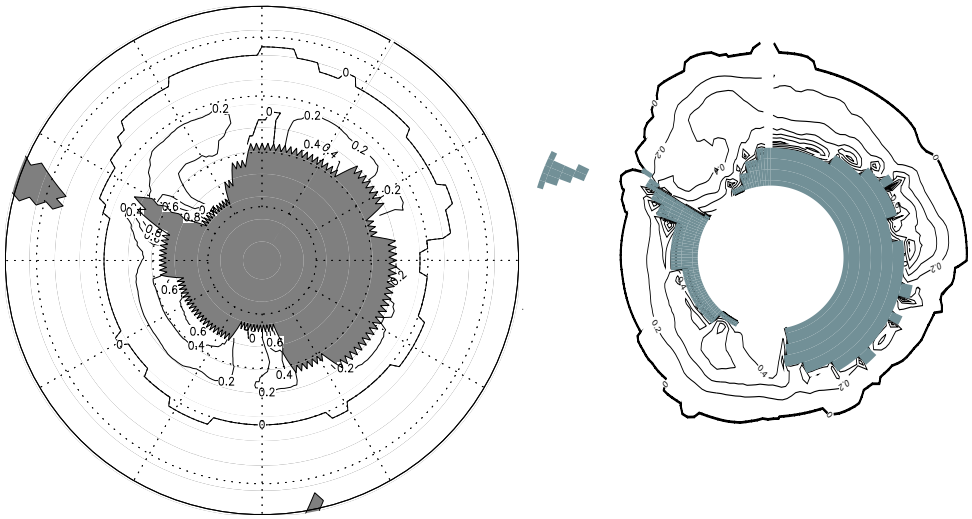

Figure 7.39: September ice thickness for HOPE (left panel) and MOM2 (right panel). Units m.

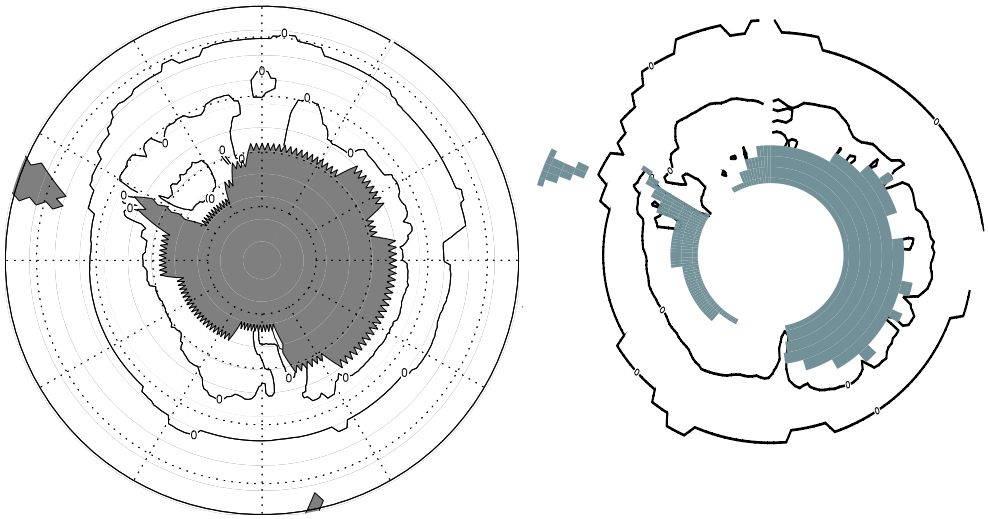

Figure 7.40: Ice growth for HOPE (left panel) and MOM2 (right panel). Units m.

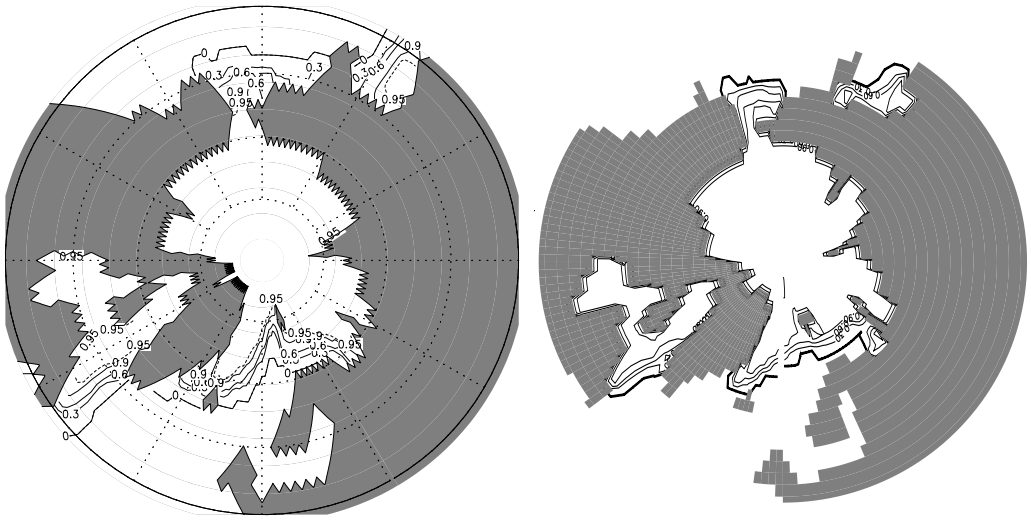

Figure 7.41: March ice concentration for HOPE (left panel) and MOM2 (right panel).

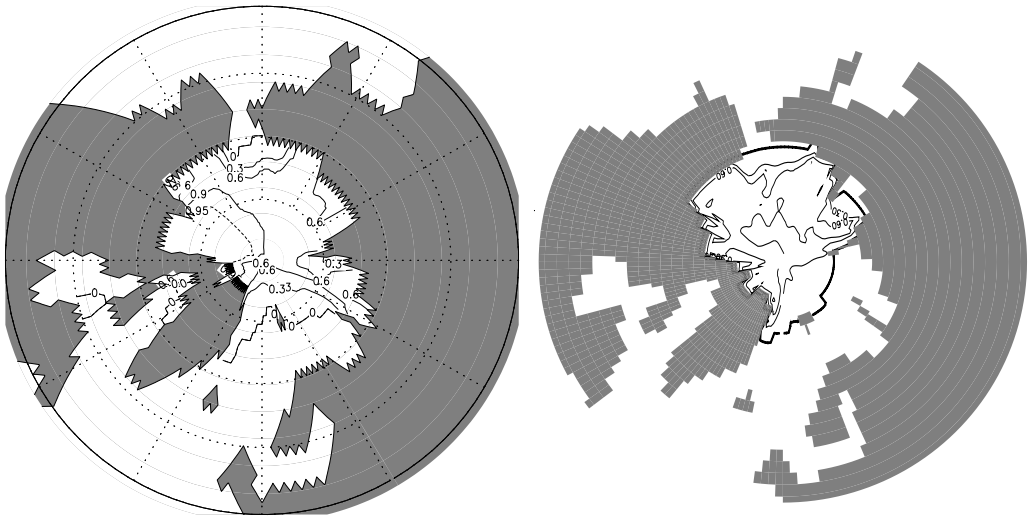

Figure 7.42: September ice concentration for HOPE (left panel) and MOM2 (right panel).

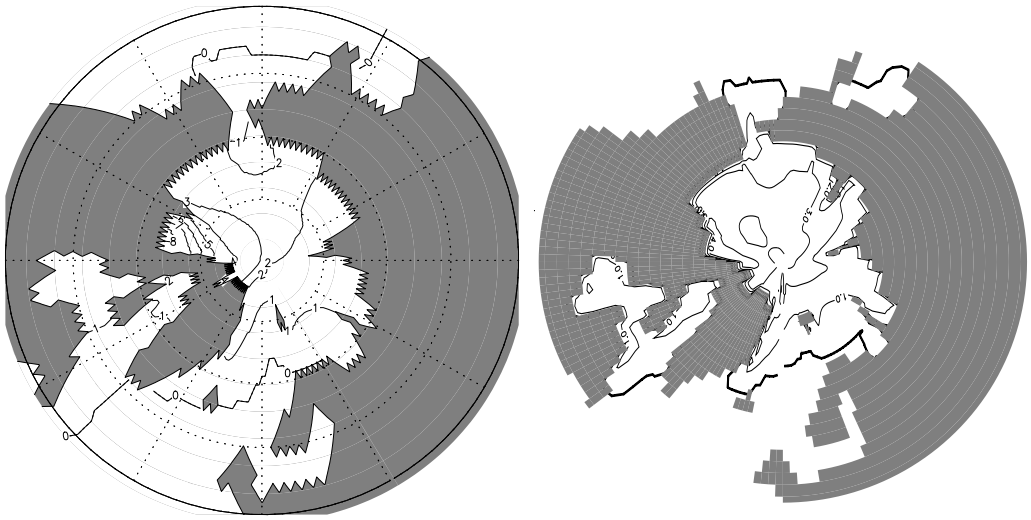

Figure 7.43: March ice thickness for HOPE (left panel) and MOM2 (right panel). Units m.

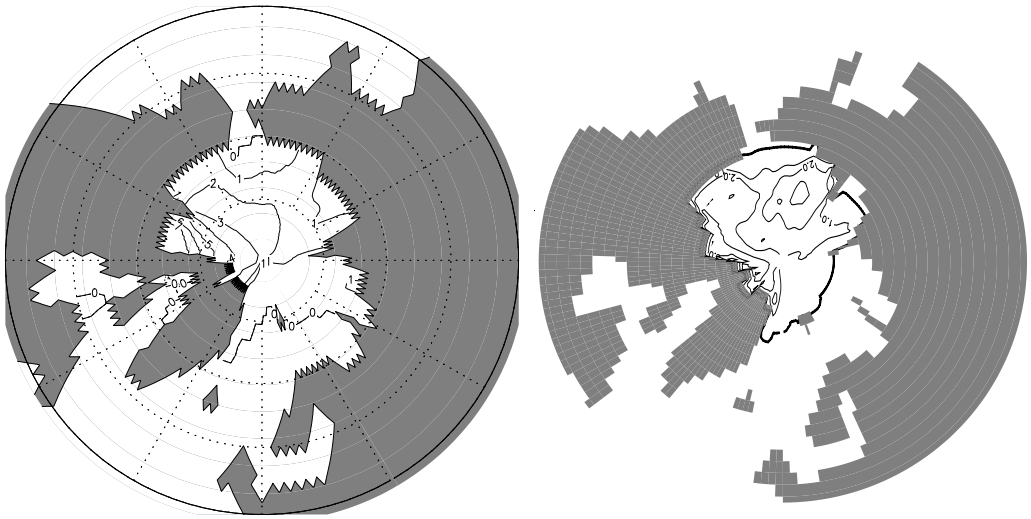

Figure 7.44: September ice thickness for HOPE (left panel) and MOM2 (right panel). Units m.

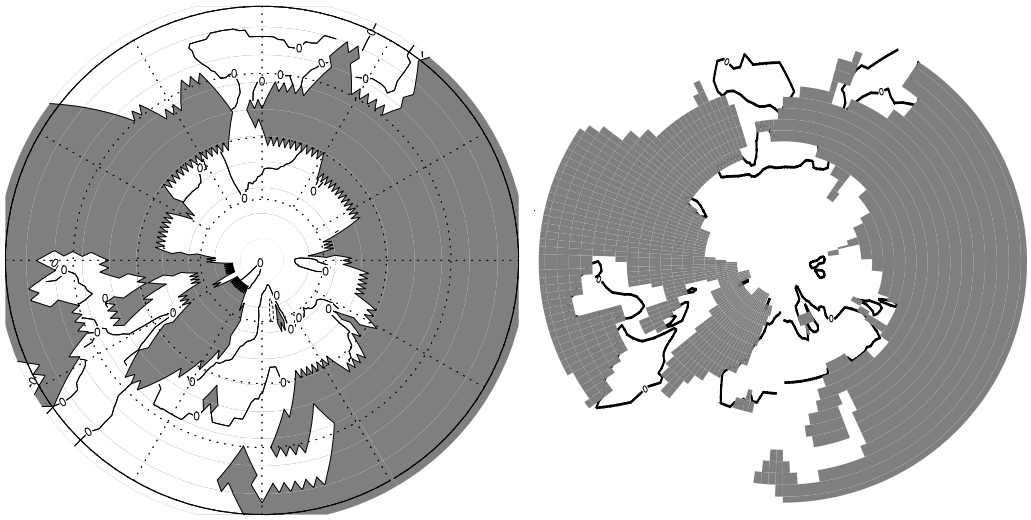

Figure 7.45: Ice growth for HOPE (left panel) and MOM2 (right panel). Units m.

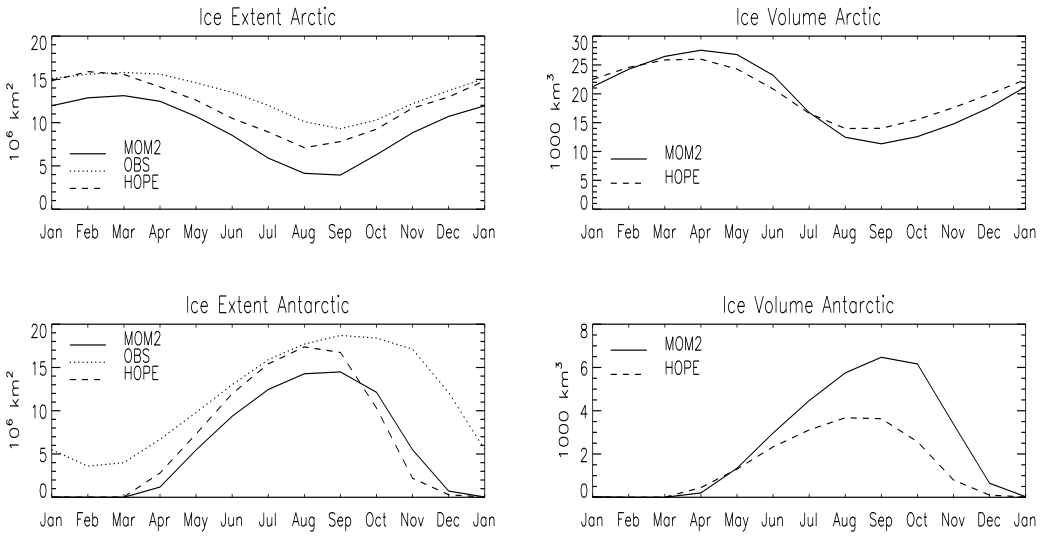

Figure 7.46: Seasonal cycle of ice extent and ice volume in the Arctic and Antarctic region. Observations are from Gloersen et al. (1992).

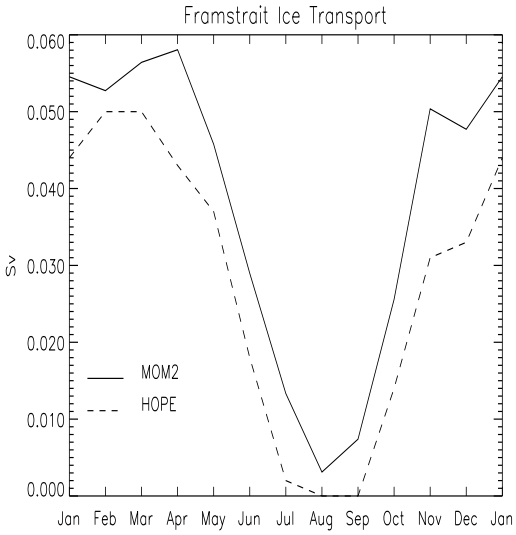

Figure 7.47: Seasonal cycles ice transport through Fram Strait.

7.10 Summary of the circulation features in the intercomparison experiments

The focus of this study is on global ocean-sea ice models that are components of coupled climate models. This focus demands the analysis of heat and fresh water fluxes, climate drift, and the renewal time of water masses.

As part of the climate system, ocean and sea ice contribute to the redistribution of heat and salt. The fluxes at the interface with the atmosphere (Figures 7.6 and 7.7) determine how the transports are partitioned into atmospheric and oceanic parts. The thermohaline circulation, often visualized as the meridional overturning streamfunction (Figure 7.5), represents a large part of the oceanic heat and water transports. At high latitudes, the correlation of horizontal velocity and zonal temperature anomalies becomes important (Figures 7.3, 7.10 and 7.28). Climate drift, the deviation from the initial climatology during the integration, is a complicated matter because it involves not only the quality of the models. Climate drift can be due to inadequate model physics, erroneous surface boundary values, or an inconsistency between surface boundary values and the climatology. Here we use horizontally averaged temperature and salinity profiles (Figure 7.26), zonally averaged sections of potential temperature and salinity (Figures 7.14 and 7.15), and zonally averaged sections for individual basins (Figures 7.17 through 7.25) to document climate drift in our models.

The renewal time of water masses is closely linked to the problem of climate drift because misrepresentation of renewal rates is an obvious cause of climate drift. Renewal rates are also important because they set a time scale for the response of the ocean to changes in surface boundary conditions. Renewal of water masses also determines the uptake of tracers by the ocean. The uptake of greenhouse gases represents another aspect of the ocean's ability to buffer climate signals. We will discuss water mass renewal together with climate drift and remind the reader of the CFC uptake experiments discussed in section 6.1.

Sea ice assumes a special role because of its important effect on the surface fluxes, especially its albedo and the feed back processes involved. Sea ice is treated separately in the following section.

Surface fluxes

Both models' net surface heat flux (Figure 7.6) features strong equatorial heating of the ocean. There is a larger heat uptake in MOM2 over the tropical Pacific as well as the tropical Atlantic. The SST in MOM2 contains a very elongated cold tongue in the eastern tropical Pacific as well as a very pronounced warm pool in the western tropical Pacific. One possible reason is an overestimate of the zonal SST gradients due to the GM parameterization (compare section 6.1). However, the large heat uptake and the low eastern SST in MOM2 is also consistent with the stronger upwelling (Figure 7.30) in the equatorial belt. These differences were unexpected because the prescribed wind stress dominates the equatorial upwelling. The reasons for the differences between MOM2 and HOPE are not entirely clear, however, we find deep upwelling in the Pacific that augments the wind driven upwelling in MOM2 (not shown). Apparently, the upwelling branch of the thermohaline circulation in MOM2 has a strong component in the low latitude Pacific that is not present in HOPE. The upwelling that compensates for the sinking of NADW and AABW in HOPE is placed somewhere else, probably in the Southern Ocean.

The Southern Ocean comprises marked differences between the models, especially in the Indian sector where HOPE takes up more heat than MOM2 does. In HOPE, there is strong heat uptake also located south of Australia that is not present in the MOM2 result. Almost all climatologies for surface heat flux contain the dipole in the Indian sector of the Southern Ocean that both models produce. On the other hand, few climatologies (e.g. NCEP) show the large, coherent area of heat uptake south of Australia. It should be noted, however, that the differences between the climatologies are much larger here, as in other basins, than between the two model results (Table 7.3).

Noticeable differences in surface heat flux also exist between the models in the North Atlantic.

There is a larger area of heat loss associated with the Gulf Stream/North Atlantic Current in MOM2. Here, the area of net heat loss of the ocean extends into the Nordic Seas and the Barents Sea. This is related to Atlantic water that is carried far to the north (Figure 7.28). MOM2 contains higher SST also in the East Greenland Current of the western Nordic Seas (Fig. 30). The SST gradient is almost meridional in MOM2, possibly a consequence of the filtering of active variables at higher northern latitudes. Both model results contain an erroneous heat uptake in the western subpolar gyre of the North Atlantic that is due to a wrong location of the North Atlantic Current (Sarmiento, 1986).

The surface fresh water flux (Figure 7.7) has a very similar structure in both models. Correspondingly, the surface salinity fields (Figure 7.11) are similar in both models. They are also very close to climatology. One important shortcoming, however, can be observed in both models in the East Greenland Current, which is too saline. As this water influences the downstream deep convection regions of the Irminger and Labrador Seas, this is a serious deficit that could affect the mean state as well as the variability in the models. The lack of fresh water export from the Arctic with the East Greenland Current leads to the thick Arctic halocline that develops in the models (see below). The large amplitude small-scale variability of Arctic surface salinity in HOPE is apparently smoothed by the filtering in MOM2.

Mass transport

The large scale overturning motion (Figure 7.5) has a similar structure in both models. The clearly defined NADW cell contains a southward flow centered at around 2000 m. Around 10 Sv of deep water are exported from the Atlantic in HOPE, an almost identical export is found in MOM2. The sinking motion near the Greenland-Scotland Ridge is more confined in HOPE whereas MOM2 also shows sinking of a few Sv at mid-latitudes. Greater differences exist in the inflow of AABW into the North Atlantic (2 Sv in HOPE, 4-5 Sv in MOM2). Even more pronounced differences can be found in the combined Indian/Pacific basin (not shown). Here, 7 Sv cross the equator northwards in MOM2 and large transports are incorporated in the tropical upwelling (see above). HOPE transports only 1-2 Sv across the equator and there is little addition, if any, to the Ekman cells at the equator.

These seemingly large differences in the Pacific should not be interpreted as a sign of huge differences in model physics. The overturning streamfunction is a very sensitive diagnostic where small changes in density can drive large differences in overturning. These differences in the zonally integrated transport can be located in rather narrow boundary regions and may vanish with longer integration times. It should also be noted that the shown streamfunction does not contain the eddy-induced transports that are included in MOM2. These transports are important, at least in the Southern Ocean where they reduce the effective strength of the Deacon cell.

Relatively large differences in the Southern Ocean also exist in the streamfunction for the vertically integrated transport (Figure 7.3). While the ACC strength is similar, the subtropical gyres of the Southern Hemisphere differ between the models. The gyres are generally somewhat stronger in MOM2. Since the wind forcing is identical, we assume that differences in the thermohaline driven part of the circulation, namely the stronger northward flow of AABW in MOM2 are responsible. The ACC transport at Drake Passage is around 100 Sv. One reason for the weak ACC is certainly the density contrast between high and middle southern latitudes that is smaller than observed (Figure 7.16). Both, higher temperatures and lower salinities in the model results near the Antarctic continent contribute to these deficiencies. This hints at problems in the formation of dense waters over the Antarctic shelves and the transport of these waters into the deep basins. Deep convection that both models erroneously simulate in the Weddell and Ross seas (Figure 7.9) is probably involved.

Surface elevation (Figure 7.27) is generally in good agreement with observations. HOPE simulates a height difference of 40 cm between Pacific and Atlantic while elevation in the two oceans is almost equal in MOM2. Again, we presume that the different formation and export rate of AABW in the models is connected to these differences. It should be noted, however, that surface elevation is a prognostic variable in HOPE while it is calculated diagnostically in MOM2. Problems in

solving the diagnostic equation can presently not completely be excluded.

Climate drift

Mean temperature and salinity profiles (Figure 7.26) provide a first quantitative estimate of climate drift from the initial conditions. Both model results are close to the observed temperature curve although HOPE is slightly warmer between 600 m and 2500 m depth. Both models are too warm above 600 m depth.

Regarding salinity, MOM2 exhibits less drift than HOPE except for the depth range between 1300 m and 3000 m. Here, we see the influence of the Mediterranean Water in the Atlantic. HOPE has a less pronounced Mediterranean Water signal although the mass exchange rate is higher than in MOM2 (Figure 7.4). Probably, this is due to enhanced mixing near the Straits of Gibraltar. We find largest drift in HOPE above 1000 m depth where the thickness of the subtropical haloclines is overestimated.

Zonal averages of temperature and salinity (Figures 7.14 and 7.15) provide more detail of the changes and their relation to dominant water masses. The effect of stronger northward transport of cold Antarctic waters at depth is visible in MOM2 although the effect is slight. Changes will appear larger for longer integration times than in our comparison experiments. On the other hand, very cold water of Antarctic origin is missing in both models. Antarctic intermediate water decreases rapidly in HOPE but is not ventilated enough in either model. There is an overly strong Mediterranean Water signal in the MOM2 result. The North Pacific Intermediate Water appears well-defined in MOM2, less so in HOPE. The permanent thermocline considerably deepens in both models. There is a strong front, as observed, between the subpolar and polar regimes (at around 60°N) in MOM2. Further north, we find an Arctic intermediate layer that is too warm in both models and occupies too large a depth range. The strong thermocline and halocline at high latitudes are present in both models. The Arctic halocline is too thick in both models.

Many of these features of the global averages are especially pronounced in the Atlantic (Figures 7.17 and 7.18). Additional highlights of the tracer distributions in this basin are

- a too weak stratification in the Southern Ocean in both models. The AABW is too warm.
- a very well reproduced AAIW, esp. in MOM2.
- a strong signature of NADW with increased salinity in both models. This reflects the Mediterranean Water influence in MOM2 and too strong mixing of the overflow waters with ambient more saline waters in both models.
- an intrusion of relatively fresh water from high latitudes to south of 60°N centered at 1500 m. This 'North Atlantic Intermediate Water' is expected to become more important during extended integration. This hints at rather fundamental problems with the representation of the Arctic in both models. These problems are connected to the storage of fresh water in a much too thick Arctic halocline. This is the case in both models but is especially pronounced in MOM2.

Sea ice

There is almost no Antarctic sea ice in summer in both models (Figure 7.36). This is basically correct although small ice covered regions should exist in summer. The comparison with satellite data in Figure 7.46 shows that both models underestimate the sea ice cover in the Southern Hemisphere in the spring and summer months (September through April). Otherwise, both model results and observations are similar. Winter sea ice thickness is typically 20 to 50 cm, which is in the observed range. MOM2 exhibits a larger seasonal cycle in ice volume than HOPE, implying thicker winter ice. However, there are no data to validate the models in this respect.

The HOPE winter sea ice distribution in the Southern Hemisphere contains large-scale polynias in the eastern and southern Weddell Sea. These are due to erroneous heat transport to the surface

by deep convective mixing (Figure 7.9). A similar problem, although on a smaller scale, exists in the southern Ross Sea. MOM2 has a connected sea ice cover in winter that is more realistic for mean Antarctic conditions. The convection that also occurs in MOM2 in the Weddell Sea (Figure 7.9) is apparently not sufficient to melt the ice as it does in the HOPE result.

In the Northern Hemisphere, the models differ in sea ice extent in the Greenland and Labrador seas as well as in the Barents Sea (Figures 7.41 and 7.42). The transition between the ice edge and the fully covered region is broader in HOPE, a fact that has to be taken into account when comparing sea ice extent figures. Both models underestimate the sea ice extent in the Arctic during all seasons (Figure 7.46). Because sea ice is very sensitive to the albedo and other parameters, this discrepancy should not be taken as a serious model failure. However, it demonstrates that the parameter values must be fine-tuned and carefully validated. Another consideration is that the forcing field might not represent the conditions over the averaging period of the satellite observations. Due to the strong nonlinearity of sea ice processes, this would be hard to achieve without using the actual atmospheric forcing data for exactly the same period. We find, for instance, that the Kara Sea is not ice covered during summer in MOM2, a situation that is in the observed range although not typical for long periods.

Summer ice concentrations in both models drop to significantly below 90% in both models near the land boundaries (Figure 7.42). A larger ice free area exists in HOPE near the Bering Strait, a consequence of the stronger inflow from the Pacific in that model. This might be connected to the larger difference in sea level between the Pacific and the Arctic in that model (Figure 7.27).

Ice thickness distributions realistically show thickest ice north of the Canadian Archipelago (Figures 7.43 and 7.44). Ice thickness reaches 8 m in HOPE whereas ice thickness does not exceed 5 m in MOM2. There is a considerable seasonal cycle in ice volume. The seasonal changes occur especially in the far eastern Arctic. Again, there is no observational database to validate the models in this respect. Observations after Barry et al. (1993) indicate that the ice thickness of MOM2 is more realistic in the Central Arctic, whereas that of HOPE is more realistic close to the Canadian Archipelago.

The Arctic fresh water gain through rivers and Pacific inflow is mainly compensated by fresh water export through Fram Strait, both in liquid and solid phases. This export is especially significant because the fresh water flows very close to the deep-water formation areas of the North Atlantic. Anomalies of these transports in strength and pathways could affect deep-water production. An especially interesting quantity is thus the Fram Strait ice export shown in Figure 7.47. The models have very similar results with almost vanishing transport in August (the HOPE transports actually vanish in August and September) and maximum export in February (MOM2) and April (HOPE). The maximum values are close to 0.05 Sv or approximately 1500 km^3/yr. These maximum values are below the estimates based on observations for the mean sea ice transport through Fram Strait. Vinje et al. (1998) give a mean transport for the period 1990-1996 of 2850 km^3/yr. The minimum annual transport of 2050 km^3/yr occurred in 1991. It is apparent that we simulate a sea ice export from the Arctic through Fram Strait (the only outlet in the model geometry) that is significantly below observed values. This has consequences for the fresh water balance and the stratification in the Arctic. To achieve a balance, the oceanic (liquid) export must be larger than observed. To increase the transport, the halocline in the Arctic first has to deepen (Figure 7.18). The thick insolating layer will buffer the system and will thus leave the models insensitive to anomalies in the forcing.

Outlook

C-HOPE is the newly developed version of the original HOPE model formulated on the Arakawa C-grid. Like its predecessor HOPE, C-HOPE is a z-coordinate global general circulation model of the ocean based on the primitive equations. It utilizes the hydrostatic and Boussinesq assumptions common in large scale models and has a free surface. C-HOPE also contains an embedded dynamic-thermodynamic sea ice model with viscous-plastic rheology and snow.

Unlike its predecessor, C-HOPE utilizes a horizontal curvilinear grid (conformal mapping of geographical coordinates) to accomodate increased resolution in regions of interest without the

interior boundary problems of nested models. The standard grid setup used for global general circulation studies places the North Pole in Greenland to avoid distorted physics. The South Pole, while remaining over land, is moved an equivalent distance along the same longitude line to keep the zero-latitude line along the Equator (Fig.7.48). Other new features include a parameterization of slope convection and a higher-order advection scheme.

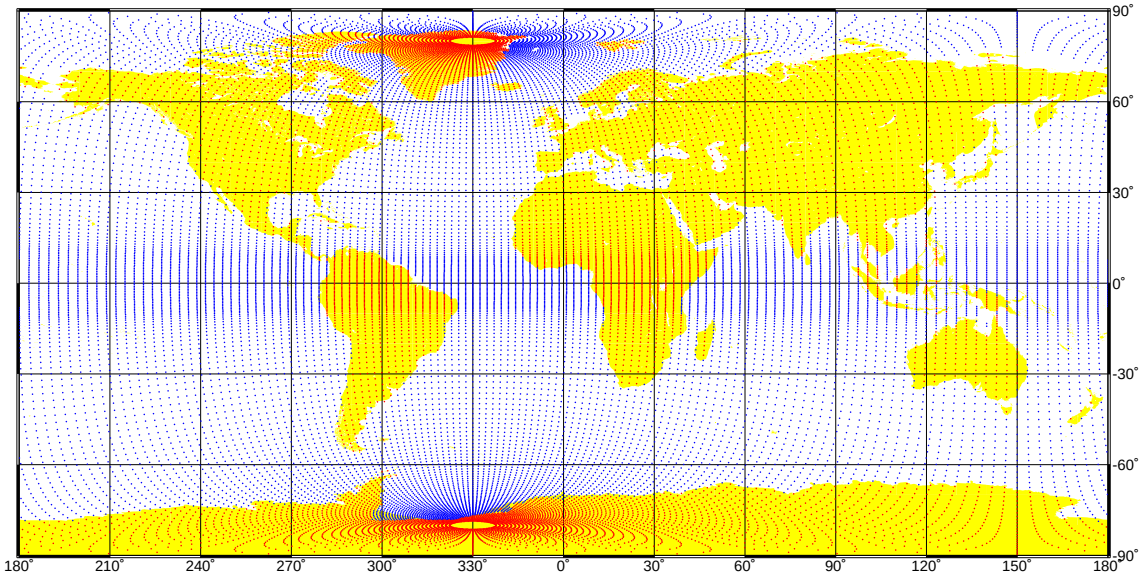

Figure 7.48: The grid of the new version CHOPE.

C-HOPE is currently undergoing optimization and tuning. From a 100-year test run of a recent C-HOPE prototype using the OMIP-Forcing the meridional stream function is shown (Fig.7.49).

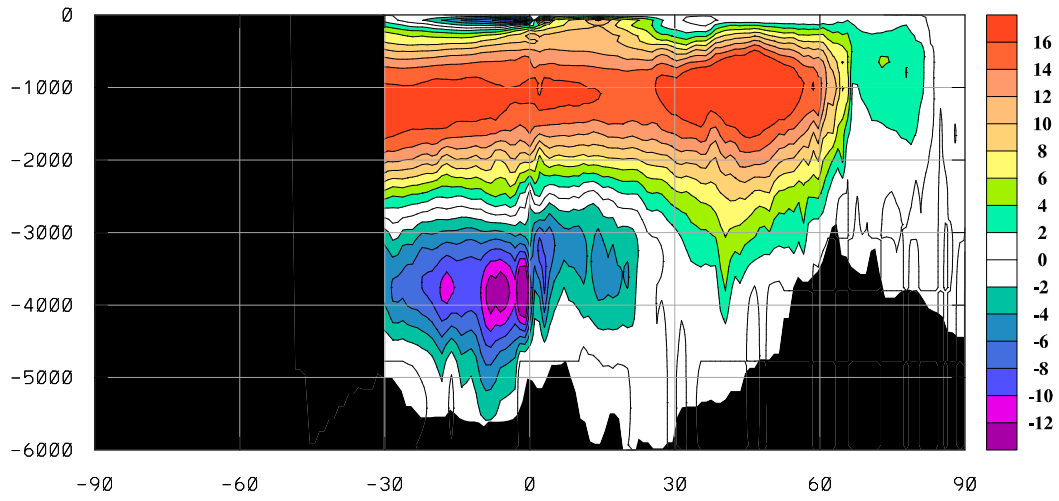

Figure 7.49: Streamfunction of the meridional overturning in the Atlantic for the CHOPE version. Units Sv.

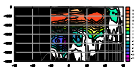

References

Adcroft, A., C. Hill, and J. Marshall, 1997: Representation of Topography by Shaved Cellsin a Height Coordinate Ocean Model. Mon.Weath.Rev., 125, 2293-2315.

Arakawa, A. and V. R. Lamb, 1977: Computational design of the basic dynamical processes of the UCLA general circulation model, Meth. Comput. Phys., 17, 173-265.

Baringer, M.O'N. and J.F.Price, 1997: Mixing and spreading of the Mediterranean outflow. JPO,27(8),1654-1677, 1997.

Barry, R.G., M.C.Serreze, J.A.Maslanik and R.H.Preller, 1993: The Arctic Sea Ice-Climate System: Observations and Modeling. Reviews of Geophysics, 31, 4, pp.397-422, 1993.

Böning, C.W., W.R. Holland, F.O. Bryan, G.Danabasoglu, and J.C. McWilliams, 1995: An overlooked problem in model simulations of the thermohaline circulation and heat transport in the Atlantic Ocean, J.Climate, 8, 515-523.

Beckmann, A., and R. Döscher, 1997: A method for improved representation of dense water spreading over topography in geopotential-coordinate models, J.Phys.Oceanogr., 27, 581-591.

Beckmann, A., C.W. Böning, C. Köberle, and J.Willebrand, 1994: Effects of increased horizontal resolution in a simulation of the North Atlantic Ocean, J.Phys.Oceanogr., 24, 326-344.

Berliand, M.E. and T.G.Berliand, 1952: Determining the net long-wave radiation of the Earth with consideration of the effect of cloudiness. Isv. Akad. Nauk. SSSR Ser. Geofis, No. 1.

Borowski, D., R. Gerdes and D. Olbers, 2000: Thermohaline and wind forcing of a circumpolar channel with blocked geostrophic contours, in preparation.

Bryan, F.O, 1986: High-latitude salinity effects and interhemispheric thermohaline circulations. Nature, 323, 310-304.

Bryan, K., 1969: A numerical method for the study of the circulation of the world ocean. J.Comput.Phys. 4, 347-376.

Bryan, K. and L. J. Lewis, 1979: A Water Mass Model of the World Ocean. J.Geophys.Res.,85(C5), 2503-2517.

Bryan, K., 1984: Accelerating the convergence to equilibrium of ocean-climate models,J.Phys.Oceanogr., 14, 666-673.

Bryden, H.L., 1973: New polynomials for thermal expansion, adiabatic temperature gradient and potential temperature of sea water. Deep Sea Research, Vol.20, pp. 401-408, 1973.

Bryden,H.L., D.H.Roemmich, and J.A.Church, 1991: Ocean heat transport across 24°N in the Pacific. DSR, 38, No.3, 297-324, 1991.

Buck, A.L., 1981: New Equations for Computing Vapor Pressure and Enhancement Factor.J.Appl.Met., Vol.20, p. 1527-1532.

Budyko, M.I., 1974: Climate and life. English edition ed. by D.H.Miller. Academic Press,Internat. Geophysics Series, New York.

Chassignet, E.P., L. Smith, and R. Bleck, 1996: A Model Comparison: Numerical Simulations of the North and Equatorial Atlantic Oceanic Circulation in Depth and Isopycnic Coordinates, J.Phys.Oceanogr., 26, 1849-1867.

Chen, C.-T. and E. Roeckner, 1996: Validation of the Earth radiation budget as simulated by the Max Planck Institute for Meteorology general circulation model ECHAM4 using satellite observations of the Earth Radiation Budget Experiment. J.Geophys.Res., 101, 4269-4287.

Cox, M.D., 1975: A Baroclinic Numerical Model of the Word Ocean: Preliminary Results, in Numerical Models of Ocean Circulation, edited by P. of a Symp., Durham, New Hampshire.

Cox, M.D., 1984: A primitive equation three dimensional model of the ocean.GFDL Ocean Group Tech. Rep. No.1, Geophysical Fluid Dynamics Laboratory/NOAA, 250pp.

da Silva, A.M., C.C.Young und S.Levitus, 1994: Atlas of surface marine data 1994, Vol.1-5, NOAA Atlas NESDIS 6-10.

Danabasoglu, G. and J.C. McWilliams, 1995: Sensitivity of the global ocean circulation to parameterizations of mesoscale tracer transports, J.Climate, 8, 2967-2987.

Dixon, K.W., J.L.Bullister, R.H. Gammon, and R.J. Stouffer, 1996: Examining a coupled climate model using CFC-11 as an ocean tracer, Geophysical Research Letters, 23,1957-1960.

Drijfhout, S. S., E. Maier-Reimer, and U. Mikolajewicz, 1996: Tracing the conveyor beltin the Hamburg large-scale geostrophic ocean general circulation model. J.Geophys.Res.,101, 22563-22575.

Drijfhout, S., C. Heinze, M. Latif, and E. Maier-Reimer, 1995: Mean Circulation and Internal Variability in an Ocean Primitive Equation Model, Report No. 177, MPI, Hamburg,J. Phys. Oceanogr., 26, 559-580.

Dümenil, L., K. Isele, H.-J. Liebscher, U. Schröder, M. Schumacher, K. Wilke,1993: Discharge data from 50 selected rivers for GCM Validation. Global Runoff Data Centre, Koblenz, und Max-Planck-Institut für Meteorologie, Rep. No. 100, Hamburg,März 1993.

DYNAMO Group, 1997: Dynamics of North Atlantic Models: Simulation and assimilation with high resolution models. Bericht Nr. 294 aus dem Institut für Meereskunde an der Christian-Albrechts-Universität Kiel.

Eby, M., and G. Holloway, 1994: Sensitivity of a large-scale ocean model to a parameterization of topographic stress. J.Phys.Oceanogr., 24, 2577-2588 Gent P.R., and J.C.McWilliams, 1990: Isopycnal mixing in ocean circulation models. J.Phys.Oceanogr. 20, 150-155.

England, M.H., 1993: On the formation of global-scale water masses in ocean generalcirculation models, J.Phys.Oceanogr., 23, 1523-1552.

England, M.H., and A.C. Hirst, 1997: Chlorofluorocarbon uptake in a world ocean model 2. Sensitivity to surface thermohaline forcing and subsurface mixing parameterizations,J.Geophys.Res., 102, 15709-15731.

ERA, 1997: ECMWF Re-Analysis, Project Report Series, 1. ERA Description J.K.Gibson, P.Kallberg, S.Uppala, A.Hernandez, A.Nomura, E.Serrano. European Centre for Medium-Range Weather Forecasts, Reading, England.

Fairall, C.W., E.F.Bradley, D.P.Rogers, J.B.Edson and G.S.Young: Bulk parameterization of air-sea fluxes for Tropical Ocean-Global Atmosphere Coupled-Ocean Atmosphere Response Experiment. J.Geophys.Res., Vol.101, No. C2, p. 3747-3764.

Fandry, C. and R.D.Pillsbury, 1979: On the estimation of absolute geostrophic volume transport applied to the Antarctic circumpolar current. JPO 9(3),449-455, 1979.

Fieux, M., C.Andrie, P.Delecluse, A.G.Ilahude, A.Kartavtseff, F.Mantisi, R.Molcard, J.C.Swallow, 1994: Measurements within the Pacific-Indian oceans throughflow region. DSR, PartI 41(7), 1091-1130, 1994.

Frey, H., M. Latif, and T. Stockdale, 1997: The Coupled GCM ECHO-2. Part I: The Tropical Pacific. Mon.Wea.Rev., 125, No.5, 703-720.

Frickenhaus, S., and W. Hiller, 2000: Coupling Parallel Atmosphere- and Ocean-models in a Metacomputing Environment. Berichte aus dem Fachbereich Physik, No. 99, Alfred-Wegener-Institut, Bremerhaven.

Gates, W. L., 1992: AMIP: The Atmosphere Model Intercomparison Project. Technical Report 7, Program for Climate Model Diagnosis and Intercomparison, Lawrence Livermore National Laboratory, L-264, PO Box 808, Livermore, CA, 94550, USA.

Gent, P.R., and J.C. McWilliams, 1990: Isopycnal mixing in ocean circulation models,J.Phys.Oceanogr., 20, 150-155.

Gerdes, R. (1993): A primitive equation ocean circulation model using a general vertical coordinate transformation. Part 1: Description and testing of the model. J.Geophys.Res., 98, 14683-14701.

Gerdes, R. (1993): A primitive equation ocean circulation model using a general vertical coordinate transformation. Part 2: Application to an overflow problem. J.Geophys.Res., 98, 14703-14726.

Gerdes, R. and C. Köberle, 1995: On the Influence of DSOW in a numerical model of the North Atlantic general circulation, J.Phys.Oceanogr., 25, 2624-2642.

Gerdes, R., C. Köberle, and J. Willebrand, 1991: The influence of numerical advection schemes on the results of ocean general circulation models, Climate Dynamics, 5, 211-226.

Gerdes, R. and Ch. Wübber, 1991: Seasonal variability of the North Atlantic Ocean model intercomparison, J.Phys.Oceanogr. 21, 1300-1322.

Gill, A.E., 1982: Atmosphere-Ocean Dynamics. International Geophysics Series, Vol. 30,Academic Press, 1982.

Gloersen, P., W.J.Campbell, D.J.Cavalieri, J.C.Comiso, C.L.Parkinson, and H.J.Zwally,1992: Arctic and Antarctic Sea Ice, 1978-1987, Scientific and Technical Information Program, NASA, Washington, D.C.

Gnanadesikan, A., and R.W. Hallberg, 2000: On the relationship of the circumpolar current to southern hemisphere winds in coarse-resolution ocean models, J.Phys.Oceanogr., 30, 2013-2034.

Godfrey, J.S. und A.C.M. Beljaars, 1991: On the Turbulent Fluxes of Buoyancy, Heat and Moisture at the Air-Sea Interface at Low Wind Speeds. J.Geophys.Res., Vol.96, No.C12,p. 22043-22048.

Goose, H., E. Deleersnijder, T.Fichefet, and M.H.England: 1999, Sensitivity of a global coupled ocean-sea ice model to parameterization of vertical mixing, J.Geophys.Res., 104, 13681-13695.

Hagemann, S. and L. Dümenil, 1998: A parametrization of the lateral waterflow for the global scale. Clim. Dyn. 14 (1), p. 17-31.

Harder, M., P.Lemke, M.Hilmer, 1998: Simulation of sea ice transport through Fram Strait: Natural variability and sensitivity to forcing. J.Geophys.Res., Vol.103, No. C3,p. 5595-5606.

Hecht, M.W., W.R. Holland, and P.J.Rasch, 1995: Upwind-weighted advection schemes for ocean tracer transport: An evaluation in a passive tracer context, J.Geophys.Res., 100, 20763-20778.

Hellerman, S., and M. Rosenstein, 1983: Normal monthly wind stress over the world oceanwith error estimates, J.Phys.Oceanogr., 13, 1093-1104.

Hibler, W.D., 1979: A dynamic-thermodynamic sea-ice model, J.Phys.Oceanogr., 9, 815-845.

Hibler, W.D., and K.Bryan, 1987: A diagnostic ice-ocean model, J.Phys.Oceanogr., 17,987-1015.

Holloway, G., 1992: Representing topographic stress for large-scale ocean models. J.Phys.Oceanogr., 22, 1033-1046.

Hopkins, T.S.,1999: The thermohaline forcing of the Gibraltar exchange. Journal of Marine Systems, 20(1-4), 1999.

Ichikawa, H. and Asuka Group, 1998: Heat ans salinity transports of the Kuroshio in the East China Sea and south of Shikoku. Umi to Sora [Sea and Sky], 74(2), 51-61, 1998.

Inoue, M., and S.E.Welsh, 1993: Modeling seasonal variability in the wind-driven upper-layer circulation in the Indo-Pacific region. JPO, 23(7), 1411-1436, 1993.

Johns, W.E., T.N.Lee, R.J.Zantopp, and E.Fillenbaum, 1997: Updated Transatlantic Heat Flux at 26.5°N. WOCE Newsletter No.27, July 1997, p.15-22.

Josey, S.A., E.C.Kent and P.K.Taylor, 1999: New insights into the ocean heat budget closure problem from analysis of the SOC air-sae flux climatology. Journal of Climate,12(9), p. 2856-2880.

Kim, S. J. and A. Stössel, 1998: On the representation of the Southern Ocean watermasses in an ocean climate model. J.Geophys.Res., 103(C11), 24891-24906.

Kim, S. J., T. J. Crowley, and A. Stössel, 1998: Local orbital forcing of Antarctic climate change during the last interglacial. Science, 280(5364), 728-730.

Koerner, R.M. 1973: The mass balance of the sea ice in the Arctic Ocean. Journal of Glaciology, Vol.12, No. 65, 173-185.

Kreyscher, M., M.Harder, and P.Lemke, 1997: First results of the sea ice model intercomparison Project (SIMIP), Ann. Glaciol., 25, 8-11.

Large, W.G., and Pond, S., 1982: Sensible and Latent Heat Flux Measurements over the Ocean. J.Phys.Oceanogr.,12, 464-482.

Latif, M., T. Stockdale, J.-O. Wolff, G. Burgess, E. Maier-Reimer, M. M. Junge, K. Arpe,and L. Bengtsson, 1994: Climatology and variability in the ECHO coupled GCM. Tellus, 46A, 351-366.

Legates, D. R. and C. J. Willmott, 1990: Mean seasonal and spatial variability in gauge-corrected, global precipitation. Int.J.Climatol., 10, 111-127.

Legutke, S. and E. Maier-Reimer, 1999: Climatology ot the HOPE-G Global Ocean General Circulation Model. Techn. Rep. No.21, Deutsches Klimarechenzentrum, Hamburg.Levitus, S.,R. Burgett and T. Boyer, 1994: World Ocean Atlas, 1994: Volume 3, Salinity. NOAA Atlas NESDIS 3.

Legutke, S., E. Maier-Reimer, A. Stössel, and A. Hellbach, 1997: Ocean - sea-ice coupling in a global general circulation model. Annals of Glaciology, 25, 116-120.

Leaman, K.D., R.L.Molinari and P.S.Vertes, 1987: Structure and variability of the Florida current at 27 degrees N: April 1982-July 1984. JPO, 17(5), 565-583, 1987.

Levitus, S., Climatological Atlas of the World Ocean, Professional paper no.13, NOAA, Rockville, MD., 1982.

Levitus, S., and T.P. Boyer, 1994: World Ocean Atlas 1994, volume 4: Temperature, NOAA Atlas NESDIS 4, NOAA, Washington D.C.

Levitus, S., R. Burgett, and T.P. Boyer, 1994: World Ocean Atlas 1994, volume 3:Salinity, NOAA Atlas NESDIS 3, NOAA, Washington D.C.

Lohmann, G., R. Gerdes and D. Chen, 1996: Stability of the thermohaline circulation in a simple coupled model. Tellus, 48A, 465-477.

Macdonald, A.M., 1993: Property fluxes at 30° and their implications for the Pacific-Indian throughflow and the global heat budget. JGR, 98(C4), 6851-6868, 1993.

Macdonald, A.M. and C.Wunsch, 1996: Oceanic Estimates of Global Ocean Heat Transport. WOCE Newsletter No.24, Oct.1996, p.5-6.

Maier-Reimer, E., Mikolajewicz, U., 1992: The Hamburg Large Scale Geostrophic Ocean General Circulation Model (Cycle 1), Techn. Rep. No. 2, Deutsches Klimarechenzentrum, Hamburg.

Maier-Reimer, E., Mikolajewicz, U., Hasselmann, K., 1993: Mean Circulation of the Hamburg LSG OGCM and Its Sensitivity to the Thermohaline Surface Forcing, J. Phys. Oceanogr., 23, 731-757.

Manabe, S., and R.J. Stouffer, 1994: Multiple-century response of a coupled ocean-atmosphere model to an increase of atmospheric carbon dioxide, J.Climate, 7, 5-23.

Marotzke J. and J. Willebrand, 1991: Multiple equilibria of the global thermohaline circulation. Journal of Physical Oceanography, 21, 1372-1385.

MARS, 1995: Meteorological Archival and Retrieval System User Guide, Computer Bulletin B6.7/2 for Data Retrieval, ECMWF Meteorological Bulletin M1.9/2.

Marsh, R., Roberts, M.J., Wood, R.A., New, A.L., 1996: An Intercomparison of a Bryan-Cox-Type Ocean Model and an Isopycnic Ocean Model. Part II: The Subtropical Gyreand Meridional Heat Transport, J.Phys.Oceanogr., 26, 1528-1551.

Marsland, S. J. and J.-O. Wolff, 2000: On the sensitivity of Southern Ocean sea ice to the surface fresh-water flux: A model study. Submitted to J.Geophys.Res.

Martinson, D. G., 1990: Evolution of the Southern Ocean winter mixed layer and sea ice: Open ocean deep water formation and ventilation. J.Geophys.Res., 95(C7), 11641-11654.

Mertz, G., and D.G. Wright, 1992: Interpretations of the JEBAR term, J.Phys.Oceanogr.,22, 301-305.

Möller, F., 1973: Einführung in die Meteorologie, Band 1. Bibliographisches Institut Mannheim, B.I.-Wissenschaftsverlag, 1973.

Molinari, R.L., W.D.Wilson and K.Leaman, 1985: Volume and heat transports of the Florida current: April 1982 through August 1983. Science, 227(4684): 295-297, 1985.

Müller, P., J.Willebrand, 1985: Equations for oceanic motions, in J.Sündermann (ed.), Landolt-Börnstein, Oceanography, Springer, Berlin.

Murray, S.P. and D.Arief, 1988: Throughflow into the Indian Ocean through the Lombok Strait, January 1985-January 1986. Nature, 333(6172), 444-447, 1988.

Muneyama, K., S.Nakamoto, T.Kawano, Y.Kashino, H.Watanabe, J.Pariwono, J.Banharnahor and H.Manoto, 1994: An observation study of the volume transport of the Indonesian throughflow. Eos, 75(25 Supplement), 1994.

Nakamura , M., PH. Stone, and J. Marotzke, 1994: Destabilization of the thermohaline circulation by atmospheric eddy transports. J.Climate, 7, 1870-1882.

Oberhuber, J.M., 1988: An Atlas Based on the 'COADS' Data Set: The Budgets of Heat, Buoyancy and Turbulent Kinetic Energy at the Surface of the Global Ocean. Report No.15,Max-Planck-Institut für Meteorologie, Hamburg.

Oberhuber, J.M., 1993a: Simulation of the Atlantic Circulation with a Coupled Sea Ice -Mixed Layer - Isopycnal General Circulation Model. Part I: Model Description.J.Phys.Oceanogr.,23, 808-829.

Oberhuber, J.M., 1993b: Simulation of the Atlantic Circulation with a Coupled Sea Ice -Mixed Layer - Isopycnal General Circulation Model. Part II: Model Experiment.J.Phys.Oceanogr.,23, 830-845.

Oberhuber, J.M., 1993c: The OPYC Ocean General Circulation Model. Techn. Rep. No.7,German Climate Computer Center, Hamburg.

Östlund, G.H. and Hut,G. 1984: Arctic Ocean Water Mass Balance From Isotope Data. J.Geophys. Res., Vol. 89 (C4), 6373-6381.

Niiler, P.P., W.J.Schmitz and D.Lee, 1985: Geostrophic volume transport in high eddy-energy areas of the Kuroshio Extension and Gulf Stream. JPO, 15(7), 825-843, 1985.

Pacanowski, R.C., 1995: MOM 2 documentation, user's guide and reference manual, Technical Report No.3, GFDL Ocean Group, Princeton University, Princeton.

Pacanowski, R. C. and S. G. H. Philander, 1981: Parameterization of vertical mixing in numerical models of tropical oceans. J.Phys.Oceanogr., 11, 1443-1451.

Pacanowski, R.C., K.Dixon, and A. Rosati, 1991: The G.F.D.L. Modular Ocean Model users guide version 1.0, Technical report 2, GFDL Ocean Group, Princeton.

Pacanowski, R.C., and A. Gnanadesikan, 1998: Transient response in a z-level ocean model that resolves topography with partial cells, Monthly Weather Review, 126, 3248-3207.

Pacanowski, R.C., andS.M. Griffies, 1999: MOM 3.0 manual, GFDL, Princeton University, Princeton.

Parkinson, C. L. and W. M. Washington, 1979: A large-scale numerical model of sea ice. J.Geophys.Res., 84(C1), 311-337.

Philander, G.P., R.C. Pacanowski, N.C. Lau, and M.J. Nath, 1992: Simulation of ENSO with a global atmosphere GCM coupled to a high-resolution tropical Pacific Ocean GCM, J.Climate, 5, 308-329.

Rahmstorf, S. and J. Willebrand, 1994: The role of temperature feedback in stabilizing the thermohaline circulation. J.Phys.Oceanogr. 25, 787-805.

Rintoul, S.R., 1991: South Atlantic Interbasin Exchange. J. Geophys. Res., 96(C2), 2675-2692, 1991.

Rintoul,S.R. and C.Wunsch, 1991: Mass, heat, oxygen and nutrient fluxes and budgets in the North Atlantic Ocean. DSR, 38, Suppl.1, S355-S377, 1991.

Rintoul, S., Hughes, C., Olbers, D., 2000: The Antarctic Cirumpolar Current System, In: Ocean Circulation and Climate, Eds: G. Siedler, J. Church and J. Gould. Academic Press, New York.

Roberts, M.J., Marsh, R., New, A.L., Wood, R.A., 1996: An Intercomparison of a Bryan-Cox-Type Ocean Model and an Isopycnic Ocean Model. Part I: The Subpolar Gyre and High-Latitude Processes, J.Phys.Oceanogr., 26, 1495-1527.

Roeckner, E., K. Arpe, L. Bengtsson, M. Christoph, M. Claussen, L. Dümenil, M. Esch, M. Giorgetta, U. Schlese, and U. Schulzweida, 1996: The atmospheric general circulation model ECHAM-4: Model description and simulation of present-day climate. Reports of the Max-Planck-Institute, Hamburg, No. 218, 90 pp.

Sarmiento, J.L.: On the north and tropical Atlantic heat balance, J.Geophys.Res., 91, 11677-11689, 1986.

Saunders, P.M., and S.R. Thompson, 1993: Transport, heat, and freshwater fluxes within a diagnostic numerical model (FRAM), J.Phys.Oceanogr., 23, 452-464.

Saunders, P.M. and B.A.King, 1995: Oceanic fluxes on the WOCE A11 section. JPO, 25(9), 1942-1958, 1995.

Schönwiese, C.-D., 1992: Praktische Statistik für Meteorologen und Geowissenschaftler. Gebrüder Bornträger, Berlin.

Schott, F.A., T.N.Lee and R.Zantopp, 1988: Variability of structure and transport of the Florida current in the period range of days to seasonal. JPO, 18(9), 1209-1230, 1988.

Semtner, A.J., and R.M. Chervin, 1988: A simulation of the global ocean circulation with resolved eddies, J.Geophys.Res., 93, 15502-15522.

Semtner A.J., and R.M. Chervin, 1992: Ocean general circulation from a global eddy- resolving model. J.Geophys.Res. 97 (C4), 5493-5550
Smethie W.M., R.A.Fine, A.Putyka, and E.P.Jones, 2000: Tracing the flow of North Atlantic Deep Water using chlorofluorocarbons, J.Geophys.Res., 105, 14297-14323.

SOC, 1997: Surface Flux Climatology (Version 1.1) of the Southampton Oceanography Centre.Int. WOCE Newsletter, No.29, p.10, Dec.1997.

Stössel, A. and S. J. Kim, 1998: An interannual Antarctic sea-ice - ocean mode. Geophys.Res.Lett., 25(7), 1007-1010.

Stössel, A., S. J. Kim, and S. S. Drijfhout, 1998: The Impact of Southern Ocean Sea Ice in a Global Ocean Model. J.Phys.Oceanogr., 28(10), 1999-2018.

Taft,B.A.,1978: Structure of Kuroshio, south of Japan. Journal of Marine Research, 36(1), 77-117, 1978.

Teague, W.J., A.M.Shiller and Z.R.Hallock, 1994: Hydrographic section across the Kuroshio near 35 degrees N, 143 degrees E. JGR, 99(C4), 7639-7650, 1994.

UNESCO, 1983: Algorithms for computation of fundamental properties of seawater by N.P.Fofonoff and R.C.Millard Jr. Unesco technical papers in marine science 44. Unesco, 1983.
Venzke, S., M. Latif and A. Villwock, 2000: The Coupled GCM ECHO-2. Part II: Indian Ocean Response to ENSO. J.Climate, 13, 1371-1383.

Vinje, T. and O.Finnekasa, 1986: Ice transport through the Fram Strait. Norsk Polarinstitutt, Skrifter No.186, 39 p., 1986.

Vinje, T., N.Nordlund, A. Kvambekk, Monitoring ice thickness in Fram Strait, J.Geophys.Res., 103, 10437-10449, 1998.

Warner, M.J., and R.F. Weiss, 1992: Chlorofluoromethanes in South Atlantic Antarctic Intermediate Water, Deep Sea Res., 39, 2053-2075.

Whitworth, T.III, 1983: Monitoring the Transport of the Antarctic Circumpolar Current at Drake Passage. JPO, 13, 2045-2057.

Whitworth, T., W.D. Nowlin, and S.J. Worley, 1982: The net transport of the Antarctic Circumpolar Current at Drake Passage, J.Phys.Oceanogr., 12, 960-971.

Whitworth, T.III and R.G.Peterson, 1984: Volume Transport of the Antarctic Circumpolar Current from Bottom Pressure Measurements. JPO, 15, 810-816, 1984.

Willebrand, J., B. Barnier, C. Bning, C. Dieterich, P.D. Killworth, C. LeProvost, Y. Jia, J.-M. Molines and A.L. New, 2000: Circulation characteristics in three eddy-permitting models of the North Atlantic. revised version, Progress in Oceanography (accepted).

Wijffels, S.E., J.M.Toole, H.L.Bryden, R.A.Fine, W.J.Jenkins, and J.L.Bullister, 1996: The water masses and circulation at 10°N in the Pacific. DSR, 43, No.4, 501-544, 1996.

Wolff, J.-O., E. Maier-Reimer, and S. Legutke, 1997: The Hamburg Ocean Primitive Equation Model. Technical report, No.13, German Climate Computer Center (DKRZ), Hamburg, 98 pp.

Zalesak, S.T., 1978: Fully multidimensional flux-corrected transport algorithms for fluids, J.Comput.Phys., 31, 335-362.